UNIVERSITÉ DU LUXEMBOURG

PhD-FSTC-2019-30
The Faculty of Sciences, Technology and Communication

DISSERTATION

Defence held on 03/05/2019 in Luxembourg
to obtain the degree of

DOCTEUR DE L'UNIVERSITÉ DU LUXEMBOURG

EN *Chimie*

by

Camila Honorato Rios
Born on 08 March 1985 in Temuco, (Chile)

SELF-ORGANIZING CELLULOSE NANORODS: FROM THE FUNDAMENTAL PHYSICAL CHEMISTRY OF SELF-ASSEMBLY TO THE PREPARATION OF FUNCTIONAL FILMS

Dissertation defence committee

Dr Jan Lagerwall, dissertation supervisor
Professor, Université du Luxembourg

Dr Virginia Davis
Professor, Auburn University

Dr Phillip Dale, Chairman
Professor, Université du Luxembourg

Dr Frank Giesselmann
Professor, University of Stuttgart

Dr Lennart Bergström, Vice Chairman
Professor, Stockholm University

Université du Luxembourg
The Faculty of Sciences, Technology and Communication

Self-Organizing Cellulose Nanorods: From the fundamental physical chemistry of self-assembly to the preparation of functional films

Camila Paz Honorato Rios

Dissertation to Obtain the Degree
Doctor of Philosophy
in the subject of Chemistry
at the Physics and Materials Science Research Unit

To Daniel and Emma for endless love

Acknowledgements

First of all, I would like to thank my supervisor **Prof. Jan Lagerwall** for the opportunity to be part of the MISONANCE project and of the ESMP group. I would also like to use these lines to acknowledge my co-workers who are usually not mentioned but have been important in the last four years, perhaps not directly related to the projectd but mostly to my personal life. I have to begin with **Zornitza Tosheva**. Initially Zory showed me the basic techniques that were needed for working with CNCs, but most important, she was the one who came up with the idea of using commercial CNCs from University of Maine. This was crucial for this thesis, it saved me a considerable amount of lab work and the material is just excellent. I also have to mention **Nina Schwarz**, she was my outstanding "minion" who worked with me during my pregnancy. She was great in the lab and a huge help that time, thanks a lot for always being in time, specially in my very early mornings. All my gratitude to **Yong Geng** for answering all my repetitive questions about liquid crystals, microscopy, and even how to make decent pictures with the camera. Of course my dear friend **JungHyun Noh**, you were always very helpful and a good friend, but even more important, a big support and model to follow during this Ph.D. My family and I had a great time every time your visited us. A big thanks to **Rao Jampani**, he spent a considerable amount of time helping with my results and with many small things in the lab. Thanks for reading part of this thesis and for all the talking about life in general. I truly wish you all the best. Many thanks to **Irena Drevenŝek-Olenik** for giving me the chance to stay in her lab in Ljubljana, and thanks also to **Matjaž Liĉen** for his assistance during the SEM imaging of some of our samples during my time there. Many thanks are also extended to **Lena Godinho** for all her kind feedback that I received after she read one draft of this work. I would like to thank every group member: **Urŝa, Lionel, Anjali, Shameek, Rijeesh, Nikolay, Larry, Hakam, Catherine, Manos, Vanessa, Astrid, Johanna, Christina, JiHyun, Anshul, Meenu, Hakam, Ashik, Shariff** and **Giusy**. Thanks also to **Monique Wiesinger** for her support and assistance with some chemicals and equipment. **Monique** is one of the most efficient person that I met here in Luxembourg and made my work much easier.

Finally, I would like to thank my family, Dan and Emmita, thanks for all the support, especially during those days when I was physically at home but with my mind at work...I am looking forward to our next steps together.

Abstract

Cellulose nanocrystals (CNCs), nanorods isolated by acid hydrolysis from cellulose sources, belong to a selective type of functional biomaterials. The intriguing ability of these nanoparticles to self-organize and develop a chiral nematic liquid crystal phase when suspended in aqueous suspensions, is increasing interest regardless of the diverse range of research fields. Unfortunately (or fortunately, for this thesis), pristine CNCs are always disperse, with great variations in rod length within a single sample. Of particular interest is the fractionation of CNC rods by separation of the coexisting phases: isotropic phase from the liquid crystalline (LC) part. Since the aspect ratio is considered to be the critical parameter that dictates the particle fraction at which cholesteric-isotropic phase separation starts, it is expected that the high aspect ratio rods will separate from low aspect ratio rods, and this is indeed what I find in this thesis.

By a systematic repetition of separation of phases, I could reach a quality of separation of long from short rods that is remarkable. The fractionation procedure was then improved by varying the equilibrium phase volume fraction Φ at which the phases were separated, reducing with this new procedure the multiple separations from five cycles to only one. The onset of liquid crystallinity was drastically reduced in the long rod fraction and the decrease in the threshold for complete liquid crystallinity was even stronger.

The mass fraction threshold at which gelation of the CNC suspension is triggered is not at all affected by the fractionation. Since gelation is a percolation phenomenon, the expectation was that also the onset of gelation would move to lower mass fractions, but this remained at about the same value. Together with the shift to lower mass fractions of the cholesteric liquid crystal phase formation we have thus opened access to a whole new range of the equilibrium phase diagram, where the full sample is cholesteric yet not gelled.

I demonstrate that the critical parameter for inducing gelation is in fact not the fraction of CNC, but the concentration of counterions in the solution. This suggests that the gelation is more complex than direct percolation between individual CNC rods, and instead is related to loss of colloidal stability due to reduced electrostatic screening.

I also show that the behavior of key parameters, such as the period of the helical modulation, so-called pitch, that is characteristic of the cholesteric phase, is very different in the range of phase coexistence compared to the range of complete liquid crystallinity. In addition, I find

that the dependence of the pitch on CNC mass fraction has less to do with the size of the nanorods but rather than with the variation of effective volume fraction as a result of more rods in the suspension or higher counterion concentration. I corroborate this hypothesis by adding different amounts of salt to CNC suspensions of varying mass fraction such that the ion concentration is held constant, thereby tuning the pitch to the same value throughout the suspensions.

In films prepared by drying CNC suspensions, the pitch can go down to a few hundred nanometers, resulting in circularly polarized colorful Bragg reflection of visible light. By working with the long-rod fraction we can absolutely obtain a highly-ordered monodomain structure that results in uniform color of film, with only one circular polarization reflected, as should be the case for CNC solid films.

While the study is carried out on CNCs, the implications go far beyond this particular nanomaterial, revealing new challenges and opportunities in general liquid crystal and colloid physics, as well as in strategic research where fractionation and the drying of initially disperse populations of nanorods is desirable.

Keywords: Cellulose nanocrystals, colloids, liquid crystals, fractionation, cholesteric helix, thin films, photonic crystal, Bragg reflection.

Publications linked to this thesis

1. *Equilibrium Liquid Crystal Phase Diagrams and Detection of Kinetic Arrest in Cellulose Nanocrystal Suspensions*

   Camila Honorato–Rios, Anja Kuhnhold, Johanna Bruckner, Rick Dannert, Tanja Schilling, Jan Lagerwall

   Frontiers in Materials (2016)

2. *Enhancing Self-Assembly in Cellulose Nanocrystal Suspensions Using High-Permittivity Solvents*

   Johanna Bruckner, Anja Kuhnhold, **Camila Honorato–Rios**, Rick Dannert, Tanja Schilling, Jan Lagerwall

   Langmuir (2016)

3. *Fractionation of cellulose nanocrystals: enhancing liquid crystal ordering without promoting gelation*

   Camila Honorato–Rios, Claudius Lehr, Christina Schütz, Roland Sanctuary, Mikhail Osipov, Jörg Baller, Jan Lagerwall

   NPG Asia Materials (2018)

4. *Enabling macroscopic-scale uniform helical nanorod arrangements by fractionating cholesteric liquid crystalline suspensions of cellulose nanocrystals*

   Camila Honorato–Rios & Jan P.F. Lagerwall

   Manuscript in preparation

Book chapter

1. *Cholesteric liquid crystal formation in suspensions of cellulose nanocrystals. Liquid crystals with nano and micro particles*

   Camila Honorato-Rios, Johanna Bruckner, Christina Schütz, Sammy Wagner, Zornitza Tosheva, Lennart Bergström, Jan P.F. Lagerwall

   World Scientific Publishing Co. Pte. Ltd. (2017)

Additional publications

1. *Transparent nanocellulose-pigment composite films*

   Honorato–Rios, C., Kumar, V., Liu, J., Koivula, H.,Xu, C., Toivakka, M.

   Journal of Materials Science (2015)

2. *Tailor-made hemicellulose-based hydrogels reinforced with nanofibrillated cellulose*

   Dax, D., Chavez, M., **Honorato–Rios, C.**, Liu, J., Steven, S., Mendonca, R.T., Xu, C., Willfor, S., Sanchez,. J

   Nordic Pulp Paper Research Journal (2015)

Contents

List of Tables

List of Figures

Chapter 1

Goal and overview of this study

Over the last years, bio-based nanomaterials have gained even more importance in different industrial sectors as well as in fundamental research, especially due to environmental reasons. Among others, the nanotechnology research has experience a shift towards sustainable raw materials. Cellulose belongs to this category, which corresponds to the most abundant bio-polymer on earth. Cellulose can be extracted from a large variety of plants, while cellulose from wood has been used for centuries to produce paper and cotton for the manufacturing of tissues (e.g. for clothes). Continuous improvement of the purification processes of cellulose lay the foundation for the research with one highly ordered part of cellulose, cellulose nanocrystals (CNCs). CNCs can be obtained by different chemical approaches and the final cellulose nanorods consist of almost pure crystalline cellulose with a diameter of 5-10 nm and length ranging from 100 nm to a few microns. The dimension of the crystals are strongly dependent on the raw material chosen as a source of cellulose, increasing the degree of complexity when studying its properties. Cellulose nanocrystals have attracted the interest of researchers with different backgrounds due to their low density and thermal expansion, outstanding mechanical properties as well as their optical properties. For this study, the ability of CNCs to self-assemble in aqueous suspension and to form cholesteric (nematic) liquid crystals was exploited. Extensive studies have been carried out in the past, focusing on the chemistry used for the preparation of CNCs and/or chemical modification of the surface of the crystals. In contrast to these studies, the goal of this thesis is to better understand the physics of CNCs in suspensions. Previously carried out research led to conflicting conclusions and unsatisfactory reproducibility of the experiments, mainly due to the previously mentioned high variability of the dimensions of the CNC rods. This thesis had from the beginning a strongly physics-based oriented and systematic approach to study the macroscopic behaviour of the CNC suspensions.

This thesis is organized in seven chapters. Chapter 2 introduces the basic concepts of liquid crystals and the key physical chemistry concepts, in addition to the experimental techniques utilized throughout the study. The fundamental concepts are described for cholesteric liquid crystals and for the preparation of the nanorods are discussed in full. Chapters 3 – 6 present the most relevant results of my research. In Chapter 3, I start with the characterization of the commercial material mainly used in this thesis. It was of high importance to verify that the commercial CNC is very pure and hence a suitable base material for the planned sensitive experiments. To assure this, I performed series of purification steps and finally compared the as-received CNC from the manufacturer (FPL) to the purified CNC suspensions at different mass fractions. In Chapter 4, I present three procedures for CNC fractionation by exploiting the spontaneous rod fractionation that takes place between coexisting isotropic and chiral nematic phases. Afterwards, I study the effect of the aspect ratio on the phase diagram by preparing suspensions using the different fractions and allowing them to phase separate. In Chapter 5, I discuss gelation and the parameters that govern this non-equilibrium phenomenon. In Chapter 6, I explore how the helix develops at different mass fractions of various CNC samples and discuss what is the real effect of the rod size and ion concentration on the final pitch. The experimental part of this thesis is finalized in Chapter 7 by preparing dry iridescent CNC films and by explaining the appearance of homogeneous or inhomogeneous colors in these films. The overall conclusions are presented in Chapter 8.

Chapter 2

Background

Overview of the chapter

The key concepts that are discussed in this thesis are presented in this chapter. The concepts are especially related to cholesteric (chiral nematic) liquid crystals and to the physical chemistry of colloids for cellulose nanocrystals (CNCs) in aqueous suspensions. By discussing the Onsager and DLVO (Derjaguin, Landau, Verwey and Overbeek) theories applied to a system of charged rod-like particles, I investigate the competition of gelation and liquid crystal ordering. The chapter is finalized by presenting the experimental techniques for preparing CNCs and the most relevant characterization methods.

2.1 Liquid crystals

Liquid crystals can be defined as moderately organized anisotropic systems, which can exhibit properties of solid crystal states and of the isotropic liquids [7]. A solid crystal has long-range, three-dimensional, positional and orientational order, while a liquid has neither positional order nor orientational order over long range. The study of liquid crystals started back in the year 1888, when an Austrian botanist named Friedrich Reinitzer reported his observations on cholesteryl benzoate, noting a strange behavior that he interpreted as two melting points. He noticed that the solid material did not melt to a colorless liquid after increasing temperature, but always to a muddy fluid until, by further temperature increase, the compound changed again into a clear and transparent liquid. Reinitzer receives most of the credits on the discovery of one more state of matter: the liquid crystal state. Nevertheless, it was Otto Lehmann the person who proposed the liquid crystal phase after investigating Reinitzer's material. It has to be considered the possibility that liquid crystalline phases might have been observed before, but a deeper investigation of this new type of material was lacking that time.

Liquid crystals are largely classified into two categories, the thermotropic and the lyotropic liquid crystals or mesophases. The word mesophase has a Greek origin, with meso meaning in between (the intermediate phase between a solid and a liquid). Typically, the mesophase is developed by anisotropic shapes, thus the building blocks of the liquid crystal phase are called mesogens. In thermotropic liquids crystal, the phase is controlled generally by a change of temperature, while in lyotropic liquid crystals, the phase appears depending on the presence of a suitable solvent and on having the mesogenic material dissolved or dispersed in the right mass fraction range. Because of the latter, lyotropic mesophases are always mixtures, while many of the reported thermotropic liquid crystals are single compounds.

In this thesis, my focus is on rodlike particles called cellulose nanocrystals. Suspensions of these in water belong to the category of lyotropic liquid crystals.

2.1.1 Chirality

Chirality can be defined as the lack of mirror symmetry, being an inherent property of many systems in nature, such as biomolecules (e.g. natural polypeptides, enzymes or DNA), as well as snails and plants that have developed a helical shape with unique handedness [7]. Louis Pasteur conducted experiments that showed the importance of stereochemistry in the understanding of chirality. He observed that salt of tartaric acid forms two types of chiral crystals, being mirror images of each other [8]. However, chirality is not unique to molecules, as it can also be applied to geometrical objects.

An object is referred to be achiral if it is identical to its mirror image. If we consider now molecules with the same constituent components but presenting variations in how their atoms are located in space, we are able to call them stereoisomers. Two stereoisomers that behave like image and mirror image are enantiomers (Figure 2.1). Enantiomers present the peculiarity of having exact physical behaviour, for example they exhibit exactly the same melting points as well as the exact properties related to their chirality, with the only exception of showing an opposite sign [7].

In liquid crystals, chirality can directly be introduced within the mesogen by the incorporation of chiral elements. This can be accomplished by replacing carbon atoms by different ligands (atoms or groups of atoms joined to the central atom). Another method is the addition of a small amount of chiral dopant—which can be mesogenic or non-mesogenic—to an achiral host liquid crystal. The chirality related effects typically increase linearly with the concentration of chiral dopants in the host phase, at least in the limit of low chiral dopant concentrations.

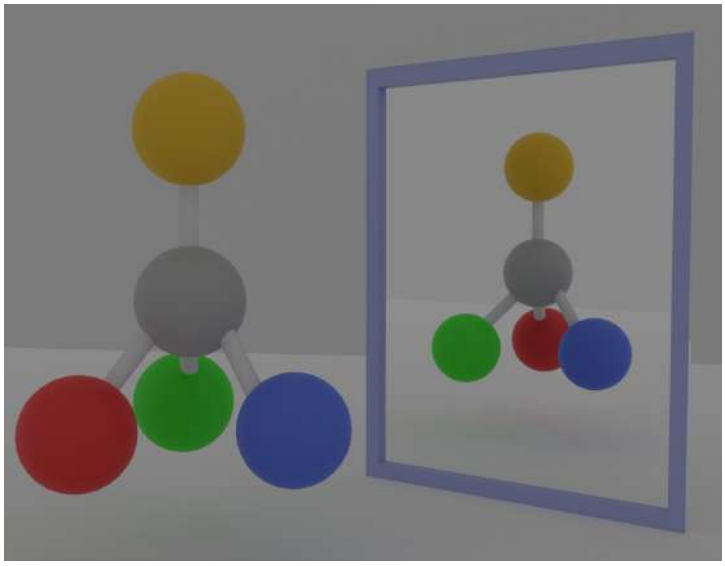

Figure 2.1: Schematic illustration of two enantiomers of a generic molecule that is chiral.

2.1.2 The nematic phase

The nematic is the most common and simplest liquid crystal phase, in which the building blocks are aligned along a common direction that is known as the director. The director is typically abbreviated with **n**, as indicated in Figure 2.2. In general, the building blocks in the isotropic phase are randomly oriented, with neither orientational nor positional order. Once the phase transition takes place and the nematic phase forms, the building blocks will orient with long-range orientational order (although not perfect) but still, no positional order. The lack of positional order in a nematic phase can be understood in terms of their centers of mass. If we imagine an arrangement of all the centers of mass of each building block and plot them, we would not see any difference compared to the isotropic phase; the main variation is the orientational ordering of the building blocks, even though the nematic phase is the most disordered among the different variety of liquid crystalline phases [9].

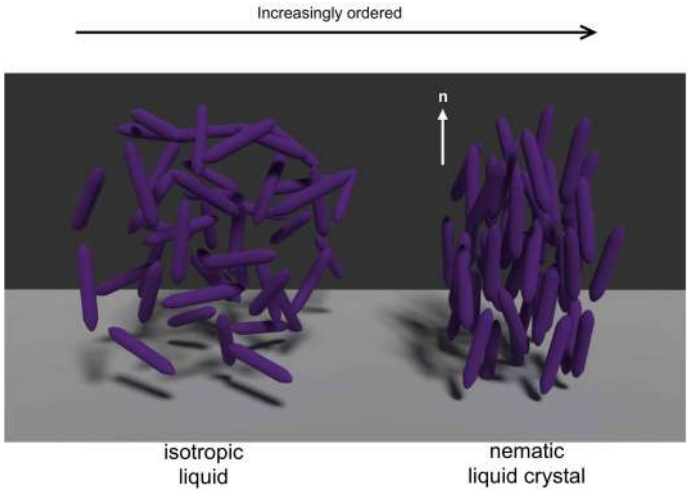

Figure 2.2: Schematic illustration of an isotropic liquid and the nematic liquid crystal phase. The director **n** indicates the average direction of the building blocks.

Despite the fact that the building blocks in a nematic phase have the tendency to orient along the director **n**, the thermal fluctuations lead to angular deviations [10]. Considering these deviations, the analysis of the degree of orientational order can be quantified by the scalar order parameter S, according to:

$$S = \frac{1}{2}\langle 3cos^2\theta - 1\rangle, \tag{2.1}$$

where θ is the angle between the axis of the building block and the director and the brackets $\langle\ \rangle$ indicate the statistical spatial or temporal average [11]. The order parameter can be found within the range of $-\frac{1}{2} \leq S \leq 1$. For the case of perfectly aligned building blocks, the order parameter would be $S = 1$. On the contrary $S = 0$ refers to the random orientation of the

building blocks in the isotropic phase. The negative order parameter $S = -\frac{1}{2}$ indicates that the building blocks are located in the plane without any preferred orientation and perpendicular to the director. Generally, the order parameter is positive, and for the case of the thermotropic liquid crystals, for which their phase transitions depend on the temperature, S can be found in the range of 0.4 – 0.8 [10, 11].

The deformations in the director field in a nematic liquid crystal can be described as the contribution of three fundamental elastic distortions, known as splay, twist and bend. The schematic illustration of the three types of deformation is presented in Figure 2.3.

The total elastic energy per unit volume of a nematic liquid crystal, $G_{deform.}$, can be expressed as:

$$G_{deform.} = \frac{1}{2}[K_1(\nabla \cdot \mathbf{n})^2 + K_2(\mathbf{n} \cdot (\nabla \times \mathbf{n}))^2 + K_3(\mathbf{n} \times (\nabla \times \mathbf{n}))^2] \tag{2.2}$$

where K_1, K_2 and K_3 correspond to the Frank elastic constants from to the three fundamental types of distortion mentioned before.

Generally speaking, the three different elastic constants present no significant differences in value. For this reason we can use one approximation considering that K_1=K_2=K_3 are in the order of $\sim 10^{-12}$ N, although K_3 (the bending constant) can present larger values compared to the other two elastic constants [9].

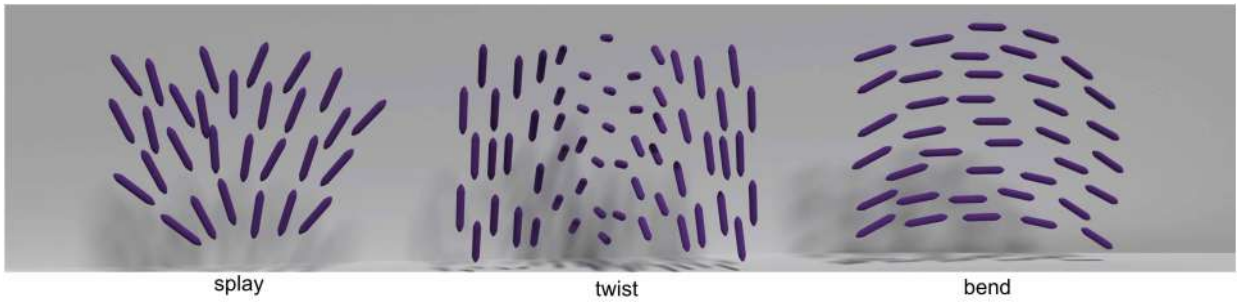

Figure 2.3: The three types of elastic deformations that can be found in a nematic liquid crystal.

Nevertheless, Eq. 2.2 is not suitable for chiral nematic liquid crystals, since this expression only applies for systems with a completely uniform ground state director field [12], which is not the situation for the helical structure which is the hallmark of the chiral nematic, also called cholesteric, phase.

Because of this, it is necessary to modify the expression for the total elastic energy in order to be compatible for chiral nematics. The corrected expression must now include:

$$G_{twist}^{N*} = \frac{1}{2}K_2(\mathbf{n} \cdot (\nabla \times \mathbf{n}) + q_0)^2 \tag{2.3}$$

From Eq. 2.3, $q_0 = 2\pi/p_0$ denotes the wave vector of the cholesteric helix and p_0 corresponds to its natural pitch. Following the description used by Lagerwall et. al [12], if now the cholesteric director field is parametrized as $\mathbf{n} = (\cos\ qz,\ \sin qz,\ 0)$, with q as an arbitrary helical wave vector and $\hat{z}$ the direction of the helix axis, the curl of the director, $\nabla \times \mathbf{n}$, develops into $-q\mathbf{n}$.

If we now consider that $\mathbf{n} \cdot \mathbf{n} = 1$, Eq. 2.3 can now be presented as:

$$G_{twist}^{N*} = \frac{1}{2}K_2(q - q_0)^2. \tag{2.4}$$

This means that the free energy density is now minimized due to the existence of a twisted director field, instead of by a uniform director field as in the case of the unmodified Eq. 2.2. If now the natural twist is in the order of the wavelength of visible light (or even smaller), the modified expressions in 2.3 or 2.4 would be considerably affected, meaning that the added elastic energy of the system is not trivial. On the contrary, if the natural twist is weak, this will not make a significant contribution to the free energy density of the system [12].

2.1.3 Birefringence in liquid crystals

A common property that is experienced by almost all types of liquid crystals is their optical anisotropy, in which the refractive index of the material depends on the direction and polarization of the incident light [11]. It means that the interaction of light with the material would depend on the orientation of the building blocks as well as on how the light propagates within the sample [10].

For anisotropic materials, the incident light beam that enters at an angle $\beta \neq 0$, angle formed between the light beam and the optic axis, can split into two components, the *ordinary ray* and the *extraordinary ray*. The resulting two beams experience different directions and velocities due to their different refractive indices: the ordinary refractive index (n_o) for the case of the ordinary ray, which is polarized perpendicular to the optic axis, and the extraordinary refractive index (n_e), for the extraordinary ray, which is polarized parallel to the optic axis, [10] respectively. The variation in velocity of the two beams leads also to a phase difference according to:

$$\Delta\phi = \frac{2\pi}{\lambda}(n_e - n_o)d \tag{2.5}$$

where λ is the vacuum wavelength of the incident light and d is the distance traveled in the medium [11].

The indices n_o and n_e are correlated according to the principal refractive indices $n_\perp$ and $n_\parallel$ as:

$$n_e = \frac{n_\parallel n_\perp}{\sqrt{n_\parallel^2 \cos^2 \beta + n_\perp^2 \sin^2 \beta}} \tag{2.6}$$

for which $n_o = n_\perp$ and β the angle between the light beam and the optic axis. Finally, birefringence is defined as the difference between n_e and n_o, according to the expression $\Delta n = n_e - n_o$.

2.1.4 Cholesteric phases

The cholesteric or chiral nematic phase, as its name suggests, corresponds to the chiral form of the nematic liquid crystal, normally expressed as N^*, where the chirality is denoted by the asterisk. The building blocks lack of positional order, although they are oriented along a common direction **n** (the director), as for the case of the nematic liquid crystals. In cholesteric phases, the director rotates in a helical manner, with the twist axis perpendicular to the director

It is rather common to indistinguishably use the terms cholesteric and chiral nematic for indicating the same helical phase, since the first compound found that developed a chiral nematic liquid crystal was a cholesterol derivative. Figure 2.4 presents a representative illustration of rod-like building blocks forming a helical structure due to the tendency of the particles to self-organize at a small angle with respect to adjacent particles. For the only reason of simplicity of drawing, the rods have been localized to layers, which do not exist in reality, and within each layer they are drawn with perfect orientational order, in contrast to the typical $S \approx 0.5$ case of a real chiral nematic.

This helical structure brings important features to this type of materials. For example, they exhibit a distinct pitch p much larger compared to the size of the building blocks. The pitch is defined as the distance for which the director makes a complete turn, although the periodicity occurs already at $p/2$.

The helix gives outstanding properties to chiral materials when p is on the order of the wavelength of visible light, in the range of 300-500 nm. Within these values, the sample will reflect colors that only come from the self-organization of the building blocks. This selective reflection can be explained according to Bragg's law (see Figure 2.5), when light is incident along the helix with a short-pitch. The reflected light should reflect only one circular polarization with the

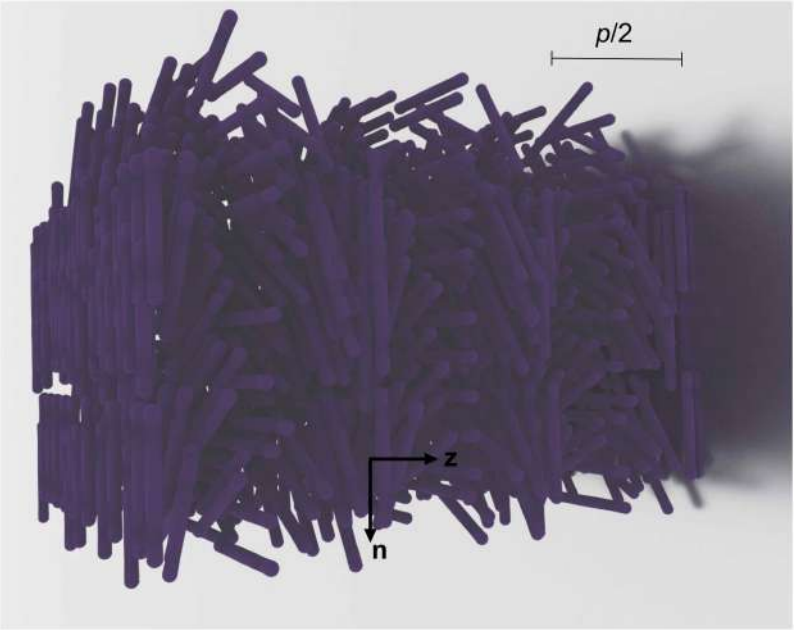

Figure 2.4: In cholesteric liquid crystals, the director **n** rotates in a helical fashion, with **n** always perpendicular to the helix axis z. The periodicity is equal to half the pitch, with p defined as the distance for which the director completes a whole turn. For simplicity of drawing, the rods have been localized to layers, which do not exist in reality, and within each layer they are drawn with perfect orientational order, in contrast to the typical $S \approx 0.5$ case of a real chiral nematic.

same handedness as the helical structure. The wavelength that is reflected can be determined according to:

$$\lambda_r = \bar{n} p \cos\theta \tag{2.7}$$

where $\bar{n}$ corresponds to $(n_e + n_0)/2$, the average of the extraordinary and ordinary refractive indices, and θ corresponds to the angle that is formed between the incident light and the helical axis.

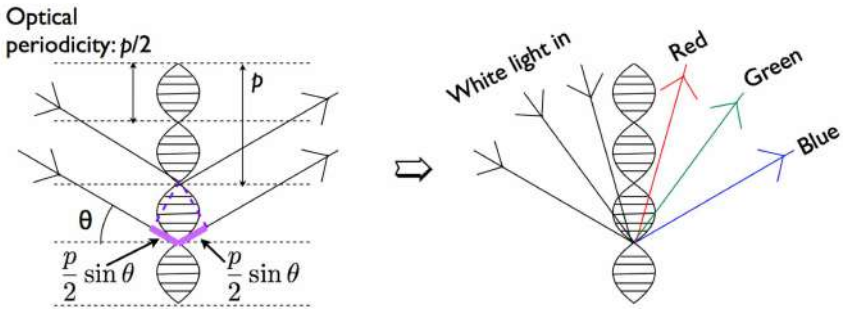

Figure 2.5: Representative illustration of the Bragg selective reflection for a chiral nematic liquid crystal with short pitch. The horizontal dashes in the central structure represent the projection of the director in the figure plane. From Lagerwall *et al.* [4]

Structural coloration is largely common in nature. The typical case is exhibited by some beetles,

feathers in peacock tails and some butterflies [13–15]. Nevertheless, the most beautiful blue color that is observed in a living organism due to Bragg selective reflection can be found in the Pollia condensata fruits [16].

2.2 The isotropic-nematic transition of hard-rod particles

Anisotropy emerges due to the rod-like shape and rather rigid character of the particles. In addition, an anisotropic steric interaction can be expected, due to the impenetrability of one particle by another. By only applying the steric interactions, Onsager founded his theory for the tendency of hard rods to experience a transition from the isotropic to an anisotropic phase when the density of the particles increases [17]. Two types of entropy need to be considered in order to understand the Onsager theory. Besides the orientational entropy, the entropy based on the translational degree of freedom needs to be taken into account. The excluded volume couples these two kinds of entropy. The excluded volume represents the volume into which the center of a building block cannot move because of the presence of other building blocks. When two hard rods lie at an angle with each other the excluded volume is always larger compared to the case in which the rods are parallel to each other. A parallel organization of the building block leads to a much lower excluded volume, a favorable condition for the translation entropy, which results in a higher mobility of the building blocks. The parallel alignment is however a state of low orientation entropy, thus there is a competition between the translational and orientational entropy, both with the tendency to reach their highest possible value. When the density is decreased relatively close to zero, the orientational entropy will always win because the building blocks are rarely colliding with each other. In this case, the increase in the translational entropy would only marginally impact the already large space in which the building blocks can move. While increasing the density, the importance of the excluded volume will be much larger. The more building blocks in the system will therefore lead to more parallel organization of the units. For that reason, the transition between the isotropic and the anisotropic states must happen at an intermediate density. Finally, the stability of the isotropic and the nematic phases depends on the geometrical morphology of the building blocks. The limits for the two-phase regime is given by the particle volume fraction ϕ, in which the isotropic phase loses its stability at $\phi_0 = 3.3d/L$. For the case of the formation of the nematic phase, the rod volume fraction is $\phi_1 = 4.5d/L$, with d the diameter and L the length of the rods [9].

2.3 Electrostatic forces and the DLVO theory

2.3.1 The Stern layer

If we think of a solid surface that is either positively or negatively charged, a few models have been proposed in order to understand the distribution of the different anions and cations in the system. The diffuse double-layer model considers the ionic atmosphere as being split in two regions, referred as the Stern layer and the diffuse layer. Close to the interface, between the particle surface and the surrounding media, the counterions dominate because of the attraction by the surface, but they are not present at high enough concentration to completely screen out the surface charge. This first region is known as the Stern layer, illustrated in Figure 2.6.

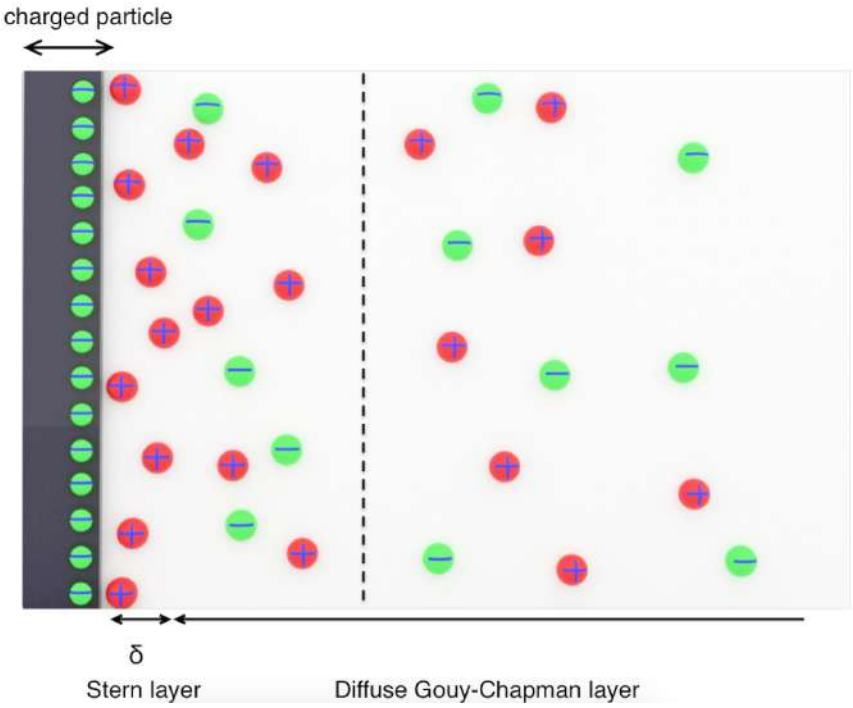

Figure 2.6: Representative illustration of the Stern layer for a negatively charged surface. The Debye length is denoted with a dashed line and the diffuse layer forms the major part of the right side of the illustration.

When getting further away from the surface, the diffuse layer will have a counterion concentration which gradually decreases with the distance from the surface [18]. This decrease has its origin in the thermal motion and will end up reaching an electroneutral solution. The overlap of the diffuse double layers of particles is the reason for their electrical forces. The length or thickness of the double layer is express as the Debye length and depends on the solvent medium, the temperature and the concentration of ions in the system according to:

$$\kappa = \sqrt{\frac{2e^2 z^2 n_\infty}{\epsilon \epsilon_0 k_B T}}, \tag{2.8}$$

where e is the elementary charge, ϵ_0 the vacuum permittivity, ϵ the relative dielectric constant of the medium, $k_B T$ the thermal energy calculated as the product of the Boltzmann constant and the temperature, z the valence of the ions and n_∞ the ion concentration far away from the surface [19].

2.3.2 The DLVO theory

Colloidal particles are able to interact due to the combination of different forces which are dependent upon the separation distance between the particles [20].

Quantitatively, the DLVO (Derjaguin, Landau, Verwey, Overbeek) theory is applied to describe the stability of colloidal suspensions. Figure 2.7 generally illustrates the profiles of these forces

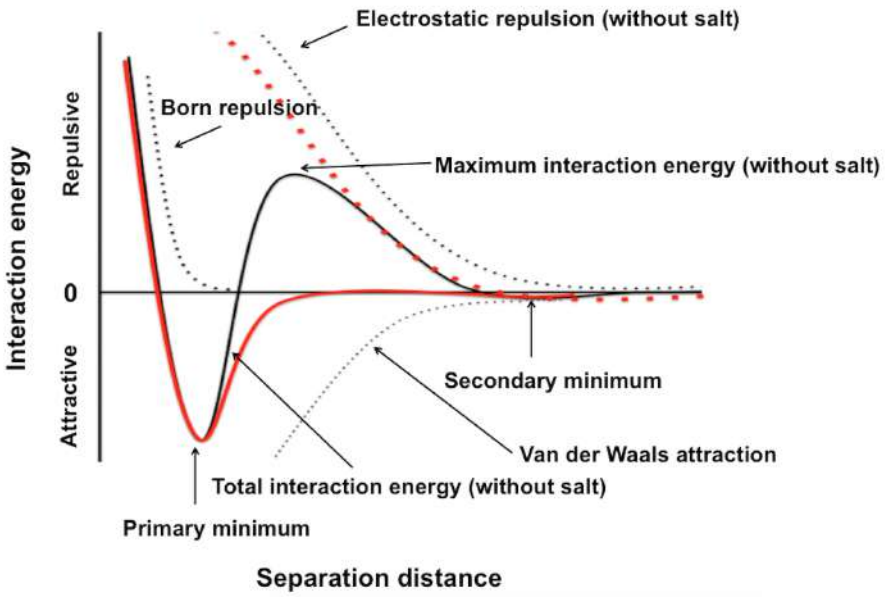

Figure 2.7: Interaction energy for a pair of spheres against their separation distance, known as the DLVO curve. The black curves refers to a system without the addition of external salt and the red curves refers to the system after the addition of salt. Figure redrawn with the permission from the original in [5].

against the separation distance between nanoparticles, known as the DLVO curve. The black curves indicate the interaction energy of a pristine system and the curves in red after the addition of a non-colloidal salt such as NaCl. The combination of the attractive van der Waals interaction together with the electrostatic or double-layer repulsion as well as shorter-range interactions—as for the case of the Born force—will lead to a total interaction energy, which

could result in attraction or repulsion between the surfaces [18,19]. The net interaction energy can be calculated as follows [19]:

$$\Phi_{net} = \Phi_A + \Phi_R, \tag{2.9}$$

with Φ_A the attractive and Φ_R the repulsive interaction energy, respectively. All curves are plotted in Figure 2.7.

The DLVO profile presents interesting information regarding the colloidal behavior of our system. At a rather close distance between the particles, we observe a primary minimum, corresponding to the global minimum free energy. If the particles get this close to one another, they will irreversibly aggregate as the minimum is much deeper than k_BT, hence thermal fluctuations cannot move the particles out of the minimum. However, there is also a secondary minimum in the salt-free curve, at about five times longer particle-particle separation. Between the primary and secondary minima there is a significant energy barrier, which is greater than k_BT in a stable colloid. If the system is prepared such that the particles do not reach the primary minimum, they will thus tend to reside preferentially in the secondary minimum. While they cannot move closer due to the energy barrier, thermal fluctuations will also move them further apart at many times; they are not trapped in the secondary minimum. [21].

The electrical double-layer that surrounds all particles in colloidal suspensions is thus fundamental for the overall behavior, as it provides electrostatic repulsion. In water or any other polar media, almost all particles are charged, resulting in positive or negative surfaces. Nevertheless, the most typical scenario corresponds to negative surfaces, which will be highly sensitive to pH, concentration of other added salts and to the nature of the functional chemical groups present at the particle surface. The reason why most surfaces are negatively charged has its origin in the nature of the counterions [3, 18]. Cations are generally smaller than anions and are typically more hydrated due to their more intense electric field. This causes the cations to remain in the aqueous solution, whereas the anions tend to absorb on the surfaces. The bonds between the ions and the water molecules are weak and the water molecules are constantly exchanged by water molecules from the bulk water. The number of water molecules which bind to ions depends on the nature of the ions and is referred to as hydration number. According to Israelachvili [3], the hydration number is considered more like a quantitative indicator of the degree to which ions bind water, than as an exact value. For the case of monovalent anions, they are only weakly hydrated and are hence less "dissolved" in the media. The hydration of counterions reduces the tendency of the ions to approach the surface and makes it less probable that the ion enters the Stern layer (Figure 2.6).

If we go back to Figure 2.7, the total interaction energy can be modified after the addition of a salt (curves in red). For this case, the attractive van der Waals contribution will not be affected by the extra ions in the system. However, the electrostatic repulsion largely drops (red dashed curve), leading to a decrease in the energy barrier. If the concentration of salt is high enough, the height of the energy barrier is decreased to $k_BT$or lower, allowing thermal fluctuations to drive the particles into the primary minimum. Because this is so deep, they will be stuck in this minimum and the particles will aggregate. If the amount of added salt is high enough, the system could thus be able to enter a kinetic arrested state, such being the case of some types of gelled materials.

2.4 Gelation

Jones [9] defined a gel as a network of macroscopic dimensions containing interconnected building blocks. The formation of a gel starts with an isolated building block which is bonding successively to other subunits, resulting in a system that goes form a liquid-like state—a sol—towards a system that can resist a shear force—a gel. A gel is more or less structurally disordered and usually contains large fractions of liquid. Despite of this poorly ordered structure, a gel reveals the mechanical properties of a solid. As per definition, gels encompass many different types of structures, whereby the building blocks might belong to different classes as well as being connected by different types of bonds. For example, bi- or multi-functional monomers can form covalent bonds between each other due to their capability to bond to more than one monomer, and as a consequence, three-dimensional networks are formed. If the individual building blocks consist of linear polymers connected by covalent cross-links, then the overall system is referred to as a rubber. However, linear polymers can also be linked to each other by physical bonds (e.g. hydrogen bonds) rather than chemical bonds, leading to a thermo-reversible network that is weak and might re-disperse in the liquid. Another possibility is that the building blocks themselves are colloidal aggregates that have been formed by molecules linked by physical interactions. In general, all these classes of gels have the common feature that they can go through a transition from the sol state to a gel state, induced by the continuous increase of bonds between the building blocks. This transition can be either called gelation transition or sol-gel transition.

The more bonds that are created between the building blocks in a steady manner, the more the macroscopic properties of the gel will change. This interesting characteristic of gel formation includes an abrupt transition from the liquid- to a solid-like material. Despite of the different microscopic details of gelation in the variety of systems, some generic features of the transition can be captured by the percolation model. In this case, clusters will start forming as more

bonds are created in the system in a random way. This will lead to the formation of a larger cluster that, at some point, will span the complete system, which will indicate the percolation point, which here corresponds to the gelation point.

2.5 Drying of colloidal suspension drops

When a colloidal drop is placed in contact with a solid substrate, a triple contact line is formed between the vapor, the liquid and the solid, as illustrated in Figure 2.8. The drop will spread mainly due to the three types of forces involved: the surface tension, the gravitational force and the viscous force [22].

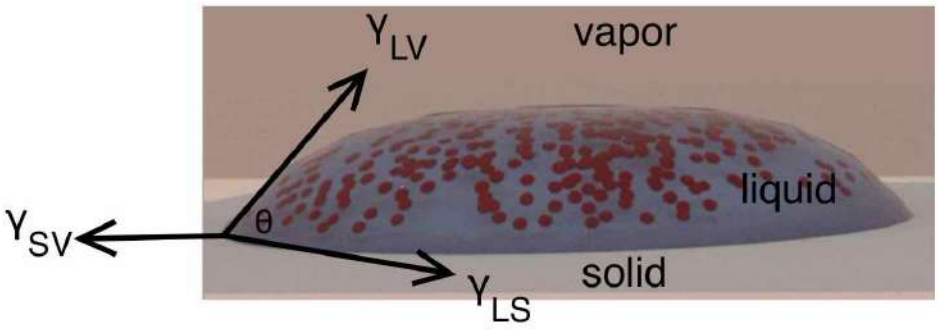

Figure 2.8: Contact angle θ at the three-phase contact line of a colloidal droplet. Surface energies of solid-vapor γ_{SV}, solid-liquid γ_{LS} and liquid-vapor γ_{LV}.

The total surface energy is minimal when the horizontal components of the surface tensions are in equilibrium. At this point the contact angle (θ_{eq}) can be determined by the Young equation:

$$\cos\theta_{eq} = \frac{\gamma_{sv} - \gamma_{sl}}{\gamma_{lv}} \tag{2.10}$$

where γ_{sv}, γ_{sl} and γ_{lv} are the surface energies of solid-vapor, solid-liquid, and liquid-vapor surfaces, respectively.

The coffee-ring effect

The evaporation of drops containing non-volatile particles dispersed in a volatile solvent might result in ring-like deposits along the perimeter [23–25]. This phenomenon is called coffee-ring effect and the resulting ring-like deposits are familiar to anyone who has observed a drop of coffee dried on a surface. The ring formation corresponds to a hydrodynamic process due to the capillary flow in the drop during drying.

The capillary flow can be understood as the flow that is compensating the solvent that has been evaporated, which is promoted by the differential evaporation rates across the interface of the drop during drying [23]. When a colloidal drop is deposited on an ideal substrate (flat, smooth and homogeneous) the evaporation rate at the edge of the drop is increased due to the pinning of the sample contact line. The increase of the evaporation rate induces the solvent to flow to the periphery of the sample in order to compensate the solvent that has evaporated, which results in a radial outward flow within the sample [26]. The radius of the drop usually remains unchanged, while the contact angle decreases. Once evaporation is finished, most of the particles are relocated at the periphery, thus forming a coffee ring at the perimeter of the droplet [22, 23, 26, 27].

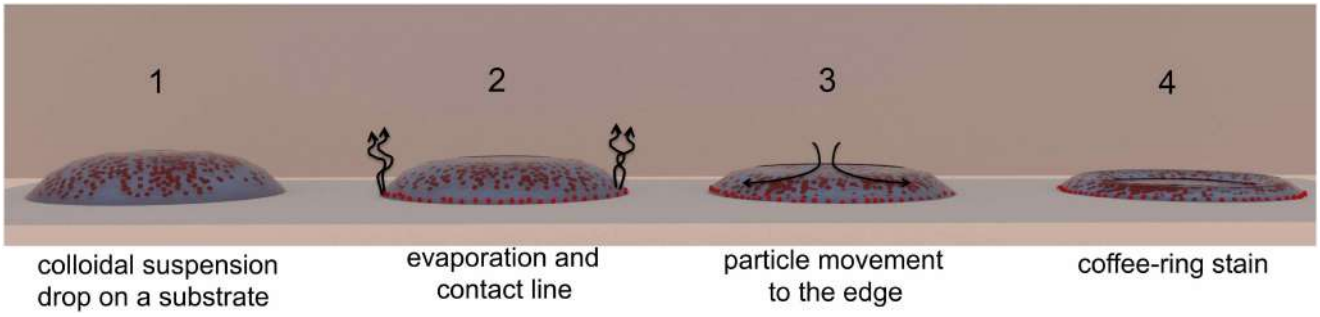

Figure 2.9: Drying of a colloidal suspension drop on a substrate. 1. A colloidal suspension drop is deposited on a flat substrate. 2. The contact line is pinned, as illustrated by the red particles at the edge of the drop. In addition, the local evaporation rate at the contact line is increased. 3. The radial outward capillary flow of water in the drop deposits particles in the periphery, creating a concentration gradient along the sample, resulting in the famous "coffee-ring" effect (4) after all water is evaporated.

2.6 Cholesteric cellulose nanocrystal suspensions

2.6.1 Cellulose

Cellulose is the main biopolymer found in nature and the dominant chemical component that is present in the fiber wall in plants. Cellobiose is the repeat unit, consisting of two glucose units, as shown in Figure 2.10 [28]. The glucose units in the cellulose matrix are linked together via β-1,4 glycosidic bonds in order to form linear polymer chains. Although cellobiose is considered to be the repeat unit of cellulose, the degree of polymerization is determined by the amount of total glucose units that build the cellulose chains. Native wood has an average degree of polymerization (DP) in the range of 9,000-15,000, which means that 15,000 monomeric glucose units are the main constituents of a cellulose chain. Cellulose molecules have the ability to form rather robust intra- and intermolecular hydrogen bonds due to the presence of highly

reactive hydroxyl groups, resulting in cellulose aggregates that are known as microfibrils. These cellulose aggregates can either form largely ordered crystalline structures, which are thermally stable and inaccessible by any chemical treatment, as well as completely disordered regions that are typically known as the amorphous part of the cellulose fiber.

The hydroxyl groups located at the surface of the cellulose fiber makes this polymer accessible to different polar solvents (e.g. water), giving the possibility to form hydrogen bonds as well as the chance to perform chemical modifications such as esterification and oxidation [29], largely important for the preparation of cellulose nanocrystals.

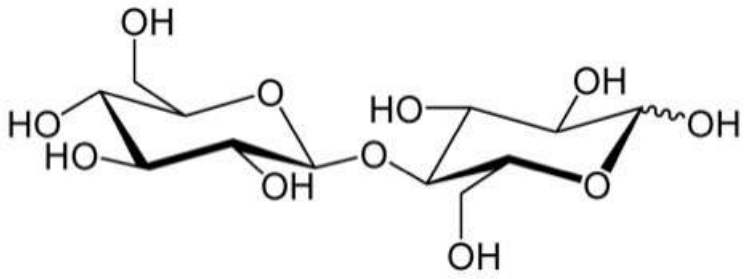

Figure 2.10: Chemical structure of cellobiose, consisting of two molecules of glucose.

2.6.2 Preparation of cellulose nanocrystals

CNCs have attracted much interest, largely due to their ability to develop a fluid yet ordered liquid crystal phase in aqueous suspensions. This is thanks to the high aspect ratio of the rods and the charges introduced after the acid hydrolysis of an initial cellulose suspension.

In 1959, Marchessault *et al.* [30] reported the formation of birefringent aquous gels of microfibrils of acid-treated cellulose and chitin, respectively at high mass fraction, although no textures indicative of helicoidal arrangements were observed. Revol and Gray *et al.* [31] reported *in vitro* self-organization aqueous CNC suspensions of lower mass fraction into stable chiral nematic phases.

CNCs can be prepared by hydrolysis with sulfuric acid of natural cellulose sources such as cotton, wood, bacteria and tunicates [1, 32–35]. A cellulose microfibril contains disordered amorphous regions as well as crystalline parts. The acid degrades the amorphous regions, leaving the CNCs as rod-like particles [36]. Due to the sulfuric acid based hydrolysis, negative charges are incorporated on the rod surface [37, 38], corresponding to the sulphate half-ester groups (SO_3^-) shown in Figure 2.11. The surface charges promote the colloidal stabilization of CNC suspensions, and together with the anisotropic rod-like shape, permit the formation of liquid crystalline phases.

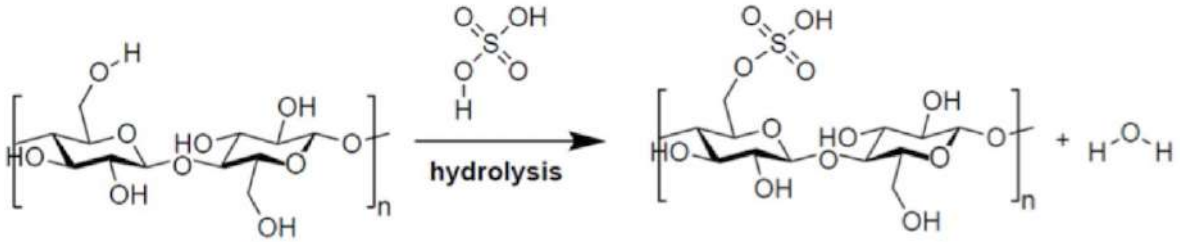

Figure 2.11: Esterification of the hydroxyl group during cellulose hydrolysis via sulfuric acid.

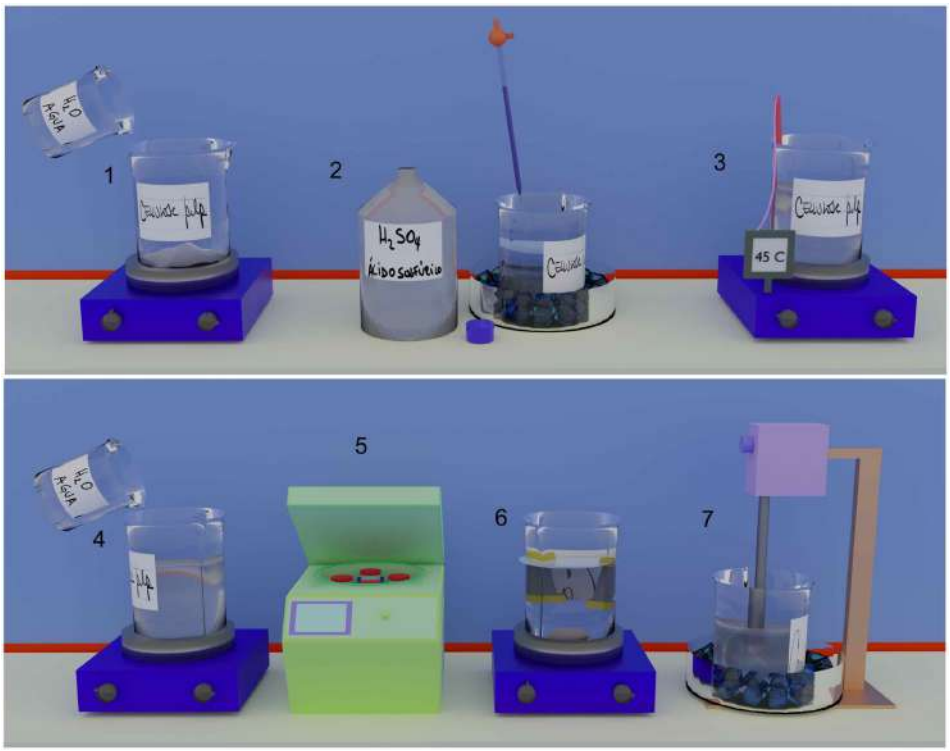

Figure 2.12: Preparation of cellulose nanocrystals on laboratory scale. 1) A cellulose suspension is dispersed in a sulfuric acid/cellulose mass ratio of 8.7 at 45°C (2-3), stirring for 1 h. The reaction is then stopped by the addition of ultra pure water (4) followed by centrifugation with a large excess of fresh water (5). The centrifuged suspension is subsequently purified using dialysis membranes in ultra pure water that was exchanged every 8 hours during 4 days (6). After the purification step, the CNC suspension is sonicated (7) in order to break down the CNC aggregates into individual rods.

CNCs present high aspect ratio L/d, typically with diameter d in the range of 5-10 and length L between 50-1000 nm [14], depending on the cellulose source and the preparation conditions with which the rods are produced.

Before the purchase of commercial CNC from Forest Product Lab (FPL), I prepared our own CNC suspensions using cotton and wood pulp as the main cellulose sources, results that were part of our first scientific publication [38]. The schematic illustration of the preparation process is presented in Figure 2.12. We start by dispersing a certain amount of the cellulose source in a sulfuric acid/cellulose mass ratio of 8.7 at 45°C, stirring for 1 h. The reaction should then be stopped by the addition of ultra pure water followed by centrifugation with a large excess of fresh water. The centrifuged suspension is subsequently purified using dialysis membranes in ultra pure water that was exchanged every 8 hours during 4 days. After the purification step, the CNC suspension is sonicated in order to break down the CNC aggregates into individual rods. Figure 2.13 presents a representative AFM images of a cotton-derived CNC suspension before and after sonication. It can be observed that the CNC aggregates are broken down due to sonication, resulting in a final sample with individual rods.

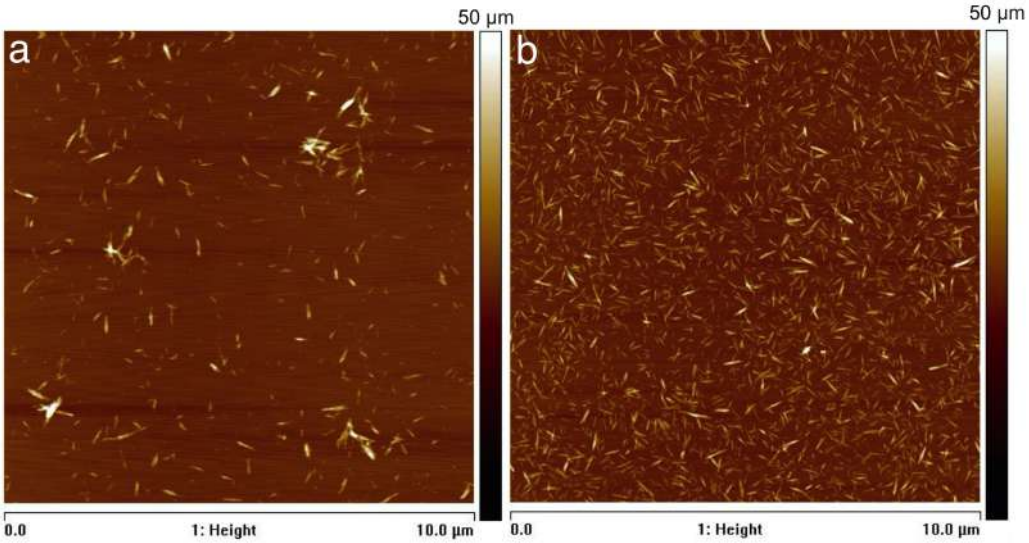

Figure 2.13: Effect of sonication on a cotton-derived CNC suspension. a) Unsonicated cotton-CNC after dialysis process and b) individual rods after sonication. The initial CNC mass fraction was 0.017 wt.% for both images.

The final CNC sample is stabilized in water due to the negative-half ester groups (SO_3^-) on the surface, with protons as counterion (H-form CNC) if no further treatment is carried out.

2.6.3 Determination of the concentration of sulphate half-ester groups

In order to determine the concentration of the sulphate half-ester groups introduced after the acid hydrolysis in the CNC sample, I followed the procedure presented by Beck *et al.* [39] and largely discussed in our scientific article [2]. In their work, the authors reported in detail the determination of the rod surface charges by conductometric titration with a rapid sample preparation method. This allows quantitative and precise determination of the sulfate half-ester content of CNCs, regardless of the counterion nature in the sample [39]. The experimental procedure consists of the following steps:

Dialysis

Commercial CNCs are typically in sodium-form (Na-CNC) rather than in H-CNC, due to the addition of NaOH after the acid hydrolysis. Because of this, dialysis previous to the determination of the sulphate groups is highly recommended for the removal of dissolved ions, including the residual sulfuric acid from the hydrolysis [28, 37]. The CNC sample is diluted to 1.5 wt.% and filled into cellulose membrane tubes. Then, an extensive dialysis process is carried out against pure water (conductivity of 0.055 μS/cm) for five days, with daily exchange of water [38].

Protonation of cellulose nanocrystals

H^+ form resin (DOWEX 50WX8, Sigma Aldrich) is used to replace the Na^+ cations in order to completely protonate the CNC sulphate half-ester groups. The resin is slurried in ultra pure water and poured into a glass column (inner diameter 2.5 cm) with fritted glass disk at the bottom. A resin bed height of 16 cm is prepared with 40 g resin. Before feeding the column with CNC suspension, the ion-exchange resin is rinsed with 1 L of ultra pure water until the eluate is colorless, with a pH identical to the wash water. A CNC suspension is fed from the top at a mass fraction $w = 0.5$ wt.% yielding a pH after the ion-exchange of 2.7. The CNC mass fraction after the column is $w = 0.5$ wt.% confirming no loss of sample [2].

Conductometric titration

CNC samples were prepared with 150 mg of H-CNC (protonated CNC, after the ion-exchange column) in a total volume of 200 mL (with the addition of ultra pure water). In order to increase the initial conductivity of the diluted CNC, 2 mL of 0.1 M NaCl solution is added and

then the obtained suspensions are titrated with 10 mM NaOH using a titrator system. The titrator system is equipped with conductivity and pH sensors together with an automatized system that allows the addition of small volume of titrant (in this case, NaOH) to the CNC suspension within a certain amount of time. In addition, this device plots the conductivity against the volume of added NaCl, identifying the equivalence point (E_p) that is necessary for the determination of concentration of the sulphate groups. This is discussed in Chapter 3. The NaOH solution is added in 0.1 mL increments over a period of 20 min. Three different CNC samples were titrated and the average result is the final sulfur content [2].

Estimation of equivalence point in CNC suspensions from conductometric curves

Figure 2.14 shows a typical conductometric titration curve of a CNC suspension. The equivalence point E_p can be determined from the linear intersection of the data points in the three different regions of the conductometric titration curve [37]. Prior to the addition of NaOH, the conductivity is high due to the presence of highly mobile hydrogen ions in the CNC suspension. Once the NaOH is added, the conductivity drops due to the replacement of the protons H^+ by the added cations (Na^+) from the base. Simultaneously, water is formed due to the reaction of the OH^- ions from the NaOH with the H^+ ions from the CNCs. This decrease in the conductivity continues until the sulphate groups have been completely neutralized, which corresponds to the equivalence point [2].

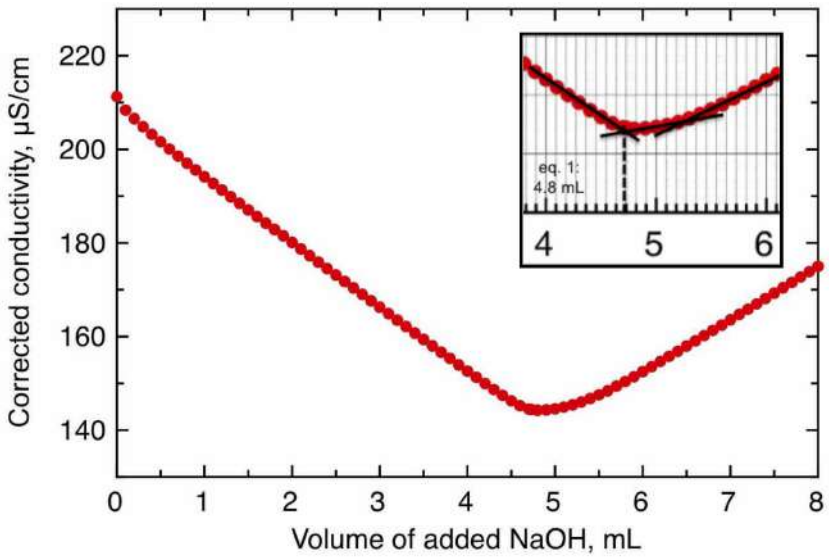

Figure 2.14: Example of a conductometric titration curve for dialyzed and protonated CNCs. The inset corresponds to the equivalence point determination, with a value of 4.8 mL.

2.6.4 Determination of diameter, length and aspect ratio of cellulose nanocrystals

Atomic Force Microscopy (AFM) is used for the size characterization of the CNC rods. A 20 μL aliquot of cationic poly-L-lysine solution (0.01 vol.%) is placed on a freshly cleaved negative charged mica surface (NanoAndMore GmbH) in order to make the surface cationic. Subsequently, the mica surface is rinsed with ultrapure water and dried with compressed air. The CNC suspension is then diluted to $w = 0.002$ wt.% in order to observe individual rods, and of this suspension, 20 μL is placed on the treated surface for 3 minutes. The sample is then rinsed with ultrapure water and pre-dried with compressed air, followed by transfer to a vacuum oven at 40°C for complete drying overnight. A Multi-mode V AFM (Digital Instruments Nanoscope Veeco) is used in tapping mode to image the samples [2].

Analysis of AFM data

I performed accurate measurements of diameter d, length L and aspect ratio L/d for the CNC rods by carrying out single profile measurements with the software $WSxM$ [2]. To get a truly representative measure of d, the commonly used method of measuring an AFM height profile perpendicular to each rod at some randomly chosen crossing point was insufficient, due to the considerable height variations along every individual CNC rod (inset in Figure 2.15. Instead, the height profile was measured along each rod r and the average value is used as its diameter, d_r. For each sample, at least 100 rods are measured individually and by averaging d_r obtained for each of these, thus a final representative diameter value d was determined for that particular CNC sample.

To obtain the length L_r of each rod regardless of its orientation in the sample plane, I used the extension of the rod in the lab frame's x and y directions, Δx_r and Δy_r, which are directly available from the height profile data. We then apply the Pythagorean theorem to calculate the length as $L_r = \sqrt{\Delta x_r^2 + \Delta y_r^2}$, as indicated in Figure 2.15. An average length value $\overline{L}$, representing the CNC sample, is again calculated as the average of all L_r values established for the total amount of rods. Finally, for each rod r I determined the aspect ratio as L_r/d_r, and the aspect ratio chosen to represent the sample is the average $\overline{L/d}$ of all the individual rod aspect ratios [2].

2.6.5 Estimation of energy transferred to the CNC suspension during tip sonication

The energy introduced by the sonication was calculated according to the procedure at http://www.sonicator.com/literature/faq.html. The delivered power under continuous (c) operation, as measured by the device, was indicated to be $P_w^c = 37$ W with the tip immersed in 50 mL water (w), under the same conditions as during CNC sonication. With the tip in air (a), the corresponding reading was $P_a^c = 4$ W. From this we calculate that the continuous power to the sample (s) would be $P_s^c = 33$ W. However, the CNC suspensions were sonicated using a $\chi = 30\%$ pulse setting, and the total sonication time was $t = 70$ s. Hence, the total energy delivered to the suspension (containing 6 wt.% CNC) can be calculated as $E_s = P_s^c \chi t = 33$ W $\cdot$ 0.3 $\cdot$ 70 s = 690 J. With a suspension volume of 50 mL this yields an energy of 14 J/mL suspension, or 0.01 kJ/mL adjusted for the accuracy in the power measurement [2].

2.6.6 Determination of the chiral nematic pitch of CNC suspensions

Polarizing optical microscopy (POM) is one of the most important tools for the characterization—and detection—of the cholesteric phase in aqueous CNC suspensions studied in this thesis. With the POM we can observe and image samples due to their optical anisotropy. If the pitch p is larger than 1 micron, we will see a cholesteric fingerprint texture (if the helix axis is along the surface) with continuous separations when imaging the sample in a polarizing microscope (Figure 2.16). The distance between two adjacent stripes is $p/2$. Nevertheless, a CNC sample (or chiral nematic samples, in general) filled in a glass capillary might exhibit a different appearance depending on the location of the helix axis (either parallel or perpendicular to the

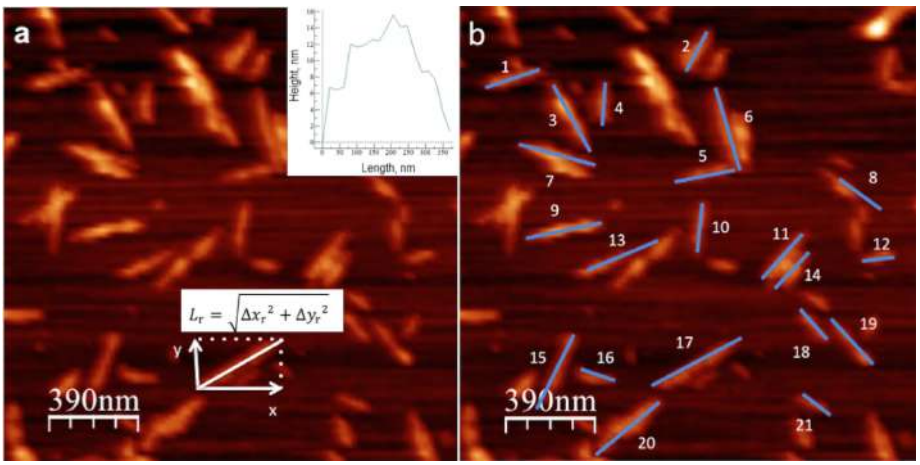

Figure 2.15: AFM images of a random CNC sample as example of the determination of diameter d, length L and aspect ratio L/d of CNC rods. From Honorato–Rios *et al.* [2].

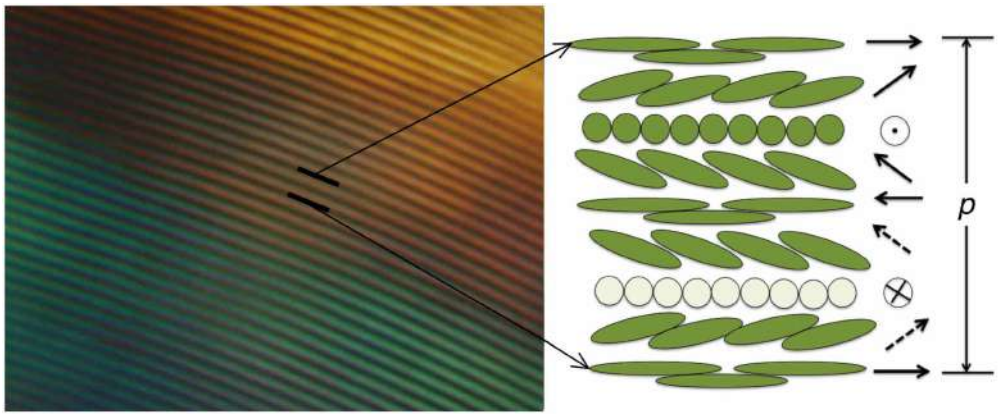

Figure 2.16: Typical fingerprint texture that CNC suspensions form (the chiral nematic phase) in sealed glass capillaries and observed in POM. The periodicity of the helix is given by $p/2$, which can be determined by the distance between two of the adjacent stripes.

glass), and on the size of the pitch [4, 38].

For the determination of the pitch, 5 cm long capillaries with rectangular cross-section of 0.20 mm x 4.0 mm, were fed with the CNC suspensions [38]. Both extremes of the capillaries were sealed and later stored at room temperature for minimum one month before imaging. The half pitch values were determined by measuring two consecutive lines in the fingerprint texture. Images of the liquid crystalline CNC suspensions between crossed polarizers were obtained using an Olympus BX51 microscope in transmission mode, together with an Olympus DP73 camera.

2.6.7 Establishing the phase diagrams

From our previous work [2,38], in order to establish the phase diagram of the CNC suspensions, we first prepare series of relevant mass fractions w obtained by concentrating the different CNC samples using mechanical stirring at room temperature. Once the concentration is high enough ($\approx$ 12 wt.%), the sample is diluted with deionized water until the different mass fractions are obtained. Once phase separation is complete, the volume fraction of LC phase (Φ) is determined by the ratio of the LC phase height divided by the height of the full sample (LC and isotropic) from images of the vials capture between crossed polarizers. All samples vials need to be standing vertically for minimum 1 month before characterization [2].

2.6.8 Characterization of CNC films

Circular polarization

An Olympus BX51 polarizing microscope in reflection mode was used for the investigation of the optical properties of the films. For the detection of circular polarization, a quarter wavelength retardation plate was inserted between the crossed polarizers. The analyzer is rotated for right- and left-handed circular polarization, respectively.

Scanning Electron Microscopy (SEM)

In order to investigate the self-organization of the rods after the films were formed, I used SEM imaging of the cross section for the most interesting samples. First, the CNC film was fractured by making a line on the glass substrate that holds the film followed by cracking both the glass and the sample. Half of the film was then placed on a holder by using a carbon tape. What is important here is that the surface that needs to be imaged has to be properly oriented so that the surface that has been fractured should have the same orientation than the direction of imaging [40]. The surface was coated with a thin gold layer (9 nm). SEM images of the fracture surface were captured with a JEOL (JSM-6010LA) electron microscope at operating voltage of 10 kV, a sample-to-lens working distance of 10 cm and the filament temperature held at 130°C.

Surface profilometry

The different height measurements of the profile of the CNC films were carried out using a stylus profilometer (Dektak XT, from Bruker), with a 12.5 μm tip radius at 3 mg force, and a 0.28 μm/pt. Every individual scan was performed along the complete sample, always aiming for the center of the film.

Chapter 3

Commercial cellulose nanocrystals from Forest Products Lab

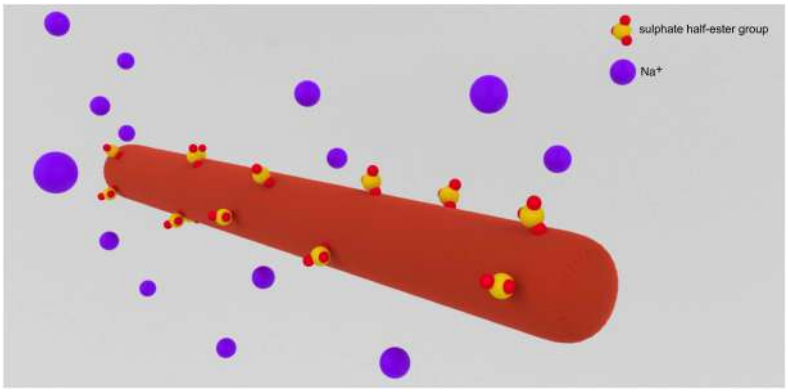

Overview of the chapter

This chapter provides information about the characterization of the commercial CNC produced at the Forest Products Lab (FPL) and supplied by University of Maine, USA. Commercial CNC is increasing in popularity in different research fields and has been extensively used in this thesis. The nanorods are extracted by acid hydrolysis from a wood cellulose source, with the peculiarity of being a sodium form CNC (Na-CNC). Details of their production procedure are provided at https://umaine.edu/pdc/cellulose-nano-crystals.

3.1 Introduction

The CNC preparation method includes straightforward chemistry and purification steps, but if the protocol is not carried out correctly, it can happen that the final CNC sample will not develop liquid crystalline phases. In addition, the yield of the process is ∼50% [35, 41] (depending on the hydrolysis conditions), meaning that around half of the initial cellulose mass is lost during the procedure. This makes the preparation of larger amounts of CNC a tedious and time consuming process, the limitation in common research labs.

The work on CNCs in this thesis is primarily focused on understanding the self-organization of the rods in aqueous suspension and the further preparation of solid films upon the evaporation of water. Because of this, the use of commercial CNC is very convenient considering the large amounts of suspension that are needed from the same starting batch. However, if any of the steps involved in the CNC purification is not properly carried out, it could lead to the presence of extra ions in the final suspension. These extra ions might impact the final behavior of CNCs, such as the phase diagram [42], chiral nematic pitch [38] and the film formation [34].

Although the use of commercial CNCs has become popular among researchers, the lack of information provided by the suppliers renders the migration from the lab CNC to the industrial product potentially problematic, especially since the exact cellulose source, the extraction process and purification is not completely obvious [43]. In this chapter, I present some basic characterization of a wood-derived CNC suspension from Forest Lab products (FPL). Furthermore, the as-received CNC was purified by dialysis followed by an ion-exchange process and finally I compared both suspensions in terms of phase diagram and chiral nematic pitch.

3.2 Characterization of CNCs from FPL

3.2.1 Size distribution of a CNC suspension from FPL

CNC dimensions were determined by carefully measuring the length L and diameter d of 300 individual rods from AFM images (details of the procedure in Chapter 2, subsection 2.6.4). Figure 3.1 presents L, d and aspect ratio L/d described by log-normal distributions. This fitting function is typical for polymers [44] as well as for colloidal particles with large size dispersity [45]. The log-normal distribution only considers positive values of the variable. In contrast, when fitting a normal Gaussian distribution to the same data sets, as largely reported in the CNC field, a significant part of the distributions tails into negative values, leading to unrealistic variable distributions. However, if a transformed variable is created by taking the logarithm of the original data, the "new" values seem to have a normal distribution. Let us say that x is the original variable and that $y = log(x)$ has a normal distribution. Then we can say that x has a log-normal distribution.

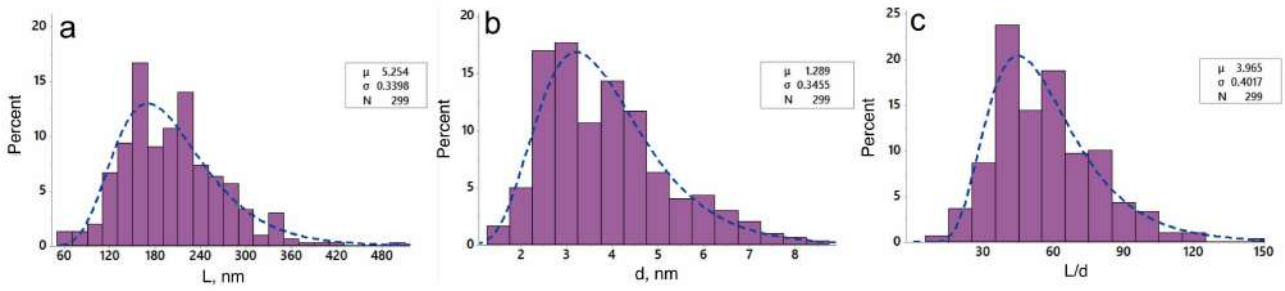

Figure 3.1: a) Log-normal distribution of length L, b) diameter d and c) aspect ratio L/d of a CNC fraction sonicated from FLP. The same sonication conditions are used in all the experiments carried out in this thesis. More details concerning sonication are discussed in Chapter 2, subsection 2.6.5. The insets present the values of μ and σ, corresponding to the mean and standard deviation of the natural logarithm of the variable, respectively. Finally, N indicates the number of individual rods measured from AFM images.

The mean value of the variable, $\bar{x}$, can be calculated from the log-normal distributions [46] according to:

$$\bar{x} = \exp(\mu + \sigma^2/2), \tag{3.1}$$

where μ and σ correspond to the mean and standard deviation of the natural logarithm of the variable, respectively. The quantity σ determines the relative width of the log-normal distribution [45], thus σ provides relevant information of the dispersity of the variables. Values of dispersity will be largely presented in this thesis for comparison between CNC fractions.

Previous to the AFM analysis, the sample was slightly sonicated (details in Chapter 2, subsection 2.6.5) in order to obtain individual particles with clear boundaries, resulting in values of $\bar{L} \approx 0.2$ μm with $\sigma_L \approx 0.3$ and $\bar{d} \approx 4$ nm with $\sigma_d \approx 0.3$. If I now consider $\overline{L/d}$ as the average of 300 individual aspect ratios, the mean value results in $\overline{L/d} \approx 57$ and $\sigma_{L/d} \approx 0.4$. If now the mean is presented $\overline{L/d}$ using, instead, the $\bar{L}$ over the average $\bar{d}$ of all particles (Figure 3.1a,b), L/d decreases from 57 to 50 for the same CNC sample. These differences emphasize the need of detailed descriptions of experiments and of data analysis, which could result in better comparison between studies.

Reid *et al.* [43] reported a relatively narrow distribution of L of an as-received CNC sample from FLP (unsonicated suspension), with most of the CNC rods in the range of 0.1 – 0.2 μm. The authors pointed out that aggregates were not measured since the exact boundaries of individual CNCs were not distinguished. Although I agree with this strategy, the amount of CNC bundles in the sample is not negligible as it can be seen in the AFM image in Figure 3.4a. In the case of the CNC samples utilized in this thesis, the majority of the particles exhibits L between 0.12 – 0.25 μm (Figure 3.1b). The increase in L compared to Reid *et al.* can be a consequence of sonication; the rods that form bundles are released after the treatment. This way I have access to more individual rods (and apparently longer rods from the bundles) suitable to be measured, increasing the final average length.

Figure 4.5 shows the pH and conductivity curves for the as-received CNC. The pH varies in the range of 6 – 7 depending on the CNC mass fraction, with the variation in pH attributed to dissolved CO_2 from the atmosphere [47]. Values of pH close to 7 indicate that the sample has been neutralized by adding a base (in this case NaOH as reported by the supplier) as shown in Figure 3.3, resulting in a sodium–form CNC (Na-CNC). Despite the fact that conductivity values can provide important information about the presence of ions in the suspension, I did not succeed in finding literature with conductivity data of Na-CNC suspensions. However, obtaining a straight increasing behavior of conductivity upon increased content of CNC is expected, if I consider that the counterions attracted by the sulphate groups are proportional to the CNC content. More details will be presented in Chapter 6.

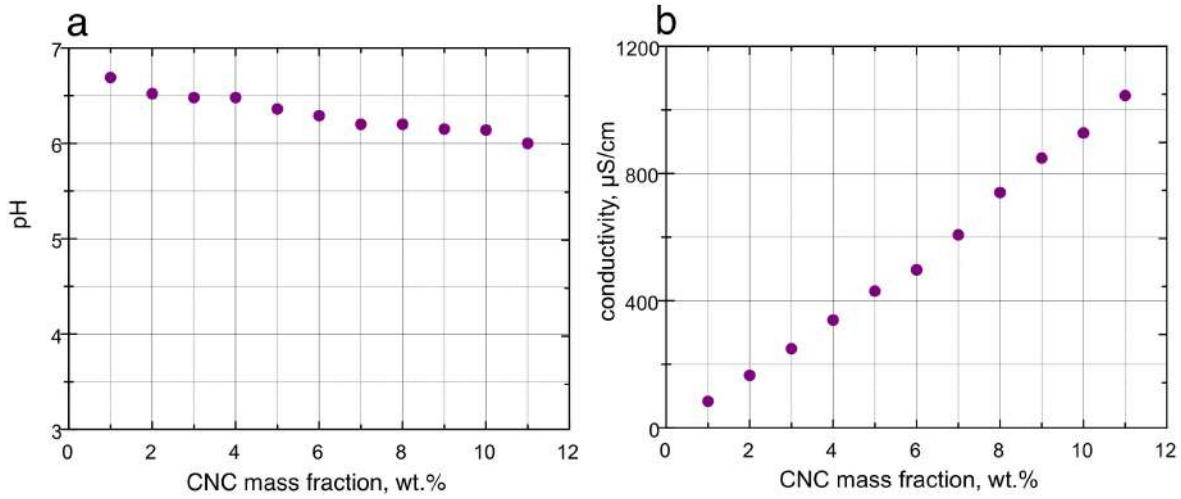

Figure 3.2: (a) Values of pH and (b) conductivity of the as-received CNC. From Honorato–Rios *et al.* [2].

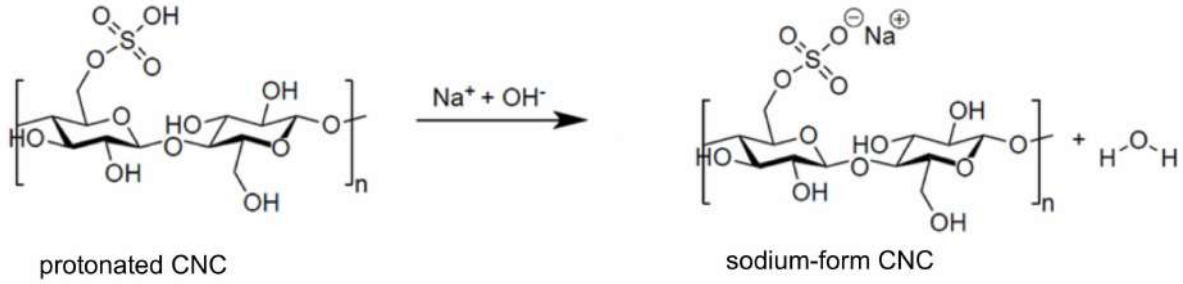

Figure 3.3: Neutralization of protonated CNC (H-CNC) by the addition of NaOH.

3.2.2 Determination of sulfur content by conductometric titration

Forest Products Lab provides a standard value of sulfur content for all their CNC batches corresponding to 0.90 wt.%. To corroborate this value, the sulfate half ester (OSO_3^-) or the sulfur content was determined by conductometric titration. This process requires complete protonation of the CNC sample (only H^+ as counterions) for accurate results [48]. The titrations were carried out after an extensive dialysis and ion exchange resin treatment of the as-received CNC (details of the procedure in Chapter 2, subsection 2.6.3). Figure 3.4a presents a representative AFM image of the as-received CNC without any further treatment and Figure 3.4b shows the titration curves for the determination of the sulfur content by conductometric procedure.

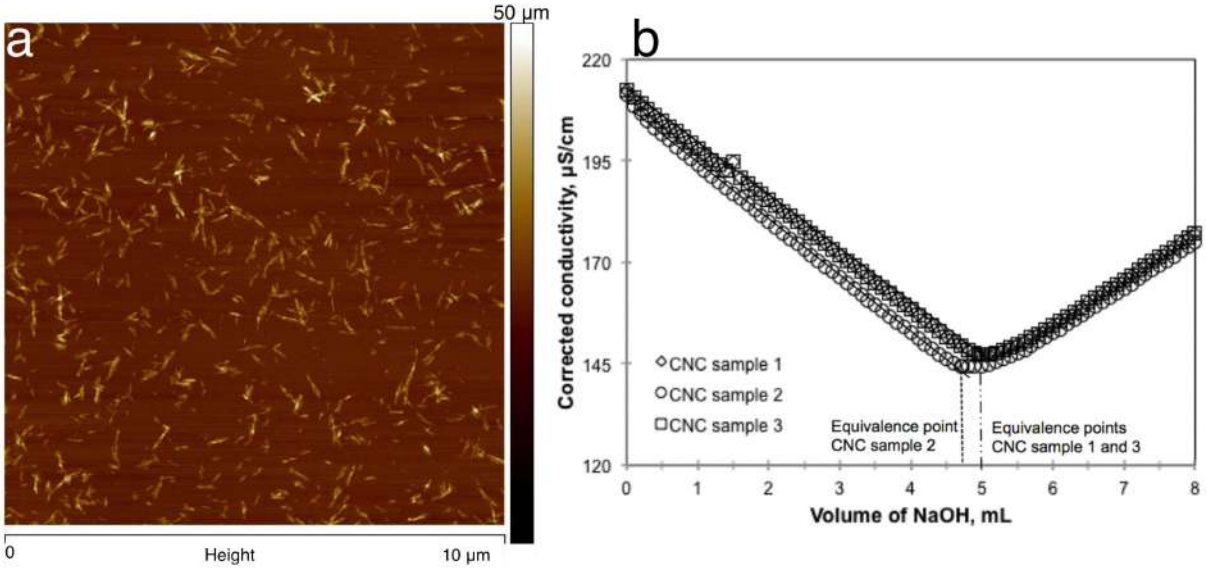

Figure 3.4: a) Representative AFM image of the as-received CNC and b) conductivity curves for the determination of the sulfur content for the as-received CNC purchased from FPL. From Honorato–Rios *et al.* [2].

The sulfur content of the as-received CNC was determined according to the expression:

$$m_s/m_{CNC} = \frac{E_p c_{NaOH} M_s}{m_{CNC}} \tag{3.2}$$

with m_s the mass of sulfur, E_p the equivalence point in mL and m_{CNC} the initial mass of CNC that is characterized.

From Figure 3.4b, E_p is determined from the first break in the conductivity curve. This value corresponds to the volume (in mL) of NaOH that needs to be added to the CNC suspension in order to completely neutralize the sample by replacing all the H^+ ions with the Na^+ ions from the NaOH. The titrations were conducted for three different samples and Table 3.1 presents the obtained results for each suspension.

Table 3.1: Determination of sulfur content in as-received CNC from FPL by conductometric titration of three CNC suspensions. From Honorato-Rios *et al.* [2].

Sample	m_{CNC}[mg]	Equivalence point, E_p[mL]	m_s/m_{CNC}
CNC 1	142	5.0	0.011
CNC 2	153	4.8	0.010
CNC 3	143	5.0	0.011

Based on the experiments it can be concluded that the sulfur content in the as-received CNC is, adjusted to the accuracy of c_{NaOH}, 1 wt.% by mass. The slight difference in sulfur content from the value provided by the manufacturer highlights the need to completely characterize all CNC samples prior to use. As I will demonstrate later in the thesis, even differences on the order of 0.1% can have significant consequences.

3.3 Purification of CNC from FLP by ion-exchange process

Commercial CNC suspensions from FPL contain sodium counterions as a consequence of the addition of sodium hydroxide for the acid neutralization. This corresponds to the last step of the production procedure in FPL [43]. Generally, experimental studies present results on CNCs prepared using their own protocols, with protonated rods as a result of the acid hydrolysis with sulfuric acid and without any further treatment. The presence of negative charges on the surface of the CNC crystals makes these samples extremely sensitive to any extra ions that could screen the charges, causing variation in the final phase diagram and chiral nematic pitch, both topics addressed in this thesis.

In order to confirm that no further purification treatment is necessary for these commercial samples, I attempted to purify the as-received CNC in a three-step process: dialysis, CNC protonation (using an ion-exchange column) followed by the addition of NaOH until pH 7. The ion-exchange process and the effect of counterions on the final samples are largely discussed in Chapter 6. This procedure ensures the removal of any extra ions that could have been introduced during the preparation procedure, resulting in a CNC sample with no other counterions but sodium ions in suspension.

Figure 3.5 presents the macroscopic phase separation and the phase diagram in pure water of the as-received CNC and its purified version after the three-step process discussed above. Prior to taking the image, the samples have been standing four months for the case of the as-received CNC and one month for the case of the purified CNC, resulting in a separation into a lower LC

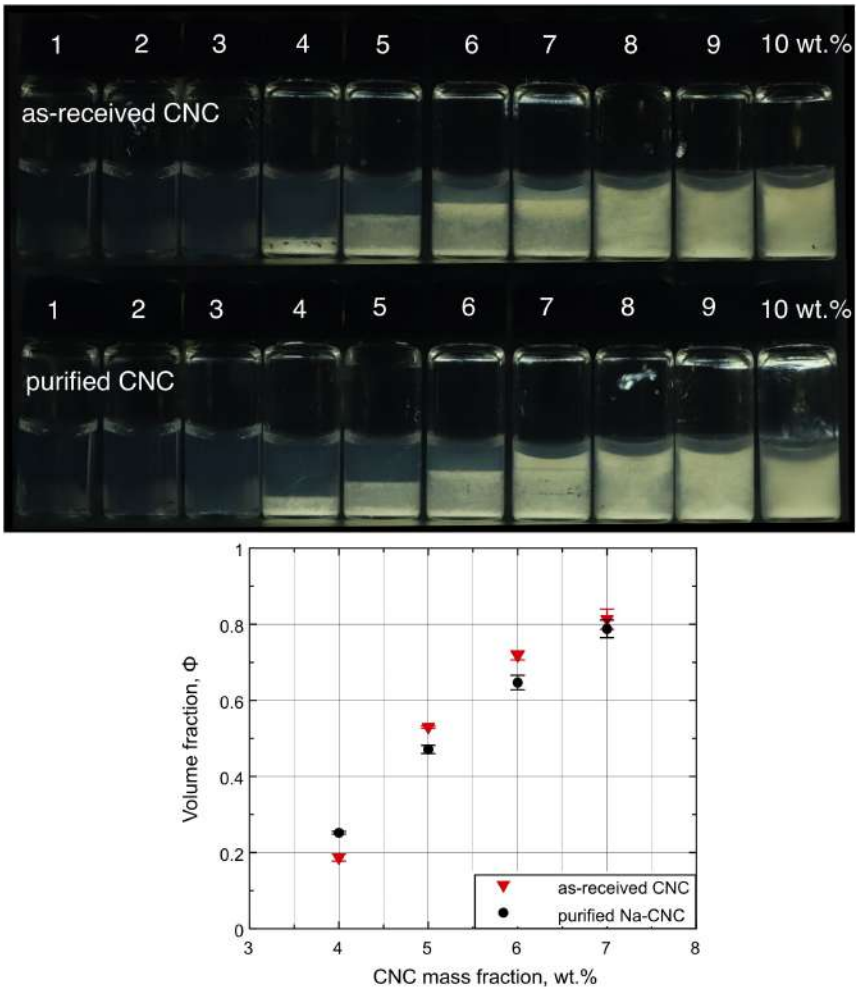

Figure 3.5: Phase separation, as observed between crossed polarizers, and quantitative plot of the volume fraction Φ for the as-received CNC and the purified Na-CNC after ion-exchange process.

phase and an upper isotropic phase for samples with an overall CNC mass fraction in the range from 4 wt.% to 7 wt.%. The upper phase scatters light in the macroscopic vials at 7 wt.% for the purified CNC, an indication that one month is not enough for a complete phase separation. From the quantitative plots of volume fraction Φ showed in Figure 3.5b, only slight differences in Φ are observed between the as-received CNC and the purified sample.

The chiral nematic pitch p for the as-received CNC and its purified version is presented in Figure 3.6, with the values measured from the fingerprint textures by polarized optical microscopy (POM). For both series, p decreases with increasing CNC mass fraction, as expected, with values between 6 μm to 9 μm for mass fractions between 5 wt.% and 9 wt.%. The differences in p between the as-received and the purified CNC are negligible.

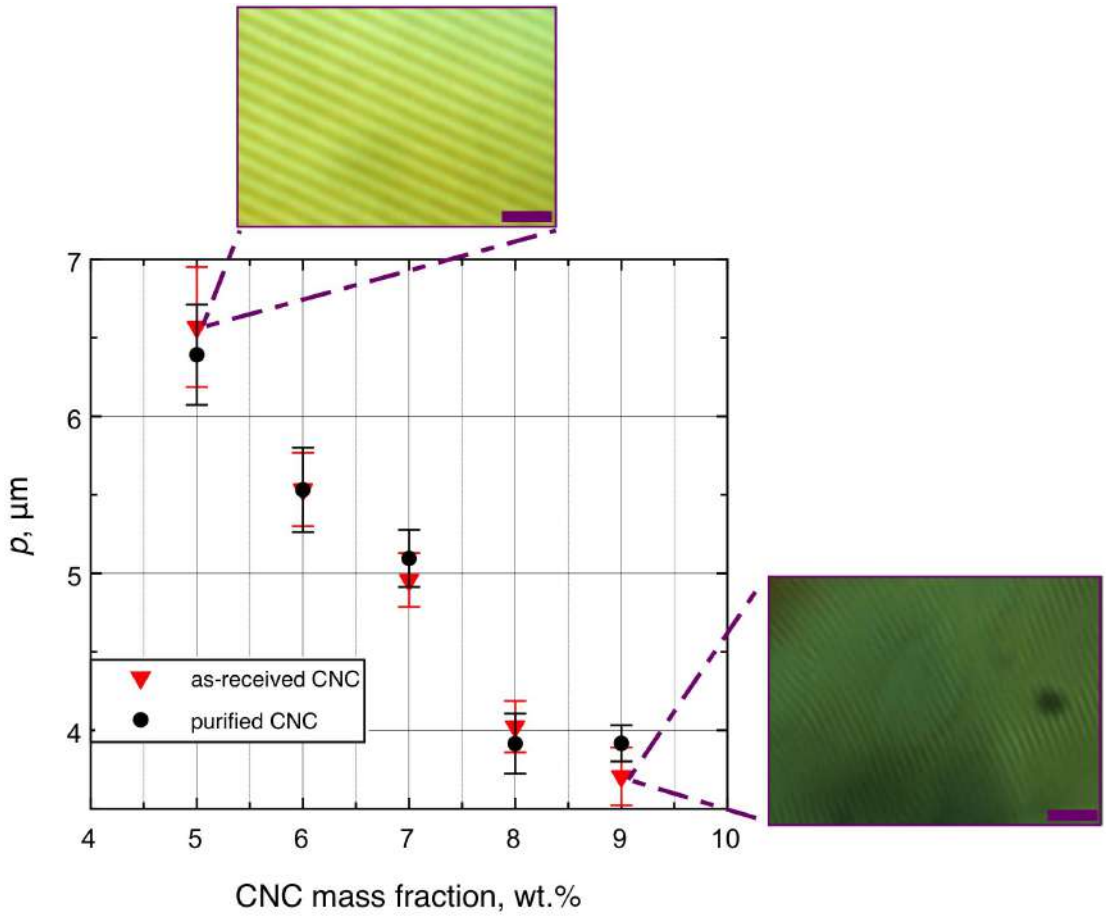

Figure 3.6: Chiral nematic pitch p for the as-received and the purified–CNC after ion-exchange process plotted against CNC mass fraction. The scale bars in the cholesteric fingerprint textures correspond to 5 μm.

3.4 Summary

The commercial CNC suspensions from Forest Lab Product (FPL) correspond to disperse sodium-form rods prepared via sulfuric acid hydrolysis prior to the neutralization with NaOH. They form cholesteric phases beyond a certain mass fraction, which is convenient for research applications. This chapter shows that the three-step purification process does not significantly impact the final behavior of the purified commercial CNC. Although minor changes in phase diagram were observed, these results suggest that the use of this commercial CNC (without further purification treatment) is a good alternative for colloidal and liquid crystal studies. Nevertheless, each new batch needs to be characterized, regardless of the specification given by the supplier.

Chapter 4

Fractionation of cellulose nanocrystal suspensions

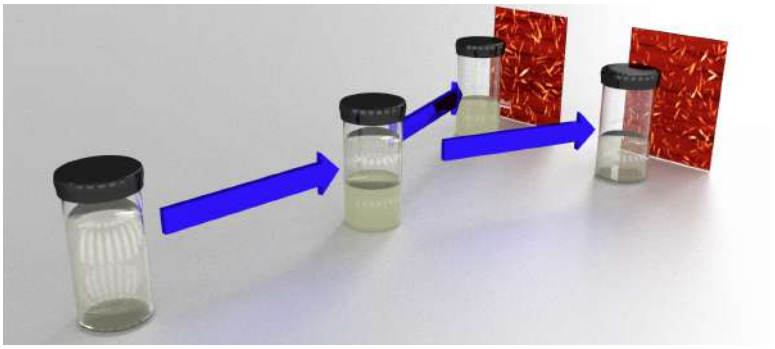

Overview of the chapter[1]

One of the main problems regarding the preparation of CNCs using a variety of cellulose sources, is the dispersity of the as-produced CNC rods. Many attempts in understanding the effect of the aspect ratio on the final CNC behavior have been previously reported [34, 49, 50]. However, the comparison between CNC batches prepared in different labs can be misleading, particularly due to the variation in surface charge density between samples. In this chapter, I present three different fractionation procedures by exploiting the spontaneous segregation that takes place according to the rod aspect ratio as the LC phase separates from the isotropic surroundings.

[1]This chapter is partially reproduced from Honorato-Rios, C. *et al.*. Fractionation of cellulose nanocrystals: enhancing ordering without promoting gelation. NPG Asia Materials, pages 1-11, 2018.

4.1 Introduction

After reaching a critical mass fraction, CNC suspensions are able to develop a liquid crystal (LC) phase which fits in the class of chiral nematic liquid crystals. The nematic order of CNC suspensions is originating from the rod-like particle shape and the ability to disperse the CNC rods in water. CNCs are dispersible in water because of the negatively charged sulphate half-esters on their surface, which have been introduced during the CNC preparation. Recall from Chapter 2 that the critical particle volume fraction for triggering the formation of a nematic phase is $\phi_0 = 3.3d/L$, and then the nematic phase, as it nucleates from the isotropic, has a distinctly larger rod volume fraction, $\phi_1 = 4.5d/L$, where d is the diameter and L is the length of the rod. A phase separation occurs when the overall rod volume fraction ϕ is between $3.3d/L$ and $4.5d/L$, with the nematic phase (with local rod volume fraction $\phi_1 = 4.5d/L$) sinking to the bottom of the sample and the isotropic phase (with local rod volume fraction $\phi_0 = 3.3d/L$) resting on the top.

The *phase* volume fraction Φ of a sample in the coexistence regime should increase linearly from 0 to 1 as the overall rod volume fraction ϕ increases from ϕ_0 (corresponding to a mass fraction w_0) to ϕ_1 (corresponding to a mass fraction w_1), as predicted by the basic Onsager model. In practice, however, the curve Φ versus w falls off sub-linearly with increasing CNC mass fraction. This is because an excluded volume must be added to the cellulose rods due to the electrostatic repulsion of the charged particles, which is increasing with increasing CNC mass fraction in the suspension. Experimentally it has been proven that suspensions of the commercial CNC quality that I use in this thesis, without additional modification can never reach a fully liquid crystalline state because $w_1 > w_g$, which means that the CNC suspension turns into a macroscopic gel, also known as a kinetically arrested state [4, 38, 43, 51–53].

In this chapter, I present different fractionation procedures with the main focus on the ability of CNCs to fractionate according to L/d. The effects of such fractionations on the final rod geometry and phase behavior are discussed. The dispersity effect on the phase separation diagram was investigated by comparing the result of the initial sample with those of the final fractions.

4.2 Liquid crystal-driven fractionation of CNCs

Pristine CNC suspensions are characterized by being disperse[2], with rods of considerable different L/d existing in suspension. Because high L/d favors liquid crystal (LC) formation according to Onsager, a sample with coexisting isotropic and LC phases has an increased representation of long and slender rods in the LC phase, whereas low L/d rods preferentially end up in the isotropic phase [2, 17, 54], as observed in Figure 4.1.

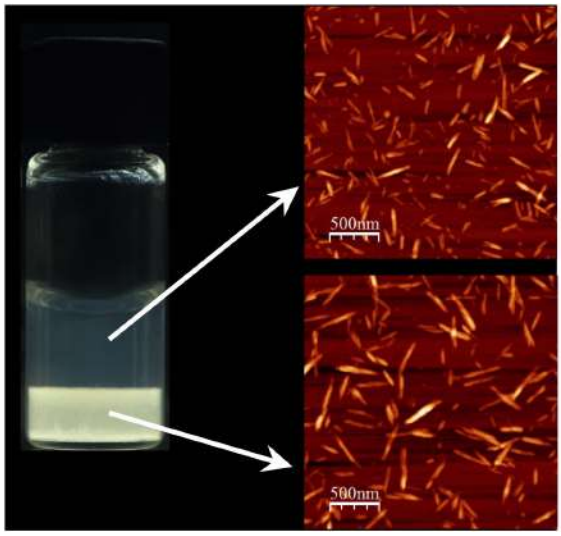

Figure 4.1: Phase separation of a 5 wt.% cotton–derived CNC suspension. The liquid crystalline (LC) phase in the lower part contains of rods with high aspect ratio, while rods with low aspect ratio populate the isotropic phase (in the upper part). On the right, representative AFM images confirm the fractionation that takes place between the coexisting phases. From Honorato–Rios *et al.* [6]

.

If the volume fraction ϕ of rods is increased, starting from a fully isotropic suspension, the LC phase will separate out once the overall rod volume fraction reaches the stability limit of the isotropic phase, $\phi = \phi_0$, as nuclei, so-called tactoids or spherulites [31, 55–58]. Within the tactoid, the rod volume fraction has the higher value $\phi = \phi_1$, corresponding to the stability limit of the nematic phase. Since ϕ_0 decreases with increasing L/d, such separation is more likely for a small subvolume in which the average L/d happens to be higher than in the overall disperse sample, explaining the spontaneous separation. Tactoids grow and merge and eventually the macroscopic LC phase, with somewhat higher average L/d compared to the isotropic phase, sediments to the bottom due to its higher density [2].

After some time standing, the sample in the vial from Figure 4.1 phase separates into an upper isotropic and a lower liquid crystal (LC) phase. From the AFM images, one can observe a clear

[2]IUPAC recommends the use of the term *dispersity* as a measure of the heterogeneity of sizes of particles in a mixture, in replacement of *polydispersity*, extensively used in the CNC field.

evidence of the spontaneous segregation of particles, with the longer rods in the LC phase, while the shorter rods populate the isotropic fraction.

Although Gray and co-workers [31,59] noticed this segregation according to L/d in their initial CNC work, the first detailed study on liquid crystal-driven fractionation in disperse rod-like suspensions that I am aware of was reported for carbon nanotubes (CNTs) [60].

4.2.1 Fractionation by centrifugation

As a first attempt to fractionate CNC suspensions, an initial sample at w = 7 wt.% (Figure 4.3) was centrifuged using different rotation speeds ω and for varying periods of time, according to the procedure reported earlier for fractionation of CNCs [61]. An AFM image of one sample after centrifugation is shown in Figure 4.2. The image reveals that CNC rods aggregate during the centrifugation, affecting the suspension behavior and the phase diagrams [2]. Probably if the parameters for centrifugation were adjusted, it would be possible to obtain samples with less aggregation. However, aggregates were clearly visible for all centrifugation settings used in our trials. I thus ruled out the method of speeding up the fractionation by centrifugation, and instead waited until sufficient separation had been achieved by gravity alone.

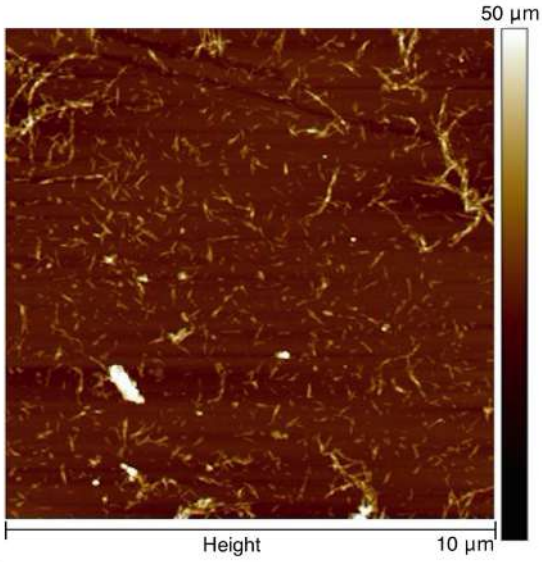

Figure 4.2: AFM image of a CNC sample at 7 wt.% after centrifugation. The conditions used for this sample corresponds to ω = 12,000 rpm and centrifugation time 60 min. From Honorato–Rios *et al.* [2].

4.2.2 Fractionation by separation of phases using a pipette

A series of CNC suspensions in the range of mass fractions between 1 wt.% and 11 wt.% (details of the preparation in Chapter 2) is presented in Figure 4.3. I will refer to this initial CNC sample as init-CNC. A starting suspension of CNC in water is prepared at 7 wt.% in the middle of the phase coexistence regime ($\Phi = 0.5$, i.e., isotropic and LC phase each comprises half of the macroscopic volume), and it is left standing until the two phases are macroscopically separated by gravity.

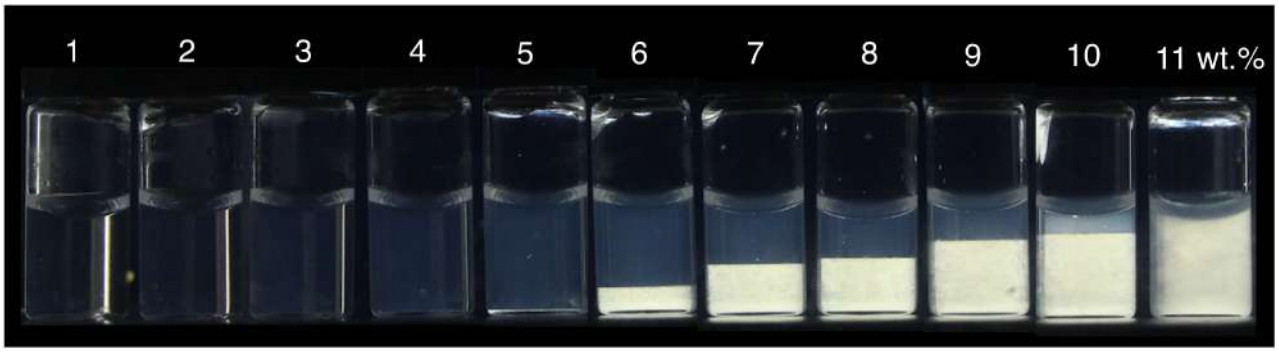

Figure 4.3: Phase separation in CNC suspensions for the initial series before fractionation (using a pipette) from a CNC mass fraction of $w = 7$ wt.%. The photograph has been taken between crossed polarizers. From Honorato–Rios *et al.* [2].

The isotropic supernatant phase is extracted using a pipette, and then the mass fractions of both samples are adjusted until they are again in the middle of the phase coexistence regime (water is evaporated from the isotropic fraction and deionized water is added to the LC fraction). This cycle is carried out three times for the LC fraction and three times for the isotropic fraction as schematically illustrated in Figure 4.4.

The CNCs in the final fractions are referred to as $3i_p$-CNC (threefold isotropic fractionation) and $3a_p$–CNC (threefold anisotropic (LC) fractionation). The subscript p refers to *pipette*, considering its use for the separation of the LC phase from the isotropic part. It is important to keep in mind the subscript p for future discussion in the upcoming sections and chapters. Figures 4.5 a,b present representative AFM images of the CNCs in the final fractions ($3i_p$-CNC and $3a_p$–CNC). The analysis of the images reveals substantial geometrical differences between the rods of the two fractions (Fig.4.5c–e). As expected, the fraction obtained from repeated separation of the isotropic phase contains in average shorter rods ($3i_p$-CNC) than the fraction obtained from repeated separation of the LC phase ($3a_p$-CNC). Great care was taken to extract reliable quantitative data on rod length and diameter from the AFM investigations. From a population of 300 individual rods, the length mean in $3i_p$-CNC is $\bar{L}^{3ip} \approx 0.17$ μm with a dispersity of $\sigma_L^{3ip} \approx 0.3$, whereas in $3a_p$-CNC, $\bar{L}^{3ap} \approx 0.23$ μm with $\sigma_L^{3ap} \approx 0.4$. The $3a_p$-CNC fraction is actually more disperse in length, considering $\sigma_L^{3ap} \approx 0.4$ for $3a_p$-CNC against $\sigma_L^{3ip} \approx$

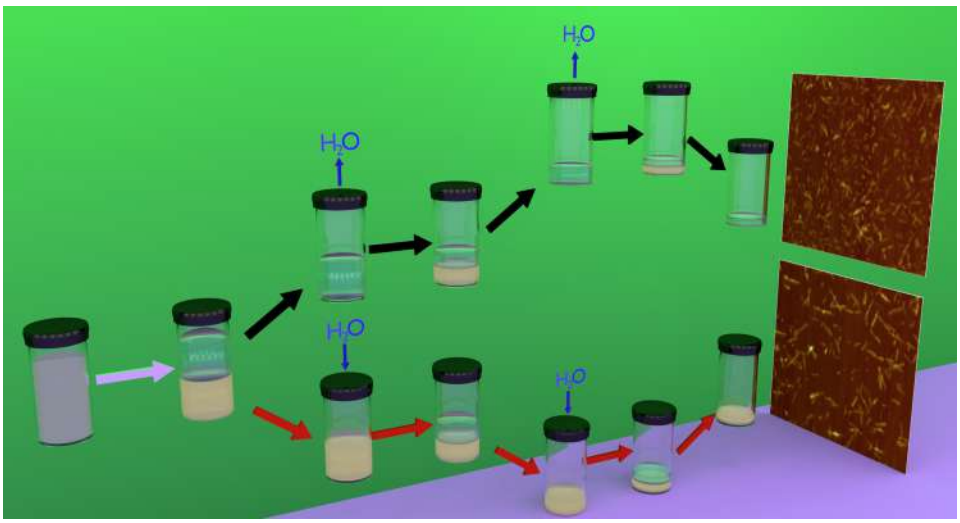

Figure 4.4: Schematic illustration of the fractionation method using a pipette. The black arrows indicate the path of the separations using the isotropic phases (transparent), and the red arrows indicate the path of the separation of the LC phases (turbid white). From Honorato–Rios *et al.* [2].

0.3 for $3i_p$-CNC.

Interestingly, the rod diameter remains approximately the same for all fractions, with a mean value of $d \approx 4$ nm; hence, the fractions are effectively separated by length. The mean of the aspect ratio (calculated as the average of L/d for 300 single rods) was 60 with $\sigma_{L/d}^{3ap} \approx 0.5$ for $3a_p$–CNC and 46 with $\sigma_{L/d}^{3ip} \approx 0.4$ for $3i_p$-CNC.

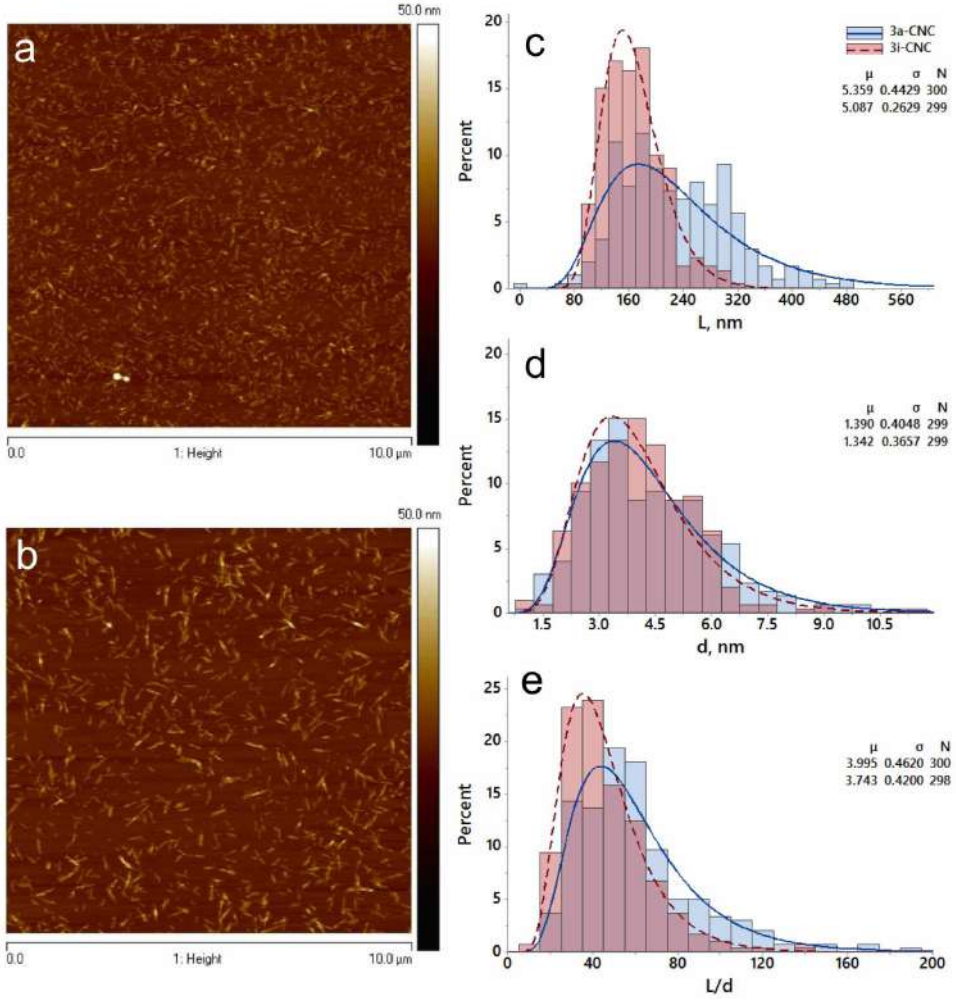

Figure 4.5: Characterization of fractionated CNCs. Left: representative AFM images of the two final CNC fractions, $3i_p$–CNC a) and $3a_p$–CNC b), after repeated phase separation. Right: Log-normal distribution of the length L c), diameter d d), and L/d e) for the two fractions, as determined from AFM data for 300 rods. Top values in insets: μ and σ of $3a_p$–CNC , corresponding to the mean and standard deviation of the natural logarithm of the variable, respectively. Bottom values in inset: μ and σ of $3i_p$–CNC, corresponding to the mean and standard deviation of the natural logarithm of the variable, respectively. Finally, N indicates the number of individual rods measured from AFM images. From Honorato–Rios *et al.* [2].

4.2.3 Fractionation procedure using a separatory funnel

One remaining challenge from the previous separation procedure is to prevent the separated phases from mixing during extraction. It is particularly difficult to avoid the contamination of the LC part by the isotropic phase. I present in this subsection an improved procedure that includes a separatory funnel (in replacement of the pipette) similar to the funnel illustrated in Figure 4.6. The stopcock located at the bottom allows a complete separation of the LC phase without any risk of contamination with the isotropic part during the process. To this end, the stopcock was closed while there was still a small amount of LC phase left. The separation of the isotropic phase from the LC fraction had been completed prior to this, with a pipette, following the procedure presented earlier in the subsection 4.2.2.

Figure 4.6: Schematic illustration of the separation of the LC fraction from the isotropic phase using a separatory funnel. A CNC suspension is filled into a separatory funnel (first funnel). A sharp boundary between phases is clearly visible after two weeks (second funnel). Finally, the stopcock is opened and most of the LC phase is drained out, closing the valve before reaching the interface with the isotropic layer (third funnel).

The as-received CNC in this procedure derives from the same CNC batch as the initial-CNC suspension in subsection 4.2.2 (both init-CNCs presented in Figure 4.3 and Figure 4.7). Nevertheless, the change in the macroscopic volume fraction Φ lies in small variations during sonication. I aimed at utilizing exactly the same conditions, without succeeding. In this case, a large batch was prepared in order to have enough material for the current procedure and for the fractionation that will be presented in the next subsection.

For fractionation, I filled a separatory funnel with a CNC suspension at 6 wt.% in the middle of the phase coexistance regime ($\Phi \approx 0.5$, Figure 4.7). The funnel was then closed to avoid

evaporation. The sample was left standing for two weeks until the phase separation was clearly visible. After this time, the top tap was opened and the isotropic upper half was then extracted from the LC using a pipette, leaving a thin layer of isotropic phase on top of the denser nematic part. Afterwards, the top tap was slightly closed and the LC phase released by gravitation from the remaining sample by slowly opening the stopcock located at the bottom of the funnel, which allowed to drain out exclusively the anisotropic phase. Following by either dilution or concentration of the separated phases, I carried out repetitive cycles with each new fraction adjusted to $\Phi \approx 0.5$.

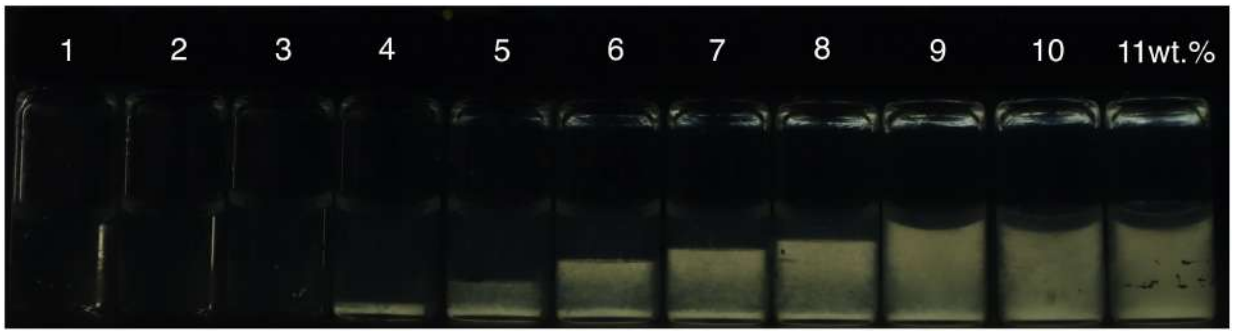

Figure 4.7: Phase separation of init-CNC series for fractionation of a CNC suspension starting at 6 wt.% ($\Phi = 0.5$) by repetitive separation of phases. The LC part was separated from the top phase using a separatory funnel. The same CNC series is used in the mass fraction-driven procedure in subsection 4.2.4.

The separation was extended to five cycles for the LC part (from now on represented as $5a_f$–CNC corresponding to fivefold anisotropic fractionation) and four times for the isotropic phase ($4i_f$-CNC, corresponding to fourfold isotropic fractionation). The subscript f refers to the *funnel* that was used in the separation of the LC phases.

The size characterization including the representative AFM images of two of the fractions ($5a_f$-CNC and $4i_f$-CNC) are presented in Figure 4.8. As expected, the fraction obtained from repeated separation of the isotropic phase contains on average the shorter rods compared to the fractions that resulted from the multiple separation of the LC phase. From a population of 100 individual rods, the length mean in $4i_f$-CNC is $\bar{L}^{4if} \approx 0.17$ μm with a dispersity of $\sigma_L^{4if} \approx 0.2$, whereas in $5a_f$-CNC, $\bar{L}^{5af} \approx 0.23$ μm with $\sigma_L^{5af} \approx 0.1$. The rod diameter remains approximately the same for all fractions, with a mean value of $d \approx 4$ nm; hence, the fractions are effectively separated by length. The mean L/d was 74 with $\sigma_{L/d}^{5af} \approx 0.2$ for $5a_f$-CNC and 55 with $\sigma_{L/d}^{4if} \approx 0.4$ for $4i_f$-CNC.

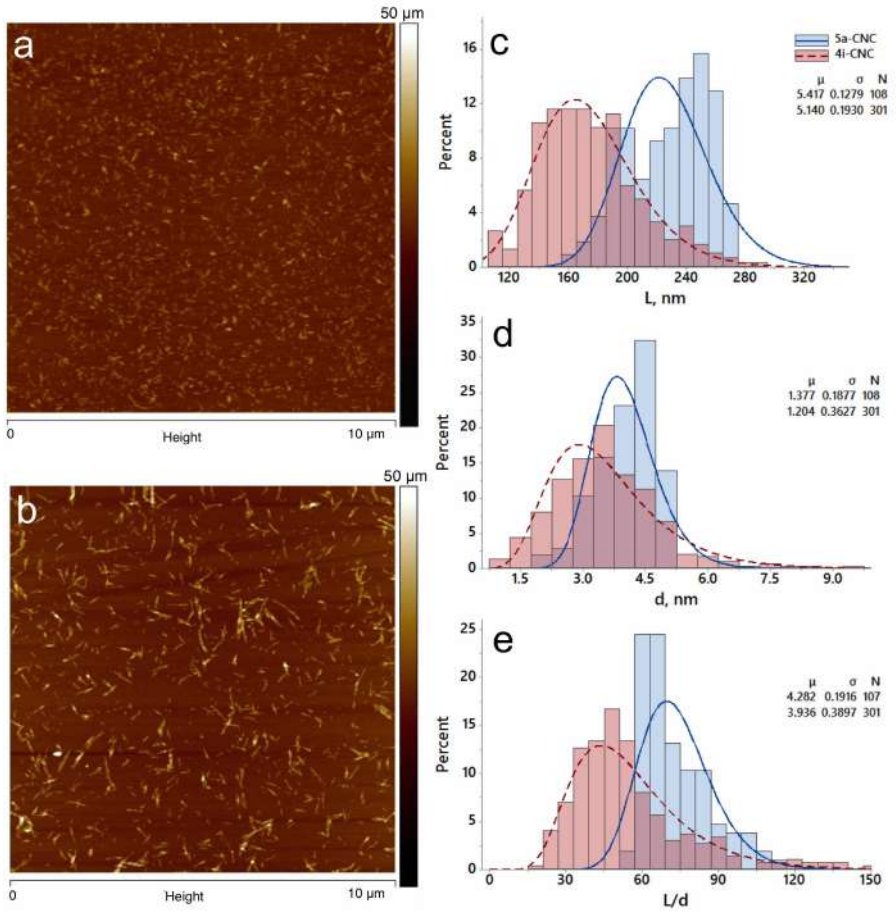

Figure 4.8: Characterization of short-rod CNCs. Left: representative AFM images of two final short rod CNC fractions, $4i_f$-CNC (a) and $5a_f$-CNC (b), after repeated phase separation. Right: Log-normal distribution of length L (c), diameter d, and L/d (e) for the two fractions, as determined from AFM data. Top values in insets: μ and σ of $5a_f$-CNC, corresponding to the mean and standard deviation of the natural logarithm of the variable, respectively. Bottom values in inset: μ and σ of $4i_f$-CNC, corresponding to the mean and standard deviation of the natural logarithm of the variable, respectively. Finally, N indicates the number of individual rods measured from AFM images.

4.2.4 Mass fraction-driven fractionation of cellulose nanorods

In the previous fractionation procedures, I attempted to repetitively separate phases using a starting mass fraction in the middle of the phase coexistence regime ($\Phi \approx 0.5$). I now address the CNC fractionation by using starting suspensions with lower and higher macroscopic volume fractions Φ, compared to the previous method. Considering the initial CNC series presented in Figure 4.7, I filled two separatory funnels with CNC suspensions containing different rod mass fractions (and thus, different Φ values). From the init-CNC series, the CNC sample at 4 wt.% shows the first visible formation of LC phase. However, the amount of anisotropic sample is quite small for the separation. Instead, I filled the first separatory funnel with CNC at 4.5 wt.% ($\Phi \approx 0.2$), ensuring a large amount of sample for the preparation of a complete series of mass fractions. Simultaneously, I filled a second funnel with a CNC suspension at 7 wt.% ($\Phi \approx 0.8$). The schematic illustration is presented in Figure 4.9.

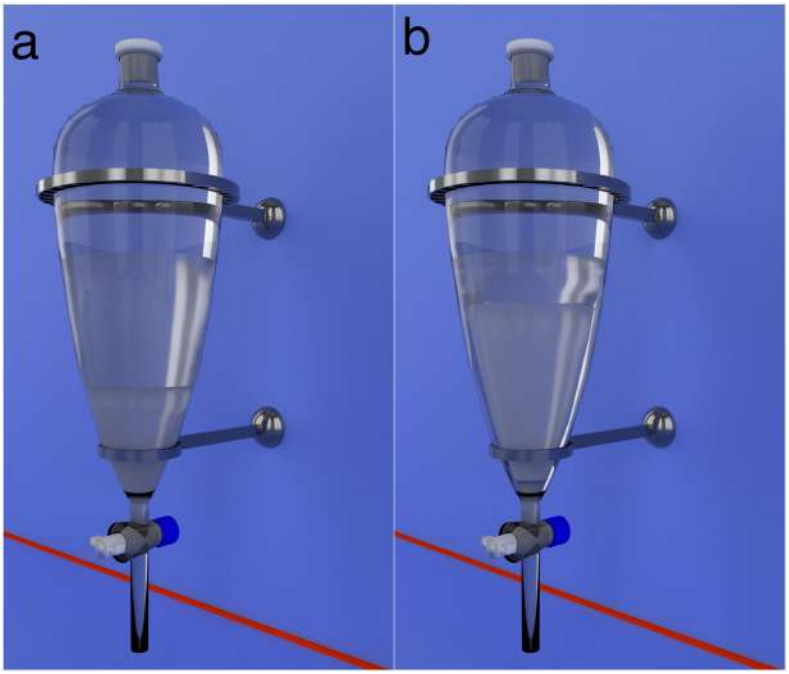

Figure 4.9: Schematic illustration of the mass fraction-driven fractionation procedure using separatory funnels. a) Phase separation in a funnel containing a CNC suspension with overall mass fraction of 4.5 wt.% ($\Phi \approx 0.2$) and b) phase separation in a funnel containing a CNC suspension with overall mass fraction of 7 wt.% ($\Phi \approx 0.8$).

For fractionation, both funnels were left standing for two weeks until the separation of phases was visible. The isotropic parts were then separated from the LC using a pipette and the lower phases were collected by opening the stockcock. In this fractionation procedure, the separation of phases was repeated only once, resulting in four batches: two CNC fractions obtained from the anisotropic phases, corresponding to $a_{0.2}$–CNC and $a_{0.8}$–CNC (from the anisotropic phase of the initial samples with $\Phi \approx 0.2$ at w= 4.5 wt.% and $\Phi \approx 0.8$ at w= 7wt.%, respectively) and

two CNC fractions containing the isotropic phases, corresponding to $i_{0.2}$–CNC and $i_{0.8}$–CNC (from the isotropic part of initial samples at 4.5 wt.% and 7 wt.%, respectively).

Figure 4.10 presents the representative AFM images for two of the fractions and the L/d distribution after measuring 100 rods using the procedure presented in Chapter 2, subsection 2.6.4. From a population of 100 individual rods, the mean $\overline{L/d}$ in $a_{0.2}$–CNC is $\overline{L/d} \approx 78$ with $\sigma_{L/d} \approx 0.4$, whereas in $i_{0.8}$–CNC is $\overline{L/d} \approx 55$ with $\sigma_{L/d} \approx 0.4$. It is known the spontaneous segregation that takes place according to the ratio L/d as the LC phase separates from the isotropic part. However, it is shown in this case that the average L/d in the coexisting isotropic and LC phases strongly depends on the overall mass fraction of the CNC suspension (for disperse CNCs), with high L/d rods dominating the LC phase at lower volume fraction Φ and the low L/d rods populating the isotropic phase at higher Φ.

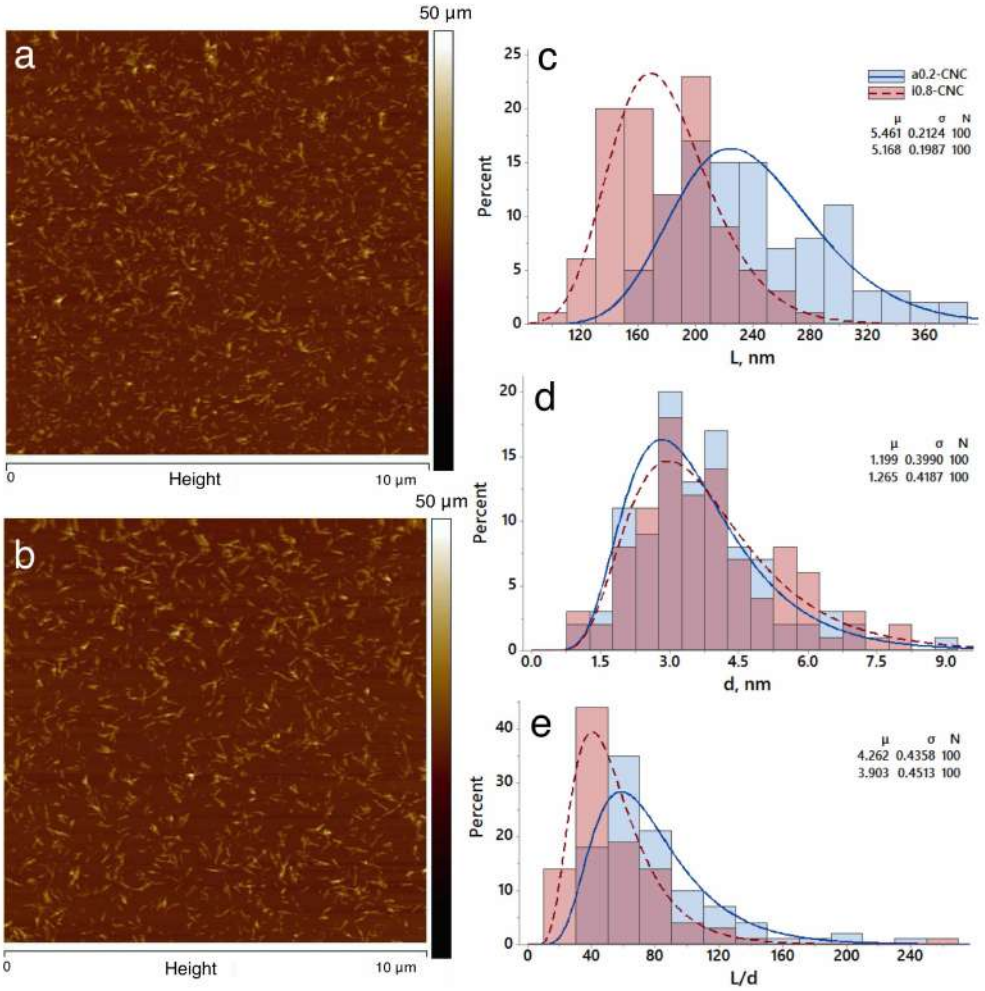

Figure 4.10: Characterization of fractionated CNCs obtained from the mass-fraction driven fractionation procedure. Left: representative AFM images of two of the two final CNC fractions, $4i_f$-CNC (a) and $5af$-CNC (b). Right: Log-normal distribution of the length L (c), diameter d (d), and L/d (e) for the two fractions, as determined from AFM data for 100 rods. Top values in insets: μ and σ of $a_{0.2}$-CNC, corresponding to the mean and standard deviation of the natural logarithm of the variable, respectively. Bottom values in inset: μ and σ of $i_{0.8}$-CNC, corresponding to the mean and standard deviation of the natural logarithm of the variable, respectively. Finally, N indicates the number of individual rods measured from AFM images.

Comparison between fractionation procedures and their effect on the final geometry of the rods

Table 4.1 summarizes the mean values for L and d for the final fractions after their corresponding fractionation procedures as well as values for the length dispersity σ_L. In general, $\bar{L}$ remains relatively unchanged between methods as well as the rod diameter $\bar{d}$.

Table 4.1: Size characterization of fractionated CNCs from AFM analysis.

Fractionation procedure	CNC fraction	$\bar{L}$, μm	σ_L	$\bar{d}$, μm	L/d_1	L/d_2
$\Phi = 0.5$, using pipette	init-CNC	0.2	0.4	0.004	57	50
	$3i_p$-CNC	0.17	0.26	0.004	46	43
	$3a_p$–CNC	0.23	0.44	0.004	61	58
$\Phi = 0.5$, using funnel	init-CNC	200	0.34	0.004	57	50
	$4i_f$-CNC	0.17	0.19	0.004	56	43
	$5a_f$–CNC	0.23	0.13	0.004	74	58
$\Phi = 0.2$ and $\Phi = 0.8$	init-CNC	200	0.34	0.004	57	50
	$i_{0.8}$–CNC	0.19	0.20	0.004	55	48
	$a_{0.2}$–CNC	0.24	0.21	0.004	78	60

Comparing the fractions obtained from the separation of the isotropic phases ($3i_f$-CNC, $4i_f$-CNC and $i_{0.8}$–CNC), rods with higher L/d were obtained from the separation of the isotropic phase from the LC part in a suspension with $\Phi = 0.8$. While a more efficient fractionation might be accomplished for higher Φ, higher mass fractions lead to a gel state, for which $w_g < w_1$ (with w_1 the minimum CNC mass fraction for which $\Phi = 1$ and w_g the CNC mass fraction at the onset of gelation). From Table 4.1, the difference in size is negligible between $3i_f$-CNC and $4i_f$-CNC, it seems that after the third separation of phases the effect of fractionation is reduced to an extent that L/d in the coexisting phases is similar.

For the case of the CNC fractions containing rods with high L/d and prepared from the separation of the LC phases from the isotropic parts ($3a_p$–CNC, $5a_f$–CNC and $a_{0.2}$–CNC), $\bar{L}$ presents relatively the same values in all the suspensions ($\bar{L} \approx 0.23$ μm). However, the length dispersity is reduced from $\sigma_L^{3ap} \approx 0.44$ to $\sigma_L^{5af} \approx 0.13$. This difference in length dispersity shows that the higher value of σ_L in the length distribution of particles obtained from the separation of phases using a pipette was due to the less precise extraction of one phase from the other in comparison to the extraction with a separatory funnel.

Values of L/d are included in Table 4.1 calculated using two different procedures (L/d_1 and L/d_2). As I explained in Chapter 3, the diameter of the rods is not constant along the particle, resulting in small values of d with large variations in individual rods. For the case L/d_2, the diameter d was considered to be constant, with $d = 4$ nm. Then I determined L/d_2 as $\bar{L}$ (from Table 4.1) over the constant d. If we considered this analysis, rods obtained from the LC part

of $a_{0.2}$–CNC shows the highest $L/d \approx 60$, without significant variation between $3i_p$-CNC and $4i_f$-CNC, with $L/d \approx 43$.

I attempted to determine the amount of CNC that is needed for obtaining CNC suspensions containing rods with high L/d after both the repetitive separation of phases starting at $\Phi \approx 0.5$ and the mass fraction-driven procedure at $\Phi \approx 0.2$. Table 4.2 presents the amount of separation steps needed for fractionation starting from an init-CNC until reaching five separation of phases ($5a_f$-CNC). In addition, Table 4.2 presents the CNC mass fraction w for which $\Phi \approx 0.5$. For the calculations, I assume that the coexisting phases have the same w as the overall sample (although w_{LC} in the LC phase is always higher than the overall w and w_i is lower in the isotropic phase compared to the overall w [2]). CNC series of a-CNC and 2a-CNC corresponds to the first and second separation of the LC phases, respectively.

Table 4.2: Determination of amount of material needed for separation of phases.

sample	number of separations	w for which $\Phi \approx 0.5$, wt.%
init-CNC	0	6
a_f–CNC	1	5
$2a_f$–CNC	2	4
$3a_f$–CNC	3	3.5
$4a_f$–CNC	4	3.3
$5a_f$-CNC	5	3.2

We can calculate the mass of CNC (without including the water) of the LC phase after phase separation ($\Phi = 0.5$) m_{CNC} as:

$$m_{CNC} = \Phi w_{0.5} V_{CNC} \tag{4.1}$$

with $\Phi = 0.5$, $w_{0.5}$ the mass fraction for which $\Phi \approx 0.5$ from Table 4.2 and V_{CNC} the volume of CNC sample after the separation. We consider the density ρ of the CNC suspensions as 1 g/mL.

Water is added to the resulted LC phase until a new volume V_{CNC} in order to dilute the CNC suspension to $w_{0.5}$, for which $\Phi = 0.5$:

$$V_{CNC} = \frac{m_{CNC}}{w_{0.5}} \tag{4.2}$$

After phase separation of the CNC sample with volume V_{CNC} ($\Phi = 0.5$), we calculate the amount of CNC with Eq. 4.1.

Using Eq. 4.1 and Eq. 4.2, I can estimate that in order to obtain 1 g of CNC (without including the water) after three separation cycles ($3a_f$–CNC), we would need an initial CNC suspension

with $\Phi = 0.5$ of $V_{CNC}^{init} \approx 133$ mL (133 g considering $\rho = 1$ g/mL)

If I determine now the amount of CNC suspension for fractionation using $\Phi = 0.2$ ($w = 4.5$ wt.%), by using Eq. 4.1 we obtain $V_{CNC}^{init} \approx 110$ mL (110 g considering $\rho = 1$ g/mL).

For further fractionation starting with $\Phi = 0.5$ ($4a_f$–CNC and $5a_f$-CNC) an even larger initial volume of CNC will be required.

The main difference between procedures lies in the time that is needed for fractionation. The mass fraction-driven fractionation is the best option for fractionation, since the separation of phases is carried out only once. In addition, less initial sample is needed compared to the amount of the CNC that is used in the method of repetitive separation of phases, starting in the middle of the coexistence regime.

4.3 Equilibrium phase diagram of the CNC suspensions

Series of relevant mass fractions w of the initial CNCs were prepared as well as of the samples obtained after the three fractionation procedures. Prior to the analysis, the sample vials stood vertically for minimum 3 months, resulting in separation into a lower LC phase and an upper isotropic phase. The volume fraction of every LC phase (Φ) was determined by measuring the ratio of the height of the LC phase to that of the full sample (LC and isotropic). The macroscopic phase separation and the phase diagrams in pure water of each sample are presented in Figures 4.11 – 4.13.

The maximum mass fraction w_0 for $\Phi = 0$ and the minimum mass fraction w_1 for $\Phi = 1$ are both affected by L/d. From the quantitative plots of the relative volume fraction (Figures 4.11b – 4.13b), Φ increases monotonically from 0 to 1 with increasing w with the exception of CNCs containing rods from the isotropic phases (low L/d rods: $3i$–, $4i$–, $i_{0.2}$– and $i_{0.8}$–CNCs) as well as the rods of the init-CNCs, for which $w_1 > w_g$ (w_g corresponds to the CNC mass fraction at which the suspension turns into a gelled state). When $w = w_g$, a departure from the monotonic behavior is seen with a sudden rise in the apparent LC volume fraction to $\Phi^{app} = 1$. This is not the true LC volume fraction but rather an artifact due to the inability of the LC phase to separate from the isotropic phase in the gelled macroscopic sample. For these samples, w_1 must be extrapolated from data.

Table 4.3 summarizes the values of w_0 and and w_1 that were determined from the plots in Figures 4.11b – 4.13b for the three fractionation procedures and the initial CNCs.

In the case of the samples obtained after the fractionation using a pipette, the increased L/d

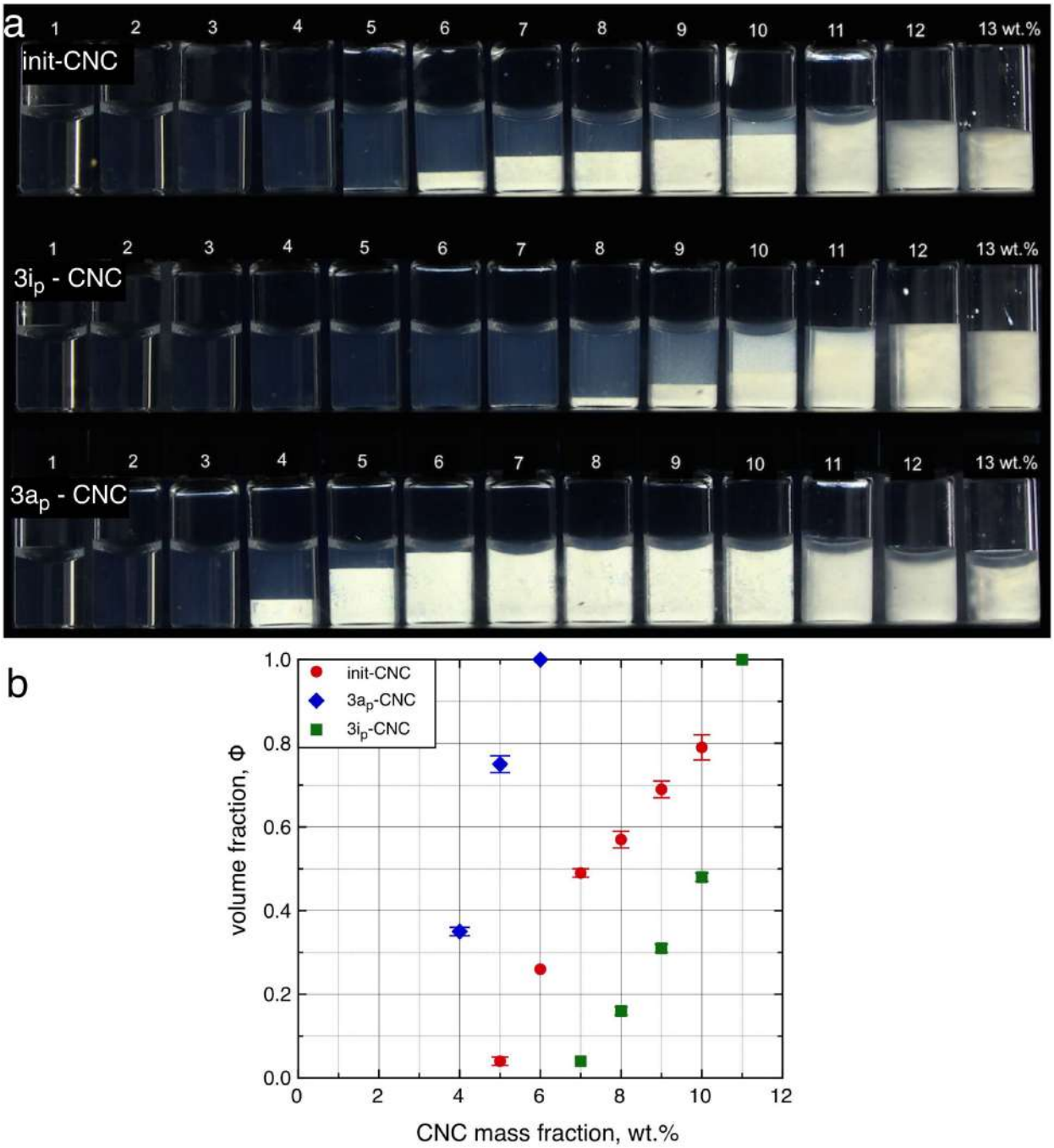

Figure 4.11: Effect of fractionation on the phase sequence. a) Phase separation in suspensions of cellulose nanocrystals between crossed polarizers for the initial series (init-CNC), and the high L/d fraction ($3a_p$–CNC) and low L/d samples ($3i_p$-CNC) as a function of the CNC mass fraction w in pure water. b) Quantitative plots of the volume fraction Φ of the LC phase for the three series. The error bars correspond to five different measurements per sample vial. The sample vials stood for 4 months before the photos were taken and the quantitative measurements made. From Honorato–Rios *et al.* [2].

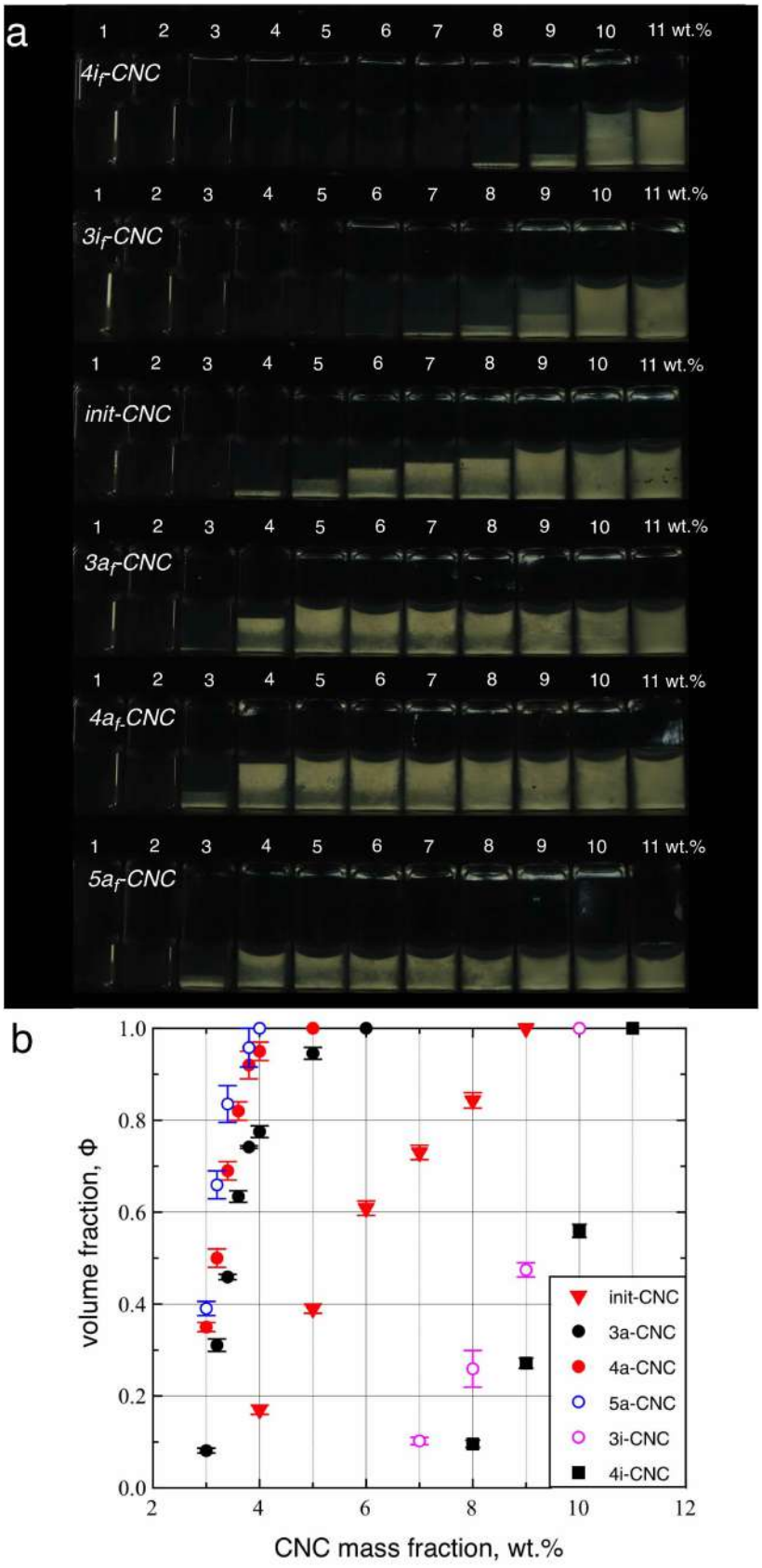

Figure 4.12: Effect of fractionation using a separatory funnel on the phase sequence, from an init-CNC with $\Phi \approx 0.5$. a) Phase separation in suspensions of cellulose nanocrystals between crossed polarizers for $4i_f$-CNC, $3i_f$-CNC, init-CNC, $3a_f$-CNC, $4a_f$-CNC and $5a_f$-CNC as a function of the CNC mass fraction w in pure water. b) Quantitative plots of the volume fraction ϕ of the LC phase for the different series. The error bars correspond to five different measurements per sample vial. The sample vials stood for 4 months before the photos were taken and the quantitative measurements made.

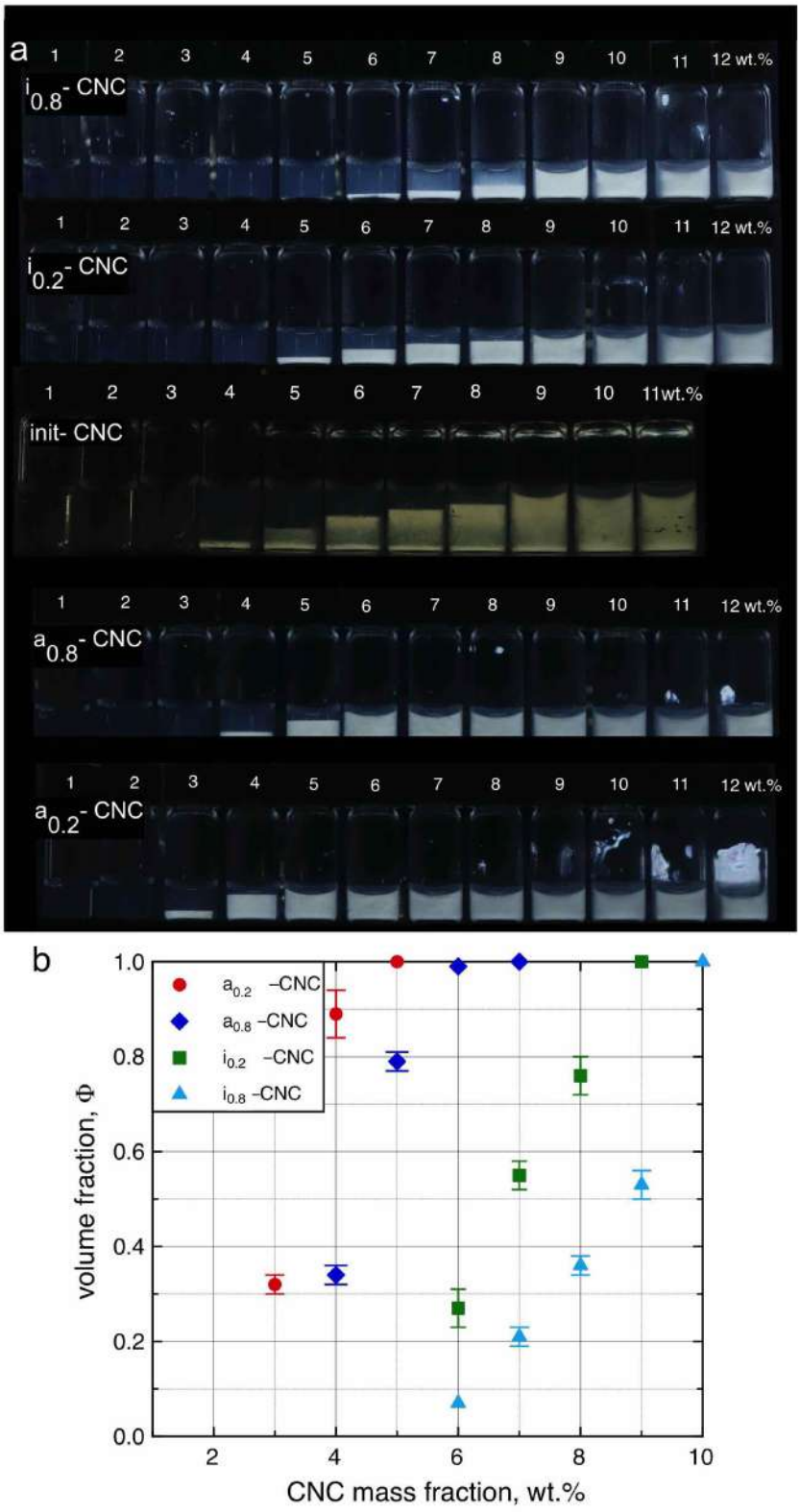

Figure 4.13: Effect of fractionation using the mass-fraction separation procedure, on the phase sequence. a) Phase separation in suspensions of cellulose nanocrystals between crossed polarizers for $i_{0.8}$-CNC, $i_{0.2}$-CNC, init-CNC, $a_{0.8}$-CNC and $a_{0.2}$-CNC, as a function of the CNC mass fraction w in pure water. b) Quantitative plots of the volume fraction ϕ of the LC phase for the different series. The error bars correspond to five different measurements per sample vial. The sample vials stood for 1 month before the photos were taken and the quantitative measurements made.

Table 4.3: Effect of fractionation method on the onset of liquid crystal formation, w_0, and on the onset of the fully LC phase, w_1.

Method	sample code	$w_0, wt.\%$	$w_1, wt.\%$
from $\Phi \approx 0.5$ with pipette	init-CNC	5	11.8
	$3a_p - CNC$	3	6
	$3i_p$-CNC	7	13
from $\Phi \approx 0.5$ with funnel	init-CNC	4	11.5
	$3a_f$–CNC	2.8	5.5
	$4a_f - CNC$	2.8	4.2
	$5a_f - CNC$	2.8	4
	$3i_f$-CNC	7	13
	$4i_f$-CNC	8	14
mass fraction-driven from $\Phi \approx 0.2$ and $\Phi \approx 0.8$	init-CNC	4	11.5
	$a_{0.2}$–CNC	2.8	4.2
	$a_{0.8}$–CNC	3	6
	$i_{0.2}$–CNC	4.5	9.5
	$i_{0.8}$–CNC	6	12

in the $3a_p$-CNC sample causes a decrease in w_0 from $w_0^{init} \approx 5$ wt.% in the initial sample to $w_0^{3a_p} \approx 3$ wt.%. For $w_0^{3i_p}$, the decrease in L/d instead increased the limit of stability of the isotropic phase to $w_0^{3i} \approx 7$ wt.%. Also, w_1 is affected, shifting from $w_1^{init} \approx 11.8$ wt.% in the unfractionated sample to $w_1^{3a_p} \approx 6$ wt.% in $3a_p$-CNC. In the case of $3i_p$-CNC, w_1 increases compared to that of init-CNC to a value greater than w_g, triggering gelation. Therefore, it is impossible to give a direct value of w_1^{3i} for the suspension of short rods. By extrapolation of the data in Figure 4.11b, it is possible to estimate that $w_1^{3i} \approx 13$ wt.%.

Figure 4.12 presents three series of CNC mass fractions with rods obtained after repetitive separation of the LC phase ($3a_f$-CNC, $4a_f$-CNC and $5a_f$-CNC) and two series of CNCs containing rods from the isotropic phases ($3i_f$-CNC and $4i_f$-CNC), starting at $\Phi \approx 0.5$ and separated with a separatory funnel. For the case of the fractions with high L/d, the effect of fractionation has decreased to an extent that the onset of liquid crystalline formation w_0 remains relatively constant for fourfold and fivefold separation cycles, decreasing from $w_0^{init} \approx 4$ wt.% in the init-CNC to $w_0 \approx 2.8$ wt.% for both $4a_f$-CNC and $5a_f$-CNC samples. Besides, w_1 is shifted from $w_1^{init} \approx 10.5$ wt.% to $w_1^{4a_f} \approx 4$ wt.% as well as $w_1^{5a_f} \approx 4.2$ wt.%, with a very small variation between the two samples. Early theoretical studies in the field of non-uniform rod-like polymers already predicted this behavior. Flory and Frost [62] and Moscicki with Williams a few years later [63], predicted that fractionation takes place in the biphasic region between ϕ_0 and ϕ_1. They reported that the dispersity in each phase is significantly lower compared to the parent (or init-CNC in our case) distribution, highlighting the efficiency of fractionation by separation of the phases of a parent sample. Lekkerkerker et *al.* [64] also reported the spontaneous

fractionation in the LC formation by extending Onsager's model.

My results suggest that for highly disperse samples, a strong fractionation occurs between the isotropic and LC phases, such that the LC part is completely dominated by the longest rods and the isotropic phase by the shortest particles in the distribution. On the contrary, when the dispersity is reduced, only moderate fractionation is carried out, resulting in coexisting phases with similar L/d distributions. Most notably, we observe that the isotropic and nematic limits shift to lower mass fractions, significantly narrowing the two-phase regime. The lowest length dispersity was found for the $5a_f$-CNC sample with $\sigma_L^{5a} \approx 0.13$ (Table 4.1). The mass fraction range for which the biphasic region takes place is 2.8 wt.% $< w <$ 4 wt.%, the narrowest range between all the values presented in Table 4.3.

To the best of my knowledge, the only study concerning dispersity in rod-like systems is reported for solutions of imogolite (a rigid rod polymer). The authors observed that the two-phase regime was narrowed with decreasing dispersity of the particles [65]. A number of theoretical studies have emphasized the importance of dispersity in the phase behavior in systems with rigid rods. Particularly they predict the phase boundaries based on hard rod interaction of a highly dispersed system [66–68]. Later on, this model was extended to include an attractive term [69] for single-walled carbon nanotubes (SWNT) dissolved in superacids. The same theoretical studies have indicated scenarios for which a high dispersity might lead to three-phase equilibrium regime (isotropic-nematic-nematic). Experimentally, three coexisting phases have been observed in highly disperse clay [70] and boehmite rods [71]. Even in CNC suspensions, a CNC sample developed three phases [72] after 6 months of equilibrium, although no further discussion is presented by the authors.

For the case of the low L/d rods from Figure 4.12, w_0 also varies, increasing to $w_0^{3i} \approx 7$ wt.% and $w_0^{4i} \approx 8$ wt.% in $3i_f$- and $4i_f$-CNCs, respectively. In both samples, w_1 has reached values greater than w_g, provoking gelation. Because of this, it is not possible to give empirical values of w_1 for suspensions of low L/d rods. By extrapolation, $w_1^{3i} \approx 13$ wt.% and $w_1^{4i} \approx 14$ wt.% in 3i- and $4i_f$-CNCs, respectively. A continuation of the fractionation beyond four cycles for the isotropic phase becomes difficult due to the slow separation of the phases at high w. For the case of $w^{4i} = 10$ wt.% ($\Phi \approx 0.5$), the bottom and top phases are similar even after several months for the sample vial to equilibrate. The scattering in the top part suggest that the separation is not yet complete, so the extraction of the top part will end up in inefficient fractionation by L/d.

Finally, the separation of two biphasic suspensions into the isotropic and LC parts, with $\Phi \approx 0.2$ and $\Phi \approx 0.8$ respectively, yielded four fractionated samples containing rods with different L/d. Figure 4.13 presents the macroscopic phase separations and phase diagrams of the four

CNC series after fractionation, as well as the init-CNC. The results exhibit that the mass fraction-driven procedure is a very effective method for fractionation, with w_0 decreasing from $w_0^{init} \approx 4$ wt.% to $w_0^{a_{0.2}} \approx 2.8$ wt.%, similar to $w_0^{5a_f}$ after fivefold separation cycles starting with $\Phi \approx 0.5$. Also, w_1 shifts to a value similar to $w_1^{5a_f}$, changing from $w_1^{init} \approx 11.5$ wt.% to $w_1^{a_{0.2}} \approx 4.2$ wt.%. For the case of the rods with low L/d, the fractionation is less effective compared to the procedure of multiple separation cycles. In this case, the decrease in L/d causes an increase in w_0 from $w_0^{init} \approx 4$ wt.% to $w_0^{i_{0.2}} \approx 4.5$ wt.% and $w_0^{i_{0.8}} \approx 6$ wt.% for $i_{0.2}-$ and $i_{0.8} - CNC$ samples, respectively.

When fractionating a CNC suspension by choosing a low volume fraction Φ, the tactoids that first form have the higher ϕ=ϕ_1, which corresponds to the stability limit of the nematic phase. In addition, ϕ_0 is shifted to a lower value with increasing L/d. This results in a separation of a subvolume for which the L/d is the highest for a value of Φ that is slightly higher than $\Phi = 0$. When a value of Φ is chosen slightly lower than $\Phi = 1$, rods with the lowest L/d will populate the isotropic phase, since the tactoids formed with longer rods have merged and sunk to the bottom liquid crystal phase.

The separation of the phases in biphasic suspensions for samples at high w takes longer time compared to CNC suspensions with lower w. Apparently, the mass fraction-driven fractionation for the low L/d fractions needs more time for a complete phase separation. This can explain the weaker fractionation effect in our results. I elaborate this topic in the following subchapter.

4.3.1 Time frame of phase separation

The difference in mass fraction at which the two coexisting phases occurs between the samples containing high and low L/d rods has also an impact on the time needed for a complete phase separation. To evaluate this, I followed the macroscopic phase separation over time of two CNC series with different L/d ($3a_f$-CNC, with a two-phase regime between 2.8 wt.% and 5.5 wt.%, and $3i_f$-CNC presenting a two-phase regime between 7 wt.% and 13 wt.%) by capturing consecutive photographs of the sample vials standing between crossed polarizers. Figure 4.14 shows sequences of images after certain time for both series, where a visible phase separation starts after time $t \approx 4$ h for the $3a_f$-CNC and a complete separation is reached after $t \approx 15$ h. In contrast, for the $3i_f$-CNC series, the first sign of macroscopic phase separation is visible after $t \approx 48$ h and a complete separation is not reached even after 3 months.

Normally, the greater density of the LC phase in a tactoid compared to that of the isotropic surrounding leads to sedimentation until the tactoid merges with the macroscopic LC phase at the bottom, as seen for all the high L/d samples.

While the upper phase in the two-phase regime is transparent and black between crossed polarizers for all the high L/d fractions ($3a_f$-CNC, $4a_f$-CNC and $5a_f$-CNC), as expected for an isotropic phase, this is not the case for the low L/d samples ($3i_f$-CNC and $4i_f$-CNC). For both samples the upper phase scatters light in the macroscopic vials, increasing with the CNC volume fraction. In capillaries investigated by POM, we see that the upper phase is not black but decorated with birefringent tactoids (Figure 4.15).

The presence of these tactoids continuously increases with increasing w, especially from 8 – 11 wt.% for the $3i_f$-CNC and 10 – 11 wt.% for the $3i_f$-CNC sample. Importantly, the capillaries shown in Figure 4.15 have been standing vertically for 3 months, hence there has been plenty of time to reach equilibrium. Instead, we must consider the kinetic effect of the substantially greater CNC content of the biphasic $3i_f$- and $4i_f$-CNC samples. As in any isotropic colloidal suspension, the viscosity of the upper phase increases with increasing the particle content w.

Especially when we approach gelation ($w_g \approx 12$ wt.%) the viscosity may be so high that the relatively low density difference between liquid crystalline tactoids and the isotropic surrounding is insufficient to drive visible sedimentation even over 2 months. In fact, even after 18 months for previous samples with short rods (not shown here), the tactoids have remained in the isotropic phase. For the $3a_f$-CNC, $4a_f$-CNC and $5a_f$-CNC, the biphasic regime ends already at around $w_1 \approx 4$wt.%, still far from gelation, hence the viscosity of the isotropic phase that surrounds the tactoid is low enough for a complete sedimentation.

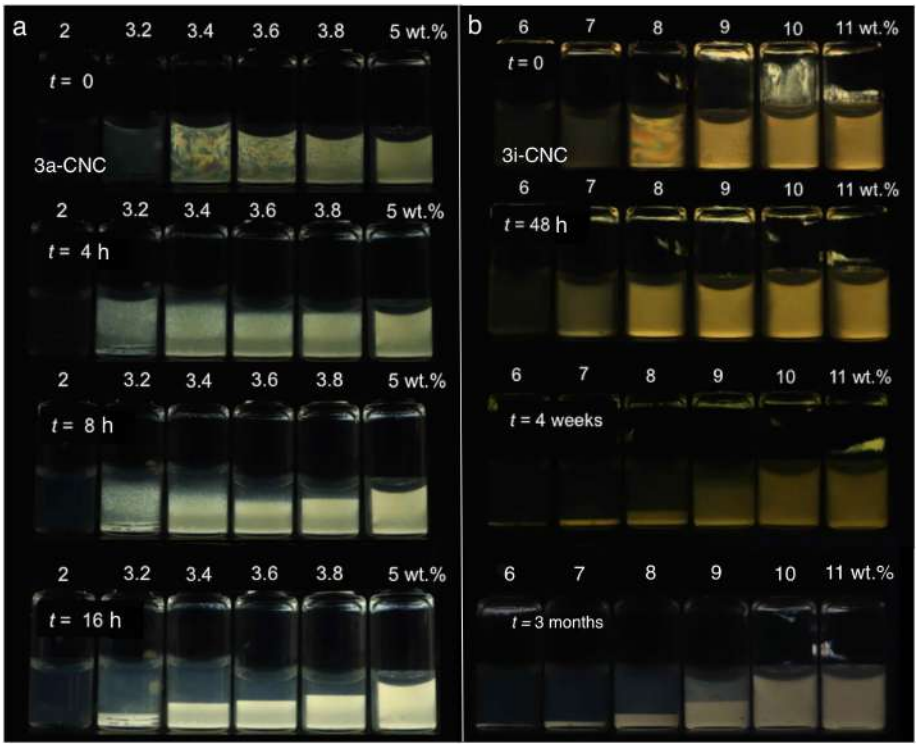

Figure 4.14: Phase separation of fractionated samples after different time t. a) $3a_f$-CNC suspensions and b) $3i_f$-CNC suspensions.

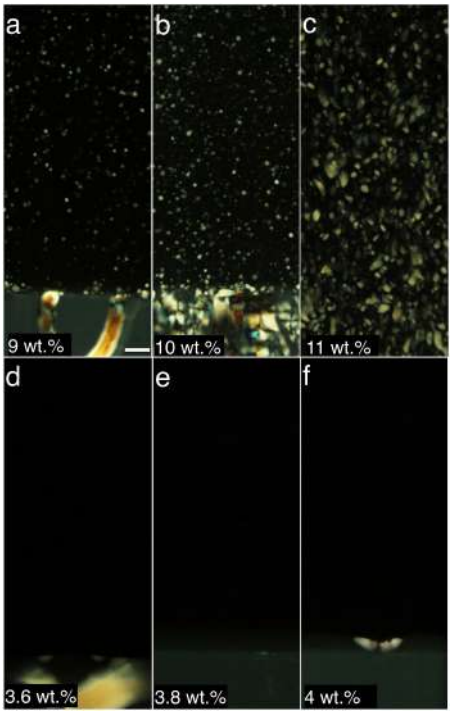

Figure 4.15: Polarized optical microscopy (POM) images of glass capillaries filled with fractionated CNC samples. (a-c) $3i_f$-CNC (d-f) $3a_f$-CNC. The capillaries have been standing in vertical position for 18 months. Scale bars correspond to 200 μm.

4.4 Summary

Fractionation of disperse CNC suspensions is remarkably efficient by the separation of phases into an isotropic and liquid crystal part, thanks to the spontaneous fractionation that occurs between the two phases. This process can be accelerated depending on the volume fraction Φ in the initial CNC that is chosen. Rods with the highest aspect ratio are obtained from the liquid crystal phase if Φ in the initial suspension is slightly higher than $\Phi = 0$. On the contrary, rods with the lowest L/d populate the isotropic phase of an initial CNC with Φ slightly lower than $\Phi = 1$. This fractionation process is very convenient considering that the separation of phases is carried out only once, since it avoids the tedious waiting process that is needed, especially for the low aspect ratio rod fractions, for which evaporation of water is needed.

Chapter 5

Kinetic arrest in cellulose nanocrystal suspensions

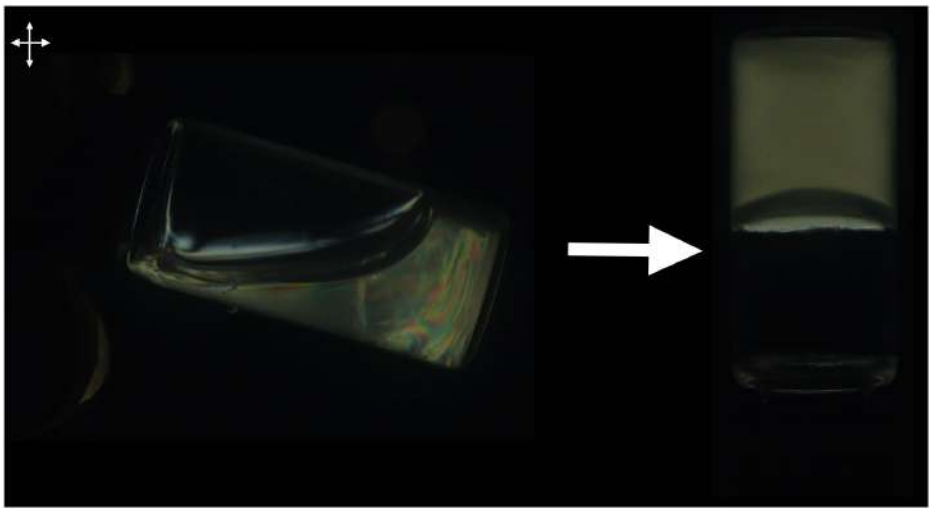

Overview of this chapter[1]

The same factor that permits CNC to form liquid crystal phases after certain mass fraction—the high aspect ratio—also promotes kinetic arrest into a non-equilibrium state, which results in a competition between the two processes. By adding salt to CNC samples within a concentration range, it is shown that kinetic arrest is triggered by the loss of colloidal stability, regardless of the rod aspect ratio. Furthermore, atomic force microscopy (AFM) reveals linear rod aggregation of CNCs upon salt addition.

[1]This chapter is partially reproduced from Honorato-Rios, C. *et al.*. Fractionation of cellulose nanocrystals: enhancing ordering without promoting gelation. NPG Asia Materials, pages 1-11, 2018.

5.1 Introduction

Colloids with rod-like particles can develop liquid crystalline phases upon the increasing mass fraction. Nevertheless, such increments in the amount of particles can also result in close rod encounters, with rods blocking each other's movements. Especially in systems containing rods with high aspect ratio, this kinetic arrest phenomenon—referred to as rigidity percolation if the scale of restricted motion equals the sample size—can turn the phase into a non-equilibrium state, recognized through a gel-like appearance [4, 38, 43, 51, 73–76].

From a liquid crystal point of view, gelation can truly be a disadvantage, as it considerably limits the range in which the two phases coexists. Even more, sometimes gelation sets in before the system has formed a complete liquid crystal phase. However, a valuable feature from an application perspective is that this non-equilibrium state allows to maintain any order (or disorder) that has been reached in an earlier stage. For the case of CNCs, it is due to this kinetic arrest that iridescent films can retain the cholesteric structures after the evaporation of the solvent.

Several studies have shown that kinetic arrest can be promoted in CNC suspensions by different factors, such as the temperature [77], CNC in non-water solvents [51], low charge density [38], additives [78] or just by an increase in CNC mass fraction [79]. Qualitatively, all the reported factors reduce the stability of the CNC suspensions, favoring the onset of gelation [80].

From the previous chapter, by exploiting the spontaneous segregation according to aspect ratio L/d that takes place as the LC phase separates from the isotropic part, it has been shown that the long-rod fraction strongly favours liquid crystallinity by reducing the threshold w_0 for liquid crystal formation, without exploring the influence of L/d on w for which kinetic arrest sets in. In this chapter, I extend the study by identifying the onset of kinetic arrest in CNC fractions obtained from one of the fractionation procedures presented in Chapter 4. Furthermore, I induce kinetic arrest by the addition of salt to CNCs containing rods with low and high L/d, which resulted in gel-like samples with end-to-end rod aggregation due to the loss of colloidal stability in the suspensions.

5.2 Effect of L/d on the onset of gelation

I establish the onset of gelation for three series of samples that contain rods with different aspect ratio L/d. The method for the separation has been described in Chapter 4, and a pipette was used for the extraction of the isotropic phase (upper part) from the LC phase (bottom part). The sample vials after phase separation and between cross polarizers are presented in Figure 5.1.

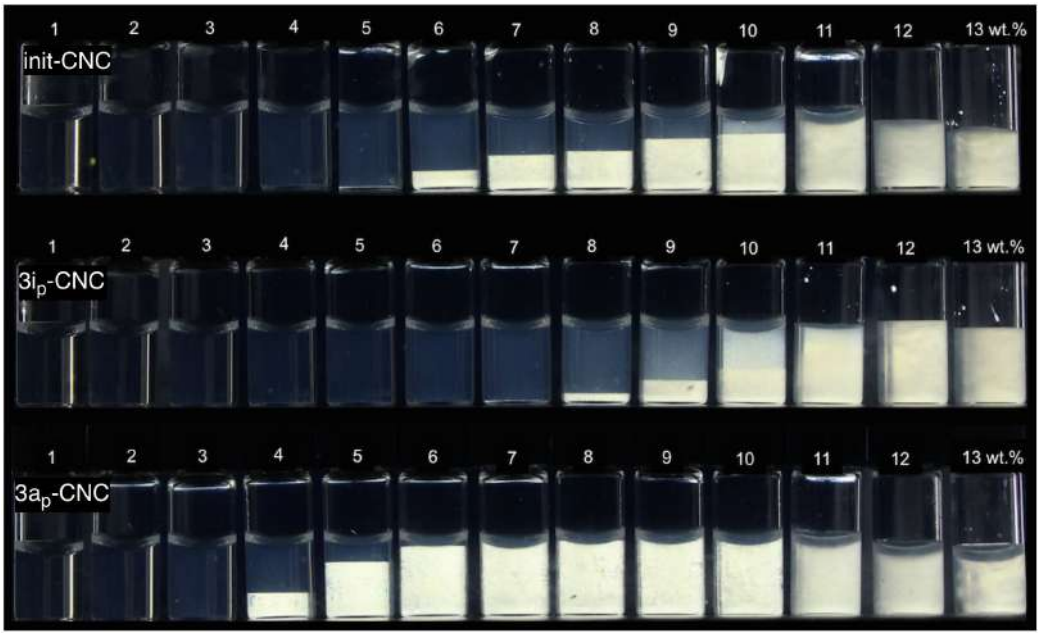

Figure 5.1: Phase separation of sample vials after fractionation using a pipette as well as the init-CNC. This image corresponds to Figure 4.11a from Chapter 4. From Honorato–Rios *et al.* [2].

From Figure 4.5 in Chapter 4, the length mean was $\bar{L} \approx 0.20$ μm with a dispersity $\sigma_L \approx 0.4$ for the init-CNC, $\bar{L} \approx 0.23$ μm with $\sigma_L \approx 0.4$ for $3a_p$–CNC and $\bar{L} \approx 0.17$ μm with $\sigma_L \approx 0.3$ for the $3i_p$–CNC suspension. The diameter mean $\bar{d} \approx 4$ nm for each of the three CNC samples.

The onset of gelation was defined as the mass fraction at which the sample remained at the top of the vial after carefully turning the sample upside down, as shown in Fig. 5.2. If the suspension remained on the top (at the normal bottom of the sample vial), the suspension is considered to be in a gel state. A very interesting observation is that all CNC suspensions reach gelation at about the same CNC content of $w_g \approx 12$ wt.% regardless of the L/d of the rods, at least within the range probed in this experiment. This shows that the change in L/d has no impact on the onset of gelation, while the common picture based on percolation of the individual rods would suggest that both, LC formation and gelation, should happen at a lower w for $3a_p$-CNC and at a higher value of w for the case of $3i_p$-CNC.

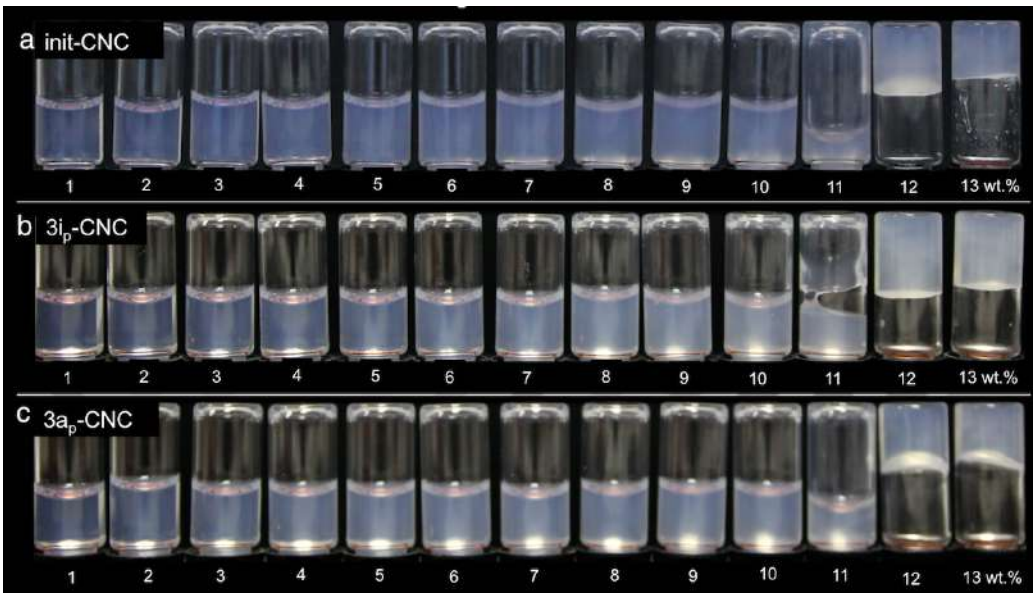

Figure 5.2: Sample vials of salt-free samples after 24 hours upside down. Top: init-CNC, middle: $3i_p$–CNC and bottom: $3a_p$–CNC. For all the CNC suspensions, the onset of gelation is $w \approx 12$ wt.%. From Honorato–Rios *et al.* [2].

Gelation makes difficult to investigate CNC mass fractions beyond ≈ 12 wt.%. My initial hypothesis behind these fractionation experiments was to suppress this non-aquilibrium state by working with low L/d rods. As I discussed before and according to percolation theory, the suspension with short rods should shift w_g to a higher mass fraction compared to the unfractionated suspension. Perhaps this delay in gelation would lead to a transition into high-ordered liquid crystal phases, as is the case for a family of viruses related to filamentous phage *fd* [81–87] as well as for DNA [88]. Unfortunately, this was not the case and gelation set in at the same mass fraction regardless of L/d.

5.3 Effect of counterion concentration on the onset of gelation

Based on our observations above, I conjecture that gelation is triggered solely by reaching a threshold value of a counterion concentration $c^g_{Na^+}$ since the only source of ions in these samples is the CNCs themselves. To corroborate our conjecture, I attempted to induce gelation at a substantially reduced CNC mass fraction by adding salt (NaCl) until $c_{Na^+} = c^g_{Na^+}$. A similar approach has previously been used for inducing gelation, e.g., in fully isotropic suspensions of nanofibrilalted cellulose with carboxyl groups at the fibril surface [89] and of dye-doped CNCs [90].

To determine experimentally the threshold value of counterion concentration that triggers gela-

tion $c^g_{Na^+}$, I attempted to induce gelation also at $w < 12$ wt.% by adjusting the sodium ion concentration in all suspensions until $c_{Na^+} = c^g_{Na^+}$ via addition of NaCl solution (1 M). In order to have a starting point of how much NaCl solution to add to each vial, the sulfur content calculated in Chapter 3 was used, assuming that every sulfate group is in its ionic state. This assumption is based on the fact that the CNC was, after the sulfuric acid hydrolysis, completely neutralized with an excess of NaOH. As it is common for commercial samples, the CNC counterions are thus Na^+. A CNC mass fraction of $w_g = 13$ wt.% was the initial estimation of the amount of CNC needed for ensuring gelation. This allowed to estimate the expected counterion concentration required for gelation as:

$$c^g_{Na^+} = c^g_S = w_S \frac{\rho w_g}{M_S} \tag{5.1}$$

where c^g_S is the sulfur concentration in the sample at the onset of gelation without salt addition, w_S the sulfur mass fraction determined by conductometric titration, ρ the density of the CNC suspension, w_g the CNC mass fraction at the onset of gelation and M_S is the molar mass of sulfur. For simplicity, the density ρ of the suspension was approximated to 1 kg/L, thus yielding a sample mass of $m = 1$ kg per liter of suspension. From Eq. 5.1, $c^g_{Na^+} = 45$ mM.

Starting from this result, I calculated the required NaCl concentration c_{NaCl} for achieving constant $c_{Na^+} = c^g_{Na^+}$ for every CNC mas fraction w, corresponding to a sulfur concentration c_S, as:

$$c^g_{Na^+} = c_S + c_{NaCl} = c^g_{Na^+} \frac{w}{w_g} + c_{NaCl} \tag{5.2}$$

with $c^g_{Na^+} = 45$ mM. The different experiments with salt addition prepared according to this formula, for each of the CNC qualities with w increasing in integer steps from 1 wt.% to 11 wt.%, yielded the behavior after 24 h are shown in Figures 5.3 – 5.5. The amount of NaCl calculated ($c^g_{Na^+} = 45$ mM) appeared to be sufficient, suggesting that the estimated concentration is very close to the experimental value. One must point out that gelation may be a slow process in the vicinity of $c_{Na^+} = c^g_{Na^+}$ [90], hence it may be that the 24 h waiting time in our experiments is insufficient, and the real $c^g_{Na^+}$ is in fact somewhat lower than 45 mM.

Figure 5.6 shows vials with varying contents of init-CNC, $3i_p$–CNC and $3a_p$–CNC, photographed between crossed polarizers 3 weeks after adding an amount of NaCl that is required to reach $c_{Na^+} = c^g_{Na^+}$ in every vial. Twenty four hours after the salt addition, the vials were turned upside down and then left standing untouched. The experiment confirms the prediction that gelation is induced in all samples with $w > 2$ wt.%, irrespective of the series. An important further

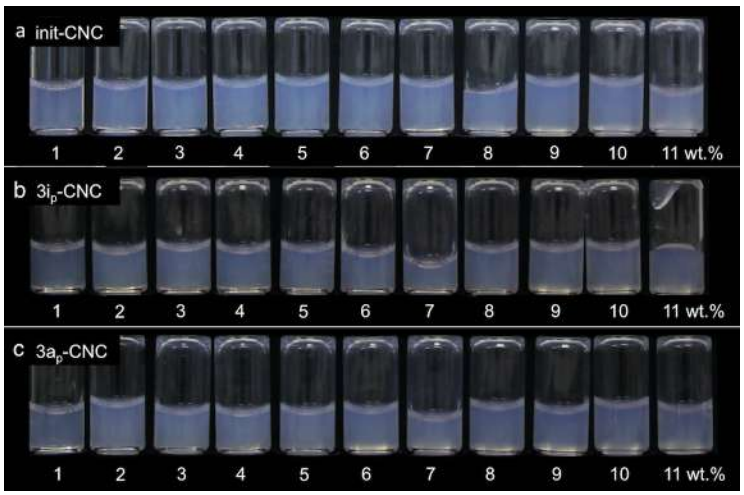

Figure 5.3: Sample vials with $w < 11$ wt.% standing upside down during 24 h after addition of salt assuming a gelation threshold counterion concentration of $c^g_{N_a{}^+} = 39$ mM. (a) init-CNC (b) 3*i*–CNC and (c) 3*a*–CNC. From Honorato–Rios *et al.* [2].

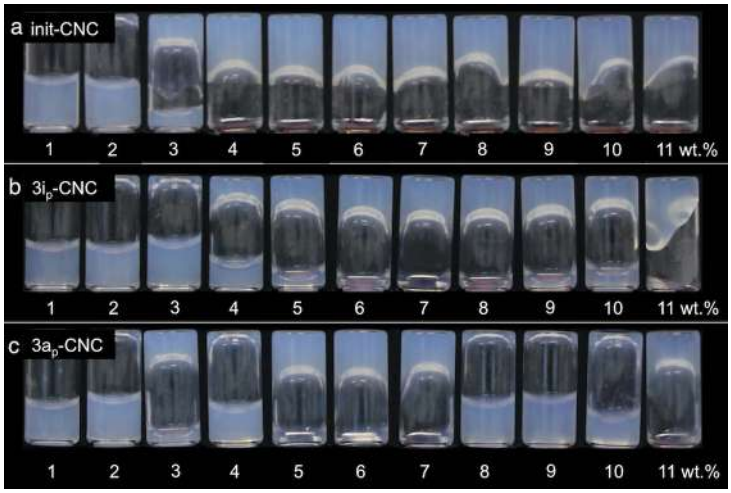

Figure 5.4: Sample vials with $w < 11$ wt.% standing upside down during 24 h after addition of salt assuming a gelation threshold counterion concentration of $c^g_{N_a{}^+} = 43$ mM. (a) init-CNC (b) 3i_p–CNC and (c) 3a_p–CNC. From Honorato–Rios *et al.* [2].

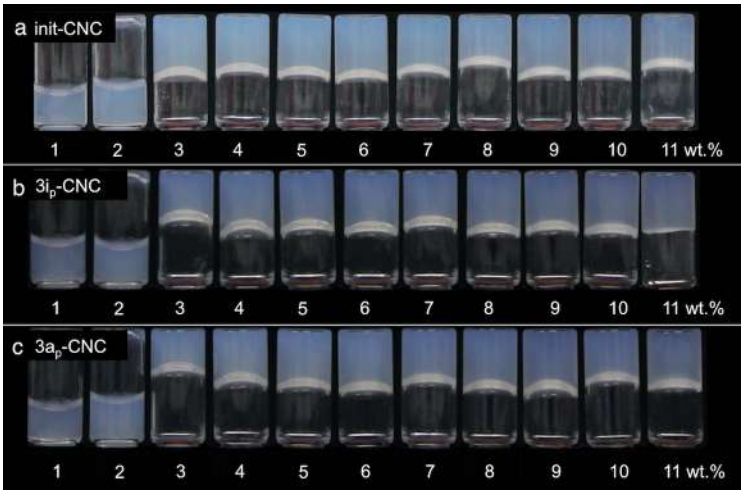

Figure 5.5: Sample vials with $w < 11$ wt.% standing upside down during 24 h after addition of salt assuming a gelation threshold counterion concentration of $c^g_{N_a{}^+} = 45$ mM. (a) init-CNC (b) 3i_p–CNC and (c) 3a_p–CNC. From Honorato–Rios *et al.* [2].

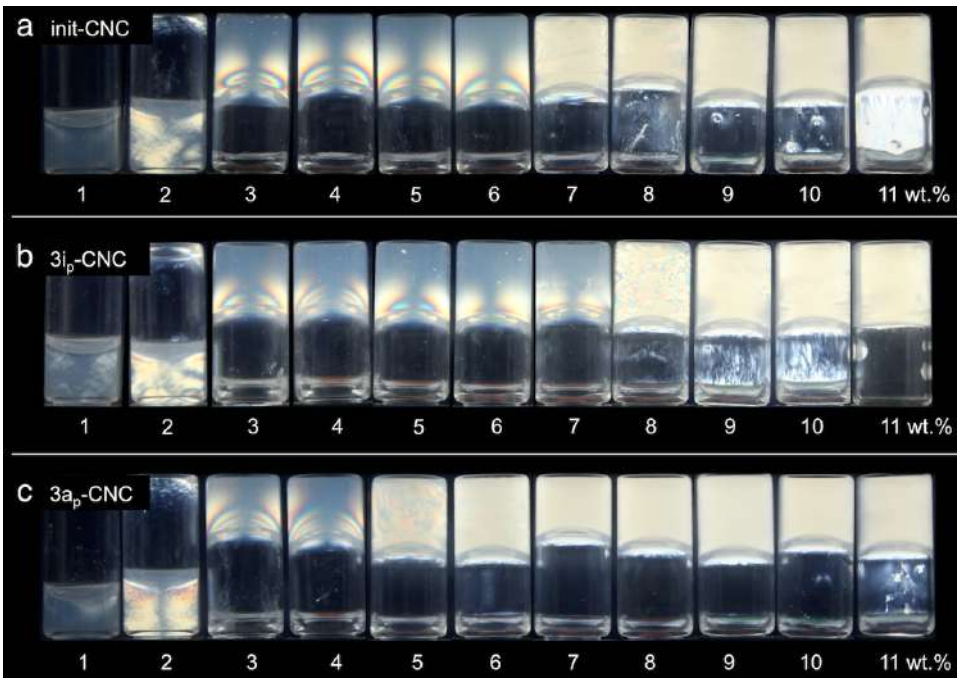

Figure 5.6: Gelation induced by salt addition. Inverted CNC suspensions (initial (a) and fractionated (b,c)) between crossed polarizers, with different CNC mass fractions w but constant sodium ion concentration $c_{Na^+} = c^g_{Na^+}$, adjusted by the addition of NaCl. The samples stood upside down for 2 weeks after reaching gelation by the addition of NaCl. From Honorato–Rios *et al.* [2].

observation is that all gelled samples show birefringence, a sign of the development of long-range orientational order. In fact, the salt-induced birefringence even precedes gelation, as evidenced by the observation of birefringence in the samples in Figure 5.6 with a low CNC content ($w \leq 2$ wt.%) that are still fluids. Similar behavior is observed at the limit of colloidal stability in a previous study of CNC rods in solvents with varying permittivities [51]. The particle aggregation induced by salt addition seen in Figure 5.6 thus appears to happen preferentially with rods aligned with each other.

5.4 End-to-end aggregation

The fact that birefringence appears prior to 2 wt.% CNCs in Figure 5.6 suggests that the end-to-end rod aggregation takes place locally, generating finite linear chains with a sufficiently high effective aspect ratio to induce liquid crystalline order in small domains. However, the overall particle fraction is not yet sufficient for percolation, even at this salt-induced increased effective aspect ratio. The percolation threshold for linear chains is apparently reached at 3 wt.%, as all samples at this or higher CNC contents enter the gel state in the presence of sufficient NaCl.

Figure 5.7 shows AFM images of init-CNC originally at $w = 2$ wt.% (diluted prior to AFM

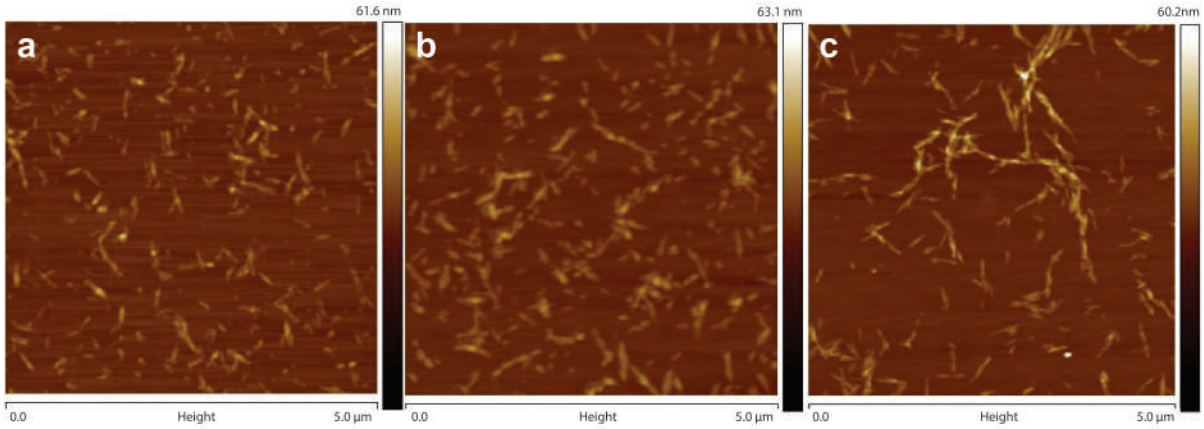

Figure 5.7: CNC chain-building upon salt addition. AFM images of init-CNC at $w = 2$ wt.% in the pristine state (a) and after the addition of NaCl: (b) $c_{NaCl} = 20$ mM and (c) $c_{NaCl} = 40$ mM. From Honorato–Rios *et al.* [2].

imaging), in the pristine state and after the addition of NaCl at two different concentrations. From these images, the rods indeed aggregate largely in parallel and end-to-end upon salt addition, growing into much longer chains. The average diameter of these chains is $d \approx 5.5$ nm, which is not significantly larger that the diameter $d \approx 4$ nm of the individual rods in the salt-free sample. The increased length and small increase in diameter suggests that aggregation takes place mostly between the extreme ends of the rods rather than through side-by-side association of the rods. After the addition of 40 mM NaCl, L/d increases from ≈ 57 (CNCs without salt) to ≈ 130. Xu *et al.* [91] and Honorato-Rios *et al.* [2], performed rheology experiments using CNC suspensions with added NaCl for a range of different salt concentrations. The authors concluded that at high salinity, electrostatic repulsion is reduced and the particles aggregate, allowing the formation of a percolating network. In fact, Xu and co-authors reported that the suspensions originally fluid at low CNC mass fraction form a strong gel at high salt concentration, conclusions that support our AFM observations.

The question remains as to what exactly causes the linear chain aggregation and the subsequent percolation and physical gel formation at $c_{Na^+} \approx c^g_{Na^+}$. The AFM data with added salt and the observation of birefringence developing in all suspensions with salt addition clearly show that the effective rod length increases thanks to linear chain aggregation when the electrostatic repulsion loses its efficiency.

Signs of CNC rod lengthening induced by the addition of NaCl have been reported before [92–94], although for much lower mass fraction of CNCs and without discussion of the consequences in terms of the macroscopic phase behavior. On the basis of small-angle neutron scattering experiments, Cherhal *et al.* [94] detected branch-free CNC aggregation with increasing length for an intermediate ion concentration (on the order of 10 mM), while the data at 50 mM or higher suggested aggregation with branching. This matches the results of this chapter relatively

well, with the degree of branching at $c_{N_a{}^+} \approx c^g_{N_a{}^+}$. While aggregation of like-charged colloidal particles upon addition of multivalent counterions is well understood, the theoretical framework of the phenomenon triggered by monovalent counterions is not trivial [95, 96], although much experimental evidence exists with various colloidal systems, including CNC suspensions [38, 89, 90, 97, 98]. What is particularly surprising is the observation of chain formation with the CNCs aggregating end-to-end rather than side-by-side, at least at these comparatively high CNC mass fractions.

In a previous study, using CNC in solvents with different permittivity [51], we noted that long-range orientational order developed simultaneously with gelation when the CNCs were suspended in dimethylformamide (DMF). Our proposed mechanism for explaining this observation was that this rather poor CNC solvent does not provide sufficient colloidal stability. The CNC rods aggregate partially, forming linear chains that develop LC order at low mass fraction, but also a continuous percolating network throughout the sample volume, thus triggering gelation. This mechanism is very similar to what we see in the present study, but here we turn water into a poor solvent by adding salt, whereas DMF is inherently inadequate for CNC dispersion.

The question remains as to what exactly causes the linear chain aggregation and the subsequent percolation and physical gel formation at $c_{Na^+} \approx c^g_{Na^+}$. The AFM data with added salt and the observation of birefringence developing in all suspensions with salt addition clearly show that the effective rod length increases thanks to linear chain aggregation when the electrostatic repulsion loses its efficiency.

One of our collaborators from the University of Strathclyde in UK, Mikhail Osipov, proposed that if the concentration of counterion c_{Na^+} is increased, approaching $c^g_{Na^+}$, spatial redistribution of counterions and ions of different type (in the case of NaCl addition) may significantly affect both the total free energy and the interaction between charged CNC rods. Figure 5.8 presents a cartoon illustration of our reasoning for the case of low c_{Na^+} (a) and high c_{Na^+} (b), respectively. At low c_{Na^+}, the positive counterions are more or less evenly distributed around the CNC rods. They screen the negative surface charge somewhat, but this screening is effectively independent of location. Hence, if any two rods approach each other, as shown in (a), they experience a repulsive force F_r that keeps the rods separated. In contrast, when $c_{Na^+} \approx c^g_{Na^+}$, there is an excess of counterions, and they may redistribute themselves around the two closely separated rods in order to reduce the total free energy which may result in an effective attraction between rods (Figure 5.8b).

The reason for the average alignment of the rods need to be further investigated, taking into consideration the distribution of the surface charges (and counterions) around the rod, in ad-

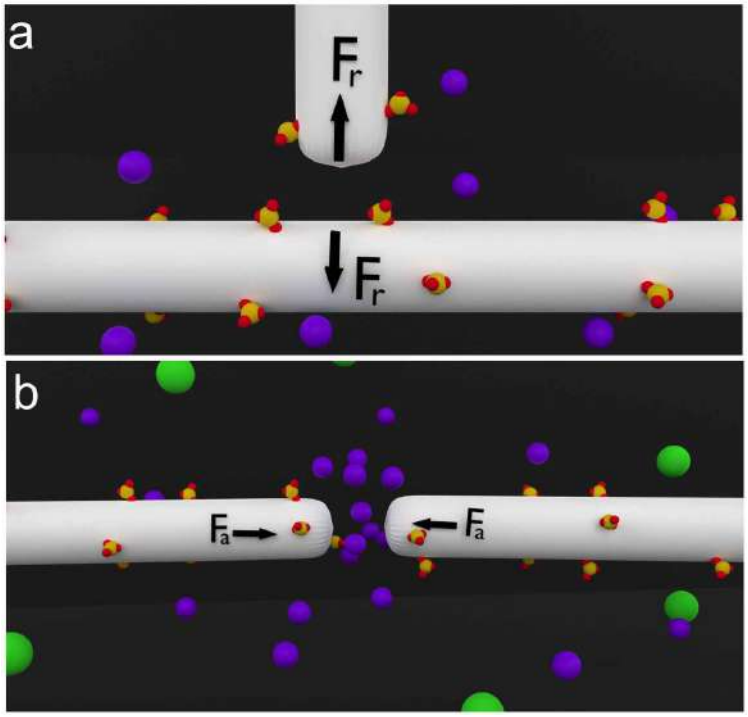

Figure 5.8: Cartoon illustration of the proposed mechanism for linear chain aggregation at high ionic strength concentration of counterions c_{Na^+}. (a) At low c_{Na^+} the counterion distribution (purple Na^+) is uniform and two approaching rods experience effective repulsion. (b) At high c_{Na^+}, small fluctuations in counterions (now also considering green Cl^-, in case of salt addition) can give a large reduction in free energy if there is local excess of positive counterions between two negatively charged rod tips, giving rise to an effective attractive force.

dition to the overall electrostatic and van der Waals interactions between particles. The rod ends may have less surface charges (or even none at all) than the sides. If there is a significant reduction in charge density at the ends, it could explain this end-to-end aggregation.

We note that it is also possible to have kinetic arrest into a soft glassy state with colloids of rod-shaped nanoparticles with high L/d at extremely low ionic strength. Kang and Dhont [99,100] reported the loss of equilibrium LC behavior for filamentous viruses beyond a critical volume fraction, yet this only happens at very low salt content. Their explanation was based on non-contact between the rods, the electrostatic repulsion instead being so effective at these low ionic strength values that the rods find themselves in an "electrostatic cage" if the particle volume fraction reaches a threshold value. While the macroscopic behavior of this kinetically arrested sample may appear similar, the physical mechanism is clearly different, and the condition of low ionic strength is indeed the opposite of what we discuss here, which is the most relevant situation for CNC suspensions.

5.5 Summary

By the spontaneous segregation according to L/d, that takes place as the LC phase separates from the isotropic surrounding, to divide the CNC suspension into two fractions with predominantly high and low L/d rods, respectively, this chapter shows that L/d has no impact on the gelation, while it indeed strongly favours liquid crystallinity (as discussed in Chapter 4). Thus, both fractions and the original suspension surprisingly have identical values of w_g, but the fraction with high L/d rods shows w_0 and w_1 much lower than in the initial suspension. Significantly, from an applied point of view, while the initial suspension had $w_1 \approx w_g$, the high L/d suspension has w_1 substantially below w_g, meaning that we have gained access over a large CNC mass fraction range where the complete sample is in an equilibrium chiral nematic phase. After the results presented in this chapter, together with Chapter 4, I can conclude that the gelation at w_g is due to the loss of colloidal stability due to the concentration of counterions reaching a threshold value regardless of the original rod aspect ratio.

Chapter 6

Helix pitch of the equilibrium cholesteric CNC phases

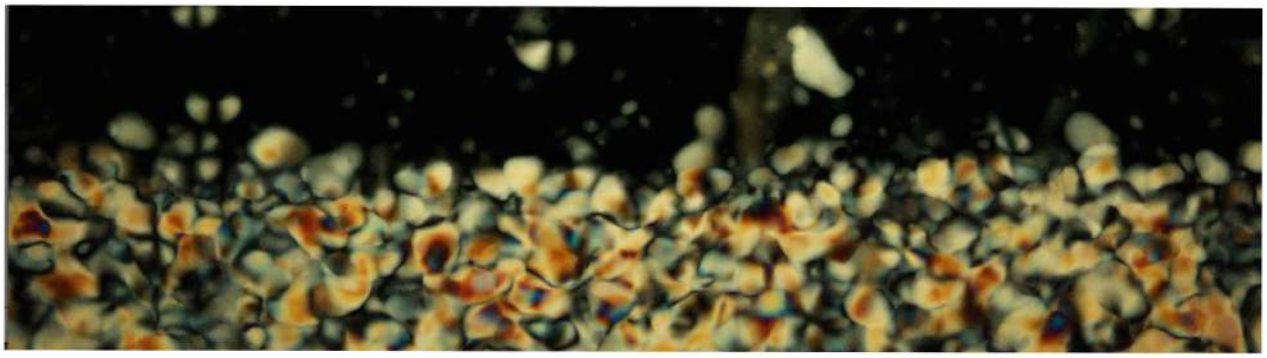

Overview of this chapter

Studies on the chiral nematic pitch in CNC suspensions have not been able to fully explain the self-organization of the nanorods once they have reached equilibrium. This chapter presents the effect of the rod size and type and concentration of counterion on the final pitch in samples prepared after the fractionation procedures in Chapter 4. It is shown that the counterion concentration plays a crucial role in the determination of the helix pitch, which is corroborated by preparing CNCs with different counterions and counterion concentrations. However, as the primary effect of the counterion concentration is to influence the effective rod volume, the counterions also affect the phase diagram. In fact, it may be that the counterion effect on the pitch occurs via the effect on the phase diagram and on the effective rod volume fraction in the system, hence this may be the primary influence. To finalize this chapter, I replicate the experimental method presented by Hirai *et al.* [1], and give some tentative explanation to their observations on pitch and phase diagram.

6.1 Introduction

As explained in Chapter 2, particles in the chiral nematic phase present a long-range orientational order, particularly with a helical periodicity in which they organize. This local alignment is known as the director—frequently represented as **n**—and the distance for which the director rotates until it completes a full rotation is known as *pitch*. Onsager described the role of entropy on the spontaneous development of the long-range orientational order in colloidal liquid crystals [17]. Nevertheless, it was Straley who presented decades later the first theoretical work on chiral nematics [101]. His seminal work has been extensively used in current studies to predict the pitch of several colloidal systems [102, 103].

In aqueous CNC suspensions, the pitch is typically found in the range of 10-50 μm, nevertheless after evaporation, the pitch decreases to values in the nanometer scale, resulting in the reflection of visible light according to Bragg's law with the characteristic iridescent colorful films [104–109]. All experimental studies on CNC nanorods report a decrease in pitch as the particle mass fraction increases, regardless of the cellulose source [1,34,38,72,92,110]. A common assumption is that the increase in chiral species (more CNC in suspension) might provoke a stronger twisting force in the system, as is the case for thermotropic cholesterics [111]. At the same time, the CNC is electrostatically charged and thus the increase in CNC content also increases the concentration of counterions in suspension, decreasing the electrostatic repulsion. Due to this screening effect, the rods get closer to each other. Moreover, in contrast to the case of chiral dopants added to a thermotropic LC, the chiral dopant is also the mesogen in the case of CNCs. Thus, increasing the concentration of chiral particles also raises the overall volume fraction of mesogens, increasing the chances of mutual influence between rods, whether chiral, electrostatic or steric. The link between concentration of chiral species and cholesteric pitch is thus highly complex, as we are changing chirality, electrostatic screening, and particle volume fraction, all at the same time.

Using the spontaneous segregation according to L/d presented in Chapter 4, I fractionated an initial CNC suspension, obtaining CNC fractions with different rod aspect ratio distributions. For the rods with high L/d, it is possible to extend the mass fraction range for which the sample is fully cholesteric, allowing not only the comparison of pitch values between CNCs with a variety of L/d, but also the determination of pitch values for a much broader mass fraction range (beyond the two-phase regime) compared to data for unfractionated suspensions that have been reported so far. This chapter also presents possible answers to unexplained data reported by Hirai *et al.* [112]. Similar experiments were carried out based on their work and the main results are presented at the end of this chapter.

6.2 Formation of the cholesteric CNC phase

When increasing the CNC mass fraction w for dilute pristine CNC samples, the sequence normally starts with an isotropic suspension of disordered rods. Beyond a certain w, a more ordered liquid crystalline (LC) phase forms, in coexistence with the isotropic phase persisting in the rest of the sample, with a pitch p commonly ranging from 3 μm to 10 μm in samples studied in this thesis (measured in the LC phase of the suspension). For higher w, normally in the range of 10 – 12 wt.%, the system enters the kinetically arrested state discussed in the previous chapter, preventing the entire sample to enter the LC phase. In general for colloidal liquid crystals, if the volume fraction ϕ of rods is increased, starting from a fully isotropic suspension, the LC phase will separate as nuclei, so-called tactoids or spherulites [31]. Tactoids then grow and merge and eventually the macroscopic LC phase forms. A clear evidence of this LC formation process is presented in Figure 6.1. I filled an open glass capillary with a CNC suspension that presents a volume fraction of LC phase slightly above $\Phi \approx 0$ after phase separation. The water slowly evaporated from the sample on the stage of the polarizing microscope with the capillary in horizontal position. Defining the time of filling as time $t = 0$, we observe tactoids forming in the isotropic phase after $t = 4$ min. Before this time tactoids were too small for visualization (Figure 6.1b). As water evaporation continues, tactoids meet and merge (Figure 6.1e) into larger domains until a continuous LC phase is observed at $t =$ 70 min (Figure 6.1g), with the typical fingerprint patterns characteristic of cholesteric liquid crystals.

For the sake of allowing an as-simple-as possible explanation of the key events taking place upon tactoid formation, allow me to make the following drastic simplification of the real situation. Let us consider the disperse CNC suspension as made up of N discrete subvolumes, each of which is monodisperse. Let us define $x = L/d$ as the aspect ratio, and let us assume that the subvolume with the longest rods has aspect ratio x_1 and the subvolume with the shortest rods has aspect ratio x_N. Thus, $x_1 > x_i > x_N$, where we introduce the variable i for indexing the subvolumes. According to Onsager, the rod volume fraction where the isotropic phase in the subvolume $i = 1$ becomes unstable is $\phi_0^{i=1} = 3.3/x_1$, hence if the overall rod volume increases above this value, tactoids will develop, with rod volume fraction $\phi_1^{i=1} = 4.5/x_1$. Assuming that the overall rod volume fraction is still lower than $\phi_0^{i=2} = 3.3/x_2$, no other tactoids will be formed.

However, if we do increase the overall rod volume fraction to $\phi_0^{i=3} > \phi > \phi_0^{i=2}$, some more tactoids with rods of aspect ratio x_1 will nucleate, and in addition tactoids containing rods with aspect ratio x_2 will form, at a local rod volume fraction $\phi_1^{i=2} = 4.5/x_2$. We can define $w_0^{i=1}$ and $w_0^{i=2}$ as the CNC mass fractions corresponding to $\phi_0^{i=1}$ and $\phi_0^{i=2}$, respectively, and

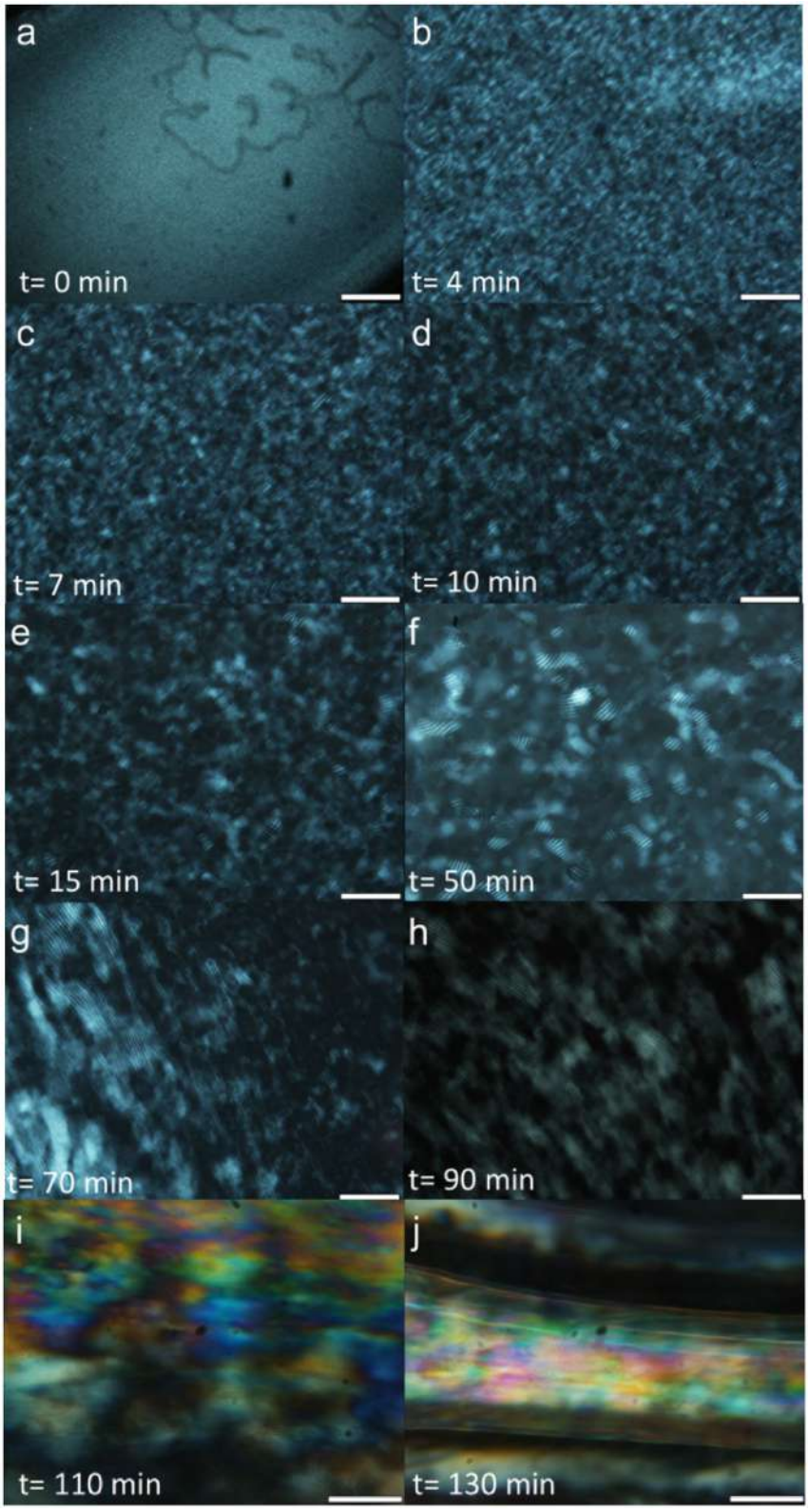

Figure 6.1: Formation of the liquid crystal phase in an open-ended horizontally aligned capillary filled with high L/d CNC sample at 3 wt.%. The scale bars correspond to 200 μm.

analogously for w_1 and ϕ_1. Most likely, both mass fractions are still far from the threshold for gelation, w_g. If we wait sufficiently long, all tactoids will sink in the gravitational field to the bottom, due to their higher density compared to the isotropic surrounding, where they will merge and form a continuous liquid crystal phase.

Extending this over-simplified model to a much later stage in the process of increasing the mass fraction, we will at some point arrive at the situation where $w_1^i = w_g$, which means that the tactoid, soon after its nucleation, should enter a gelled state. The surrounding isotropic phase still has a CNC fraction $w < w_g$, hence it remains fluid. This means that the $w_1^i = w_g$ tactoids will still sink to the bottom, but, since they are gelled, they cannot merge with other tactoids. Instead of a continuous liquid crystal phase at the bottom, we will thus have a sediment containing discrete tactoids that never merge with their surrounding.

Even later in the process we would eventually reach the situation where $w_0^i = w_g$. This means that the isotropic phase gels, and the whole sample becomes kinetically arrested. Any tactoids that did not yet sediment will remain suspended forever. I stress that the model used here is grossly over-simplified, ignoring totally any interactions between rods of different length and assuming a discrete subdivision that does not exist in reality. The reason I use such a simple model is that I believe that it *qualitatively* captures the key events going on as water evaporates from an initially low-concentration disperse CNC suspension. At least it allows an explanation of the experimental data that I will present in the following. While a correct description of the process would need to take one of the more recent theoretical frameworks developed for modeling disperse nanorod suspensions as its starting point, the advantage of this oversimplified picture is that the argument can be depicted using only Onsager theory. My understanding is that the qualitative results, with a three-stage division between fluid tactoids in a fluid environment, to gelled tactoids in a fluid environment, to gelled tactoids in a gelled environment, will still apply after a more rigorous treatment, but the tactoids will of course have some dispersity in themselves and the quantitative relations will be much more involved. My hope is that my experimentally founded explanation can motivate theoretical physicists to model the sequence of events in a way that is also quantitatively correct.

In the rest of this chapter, I will describe my observations on a variety of CNC suspensions filled into glass capillaries with rectangular cross section. The capillaries were sealed and vertically stored at room temperature for minimum 1 month before characterization. All the pitch values were determined by measuring the distance of two consecutive stripes in the fingerprint texture. More details of the characterization procedures in Chapter 2, subsection 2.6.6.

6.3 Effect of rod aspect ratio on the chiral nematic pitch

Studies on CNC derived from different cellulose sources have shown that p generally decreases as w is increased [113,114]. However, none of the published studies has considered the fact that the rod average L/d in the LC phase coexisting with the isotropic phase varies depending on the overall mass fraction of the CNC sample. From our results presented in Chapter 4, larger rods populate the LC phase in samples with low w, while shorter rods remain in the isotropic phase for samples with high CNC content. It is in this context that a relevant question arises whether this difference in L/d is the reason for the variation in p — and if not, what else can explain the pitch reduction upon increasing CNC mass fraction?.

I start the investigation by evaluating the influence of L/d on the equilibrium helix formation. For this, p was determined in fractionated samples prepared from two different experimental procedures with both sets of suspensions obtained from the same initial CNC. Samples prepared from repetitive separation of phases and starting in the middle of the phase diagram ($\Phi = 0.5$) were used together with CNCs from the mass fraction-driven fractionation protocol (with $\Phi = 0.2$ and $\Phi = 0.8$). Complete size characterization and plots of phase diagrams are presented in Chapter 4, Figure 4.12 for samples from $\Phi = 0.5$. Figure 4.13 presents the characterization of the samples obtained from the mass fraction-driven protocol.

In Figure 6.2, the helix pitch of the long-rod fractions obtained after repetitive separation of the LC phase ($3a_f$-CNC, $4a_f$-CNC, $5a_f$-CNC), and the short-rod fractions obtained from multiple separation of the isotropic phase ($3i_f$-CNC and $4i_f$-CNC) are plotted against the total CNC mass fraction w.

For the long-rod fractions p stays relatively constant ($p \approx 9$ μm) with increasing w, from the onset of LC formation to the end of the two-phase regime (3 wt.% $< w <$ 4 wt.%). Afterwards, the CNC suspensions enter the fully LC range, decreasing p monotonically with increasing w. Although the differences in p are not very large between the three long-rod fractions, values of p in the $3a_f$-CNC samples are slightly lower compare to $4a_f$-CNC and $5a_f$-CNC suspensions, especially in the two-phase regime.

This difference is most likely not the difference in L/d itself, but rather that the lower L/d value of the 3a fraction compared to the other fractions, leads to a higher w_1 value and thus a higher CNC content in the LC phase. This corroborates well with the fact that all three fractions have essentially identical values once the two-phase region is passed, because then the CNC content in the LC phase is actually what is indicated on the x-axis. If now I plot the average pitch values of the two-phase regime for each of the long-rod samples against the CNC mass fraction of the LC phase w_1 (Figure 6.3), we observe that p decreases as w_1 increases, as

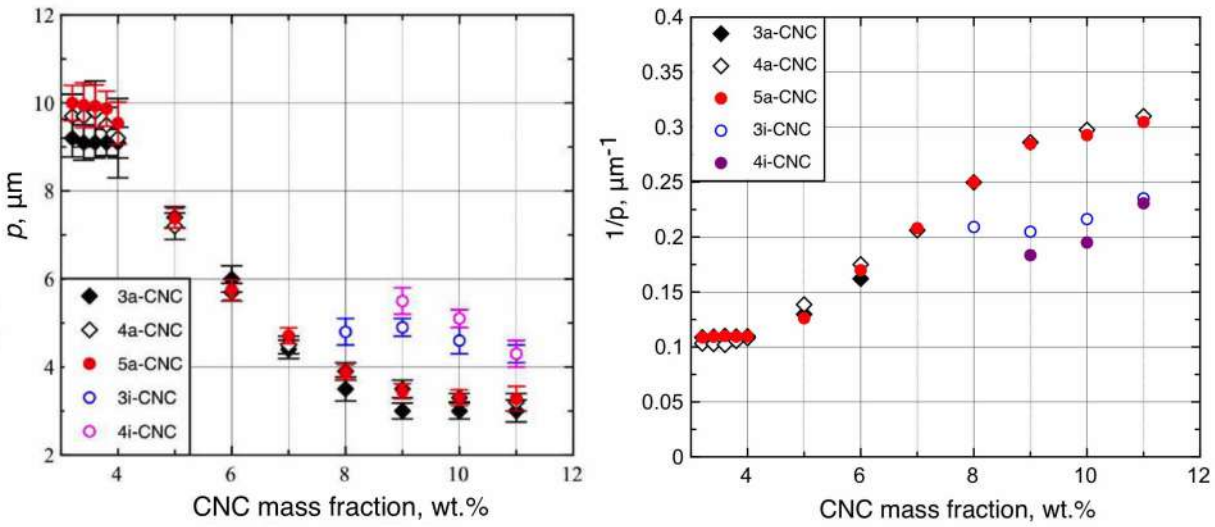

Figure 6.2: Left: Chiral nematic pitch p for fractionated samples against total CNC mass fraction w obtained after the repetitive phase separation of an init-CNC with $\Phi \approx 0.5$. Right: Inverse p (twisting power) as a function of w. Note that all values for short-rod fractions ($3i_f$-CNC and $4i_f$-CNC) are obtained for such high values of w_1 that the cholesteric phase in a tactoid gels or gets very close to gelation. This means that the helix cannot reach its equilibrium value and the pitch values for these fractions must thus be considered separately from the equilibrium values obtained for long-rod fractions, up to $w \approx 10$ wt.%. It is likely that the values also for long-rod fractions at $w = 10$ and $w = 11$ wt.% are not equilibrium values due to the vicinity of gelation, explaining the deviation from linear behavior in the $1/p$ diagram for these w values.

expected for CNC suspensions.

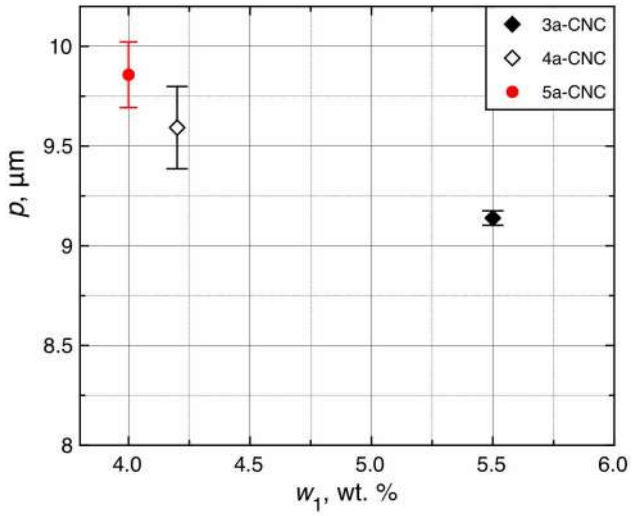

Figure 6.3: Plot of the average pitch p in the two-phase regime presented in Figure 6.2, against the CNC mass fraction of the LC phase, w_1, for $3a_f$-CNC, $4a_f$-CNC and $5a_f$-CNC samples. Values of w_1 are taken from Table 4.3 in Chapter 4. The lower L/d in the $3a_f$ fraction compared to $4a_f$-CNC and $5a_f$-CNCs, leads to higher w_1, which results in a decreased p as expected for CNCs.

When the data are plotted as the inverse of p against w (in the right of Figure 6.2), the slope would correspond to the chiral strength of the CNC rods, in the interpretation that is frequent in research on thermotropic cholesterics, where $1/p$ is typically a linear function of the chiral dopant concentration in the limit of low concentration. A steep slope indicates stronger helical twisting power (HTP), while a gentle slope reveals weaker HTP [115]. Usually this index might be considered to represent the helical structure produced by introducing a given concentration of chiral dopant molecules into a non-chiral nematic liquid crystal phase, and it is important to remember that the HTP is defined for the limit of vanishing chiral dopant concentration [116].

In fact, it is common in practice that the $1/p$ vs w curve deviates significantly from the linear bahavior once the chiral dopant concentration exceeds a few percent. I present in Figure 6.2b $1/p$ against w for all the different fractionated samples. We observed a linear increase for w in the range of 4 wt.% to 9 wt.% for the long-rod fraction. The long-fraction CNCs exhibit very weak HTP, estimated to $\sim 0.04\ \mu\text{m}^{-1}$. However, the interpretation of the data in terms of HTP is not without problems. In the normal definition of HTP, the independent variable is the concentration of a chiral dopant added to a preexisting non-chiral nematic host phase. In this case, the chiral dopant is also the mesogen, and the host phase is isotropic liquid water. It is thus far from obvious that definition of an HTP value for CNC is meaningful.

From Figure 6.2, the departure from linearity for 3a, 4a and 5a fractions might be because the helix does not reach equilibrium within the time frame of the experiments for these high w values. Perhaps gelation is close enough already at $w = 10$ wt.% that it becomes impractical to measure the equilibrium pitch.

The situation for the short rods differs from the previous results for two main reasons. First, the two-phase regime is shifted to considerably higher values of w compared to the long-rod fractions, thus a complete LC phase cannot be reached in practice because $w_1 > w_g$. The second deviation is the formation of tactoids that do not merge over time, due to the gelation occurring within the tactoids. From Figure 6.2, p is slightly larger in the $4i_f$-CNC fractions compare to $3i_f$-CNC (the $4i_f$-CNC contains rods with lower average L/d compared to $3i_f$-CNC). I believe that the reason for this variation is the inability of the short rods to form an equilibrium LC phase. Instead, the short rods formed tactoids that gelled due to the high counterion concentration in very short-rod tactoids. As shown in Figure 4.15 in Chapter 4, tactoids have remained in the isotropic phase of short-rod suspensions kept vertically for more than 2 years, which shows that eventually the whole sample gels. If now we plot $1/p$ against w for the short rods (Figure 6.2), the helical twisting power is $\sim 0.02\ \mu m^{-1}$, even weaker than for the long-rod fractions. However, this result should be interpreted with even more caution than for the long rods, for two reasons. First, as already mentioned, the pitch data for short rods is likely not representative of equilibrium conditions. Second, all data for the short-rod samples

are obtained within the biphase regime, where the rod mass fraction stays the same within a tactoid, hence we should see no variation in the pitch within that tactoid as the overall CNC mass fraction is increased. Therefore, should some data actually correspond to equilibrium, any variation is due to the averaging over tactoids with different L/d and thus different w_1.

To corroborate these results, values of p and $1/p$ for the four fractions obtained from the mass fraction-driven procedure, are plotted against w and the curves presented in Figure 6.4. Full size characterization and phase diagrams of the CNC samples are shown in Figure 4.13, Chapter 4. As expected for each series, p decreases monotonically with increasing w, without important variations between the four fractionated suspensions. The fact that this trend in pitch is not affected by the size of the rods, especially by the short ones, can be rationalized in terms of aspect ratio. The rods in the $i_{0.8}$–CNC (short-rod fraction) prepared after the mass fraction-driven procedure are longer than the rods presented earlier ($3i_f$-CNC and $4i_f$-CNC). This has an effect on Φ, reducing the w_1 value within tactoids once LC formation has started (far away from gelation). For the four curves presented in Figure 6.4b, we observe a linear increase of $1/p$ with increasing w, and an estimated HTP of $\sim 0.03\ \mu m^{-1}$.

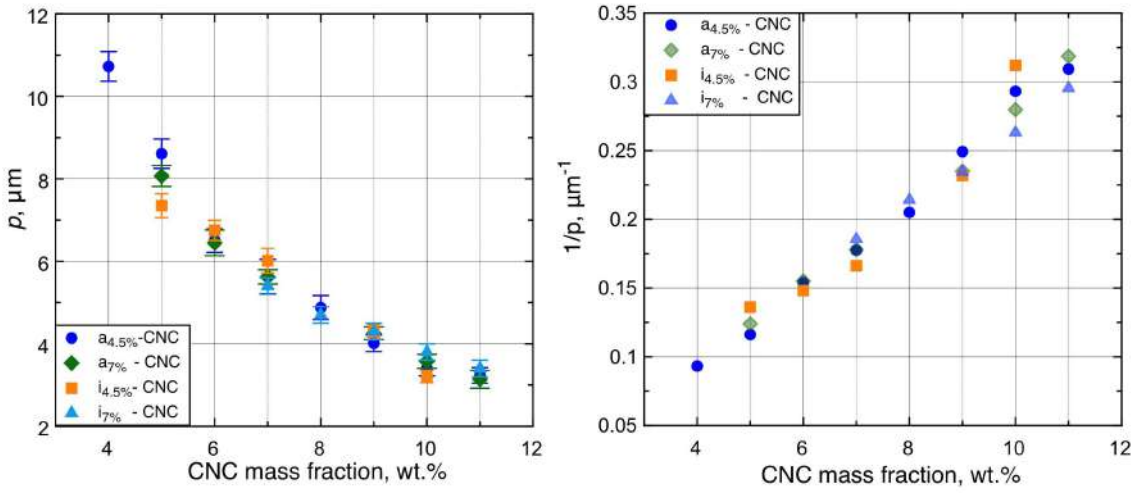

Figure 6.4: (Left) Chiral nematic pitch p of fractionated samples against CNC mass fraction w and (right) the inverse of pitch p plotted against the CNC mass fraction w. The samples have been prepared using the mass fraction-driven protocol presented in Chapter 4. The error bars correspond to the standard deviation of 70 different measurements per sample capillary.

The study of the effect of L/d on the helix pitch is challenging, basically due to the impact of the rod size on the threshold volume fraction Φ and the difficulties in obtaining equilibrium pitch values when w approaches w_g. The fractionation procedures presented in this thesis have shown to be highly efficient, allowing us to obtain suspensions with rods with important geometrical differences. However, when working with the short-rod fractions, suspensions in the two-phase regime will be obtained while the long rods will present fully liquid crystalline phase. In addition, the formation of tactoids by the very short rods could lead to wrong conclusions,

not only in terms of incomplete phase separations and non-equilibrated pitch values, but also for the formation of final films as we will see at the end of this thesis.

For the case of rods with very low L/d ($3i_f$-CNC and $4i_f$-CNC), we reached a point where $w_1 > w_g$ within the tactoid, meaning that it has entered a gelled state shortly after its nucleation. This can explain why tactoids do not merge, even after long times in glass capillaries. Finally, the LC phase cannot anneal into its equilibrium state, resulting in tactoids with p values that are greater than the equilibrium value.

6.4 Effect of counterions on the helix pitch

The electrostatic stabilization of CNC rods allows the system to remain stable over time and thus CNCs are able to form cholesteric phases after high enough mass fractions. Typically, CNCs present either protons (H^+) or sodium (Na^+) as counterions, depending on the strategy of production [43]. Considering that the variation in w, which appears to influence $1/p$ near linearly provided that the point of gelation is not approached, also amounts to a variation in counterion concentration, the question arises as to whether perhaps the observed pitch variation might be related more to electrostatics than to the concentration of chiral species in the system. This subsection presents an investigation of the effect of different counterions on the helix pitch.

6.4.1 Ion-exchange procedure and characterization of the obtained CNC suspensions

In order to study the effect of the type of monovalent counterions on the helix pitch in CNC suspensions, I prepared samples with hydrogen, lithium, sodium and cesium counterions based on the work presented by Dong & Gray [117] in 1997. The authors examined the influence of a variety of counterions on the final properties of CNC suspensions, such as the effect on the phase diagram and on the equilibrium pitch.

As discussed in Chapter 4 and Chapter 5, gelation has nothing to do with the length of the rods while LC formation is largely affected. The fractionation procedure thus allows to substantially extend the equilibrium LC phase by working with the long-rod fraction. The access to equilibrium liquid crystalline samples beyond the two-phase regime leads to a better understanding of which parameters govern the pitch of the helical superstructure that is spontaneously formed in the chiral nematic phase of CNC suspensions.

The schematic illustration presented in Figure 6.5 summarizes the ion-exchange procedure for the preparation of the CNC samples with different counterions. I started with the dilution

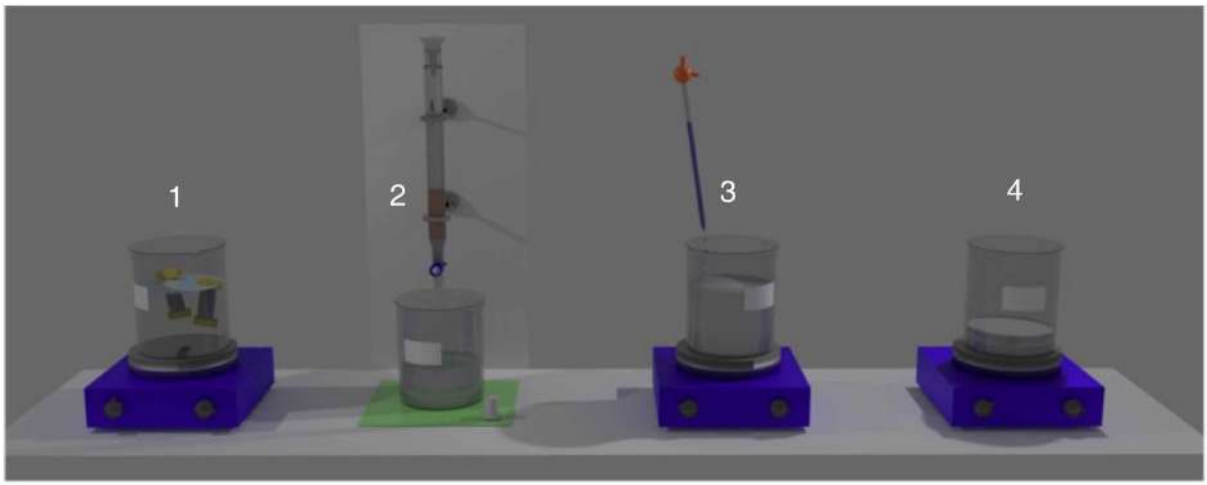

Figure 6.5: Schematic illustration of the ion-exchange process. 1) CNC suspension at $w \approx 1.5$ wt.% is dialysed against ultra pure water. 2) CNC is protonated using an ion-exchange column containing H^+ form resin. 3) The protons on the CNC are exchanged by the corresponding counterion by the addition of a base. 4) The final CNC is concentrated to a desired w.

of a CNC suspension with rods with high aspect ratio to 1.5 wt.% followed by purification using dialysis membranes in ultra pure water for three days with daily exchange of water. After dialysis, the suspension was diluted again to 0.5 wt.% and fed into an ion-exchange column (containing H^+ form resin) for the replacement of all Na^+ counterions, resulting in the protonation of the sulphate half-ester groups (acid-form CNC or H-CNC). CNC suspensions associated with other counterions were prepared by neutralizing the acid form suspension with the corresponding base until its pH was neutral. Finally, concentrated samples were obtained after slow evaporation at room temperature. More details of the procedure are presented in Chapter 2. The results presented in this section for the Na-CNC correspond to the purified CNC suspension after the ion-exchange procedure discussed above. This way we ensure that only Na^+ counterions are present in suspension.

After the ion-exchange procedure, I measured the conductivity and pH of the H-CNC and Na-CNC suspensions with different w and the values are plotted in Figure 6.6.

Conductivity can be used as a measure of the concentration of ions in solution [118–120]. If the concentration of ions increases, so will the conductivity as the concentration of charge carriers increases. Another factor in conductivity measurements is that not all ions carry charge equally. For the case of the small H^+ ions, they move through the suspension at very high speed, whereas larger ions such as Na^+ move at a slower speed. Therefore the results in conductivity will also depend on the size of the ions. Indeed, the measured conductivity is higher for the protonated CNC (H-CNC) compared to its sodium form (Na-CNC), both presenting linear increments of conductivity as w increases.

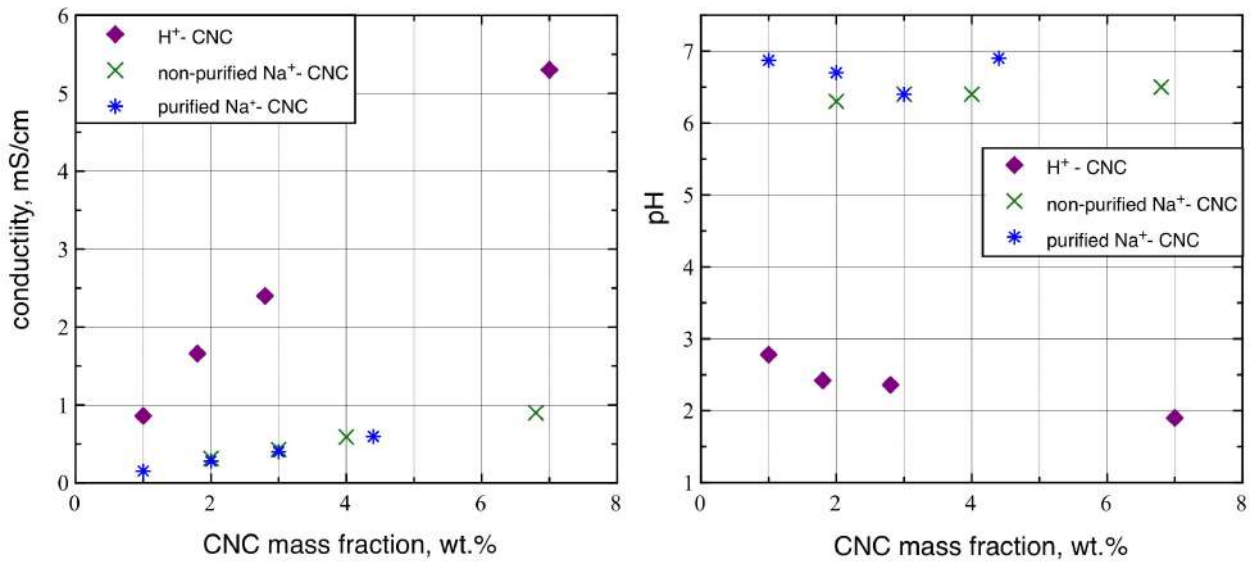

Figure 6.6: Conductivity and pH measurements for commercial sodium form CNC (non purified Na-CNC), protonated form CNC (H-CNC) after ion-exchange column and sodium-form CNC (purified Na-CNC) after ion-exchange process and the addition to the corresponding base for a long-rod CNC sample. These values were measured in samples containing rods with high aspect ratio.

Figure 6.6 also presents conductivity values of the commercial sodium-form CNC (without purification) for w ranging from 1 wt.% to 7 wt.%. These measurements coincide with the conductivity of the CNC suspension after purification and ion-exchange process. This is a good indication that the initial CNC sample is pure, and it can be used without any further treatment. The pH for the Na-CNC suspension shows values in the range of 6 – 7 for the commercial CNC and its purified version, dropping to values in the range between 1.9 - 2.7 for H-CNC in the same mass fraction range. The CO_2 in air tends to lower the pH; this can explain the variation in pH for the commercial Na-CNC.

6.4.2 Equilibrium phase separation and chiral nematic pitch in CNC suspensions with different counterions

Figure 6.7 shows the corresponding phase separations for all the different CNC samples with the variety of counterions. All the suspensions formed chiral nematic ordered phases above a critical mass fraction. From our results in volume fraction presented in Figure 6.7, the series with Cs^+ counterions formed a LC phase at the highest w. However, there are not significant differences for the H^+, Li^+ and Na^+ counterions concerning the onset of the ordered phases. In all cases, as w increases Φ is approximately the same for all CNC samples.

Dong & Gray carried out similar experiments [117] and the authors reported that the isotropic-LC transition can be largely affected by the type of counterions present in the suspension for

the case of organic and inorganic counterions. They concluded that the critical mass fraction for ordered phase formation increases in the order $H^+ < Na^+ < Cs^+$, due to the increase in the repulsive hydration force that grows with the hydration number of the counterion [117]. The

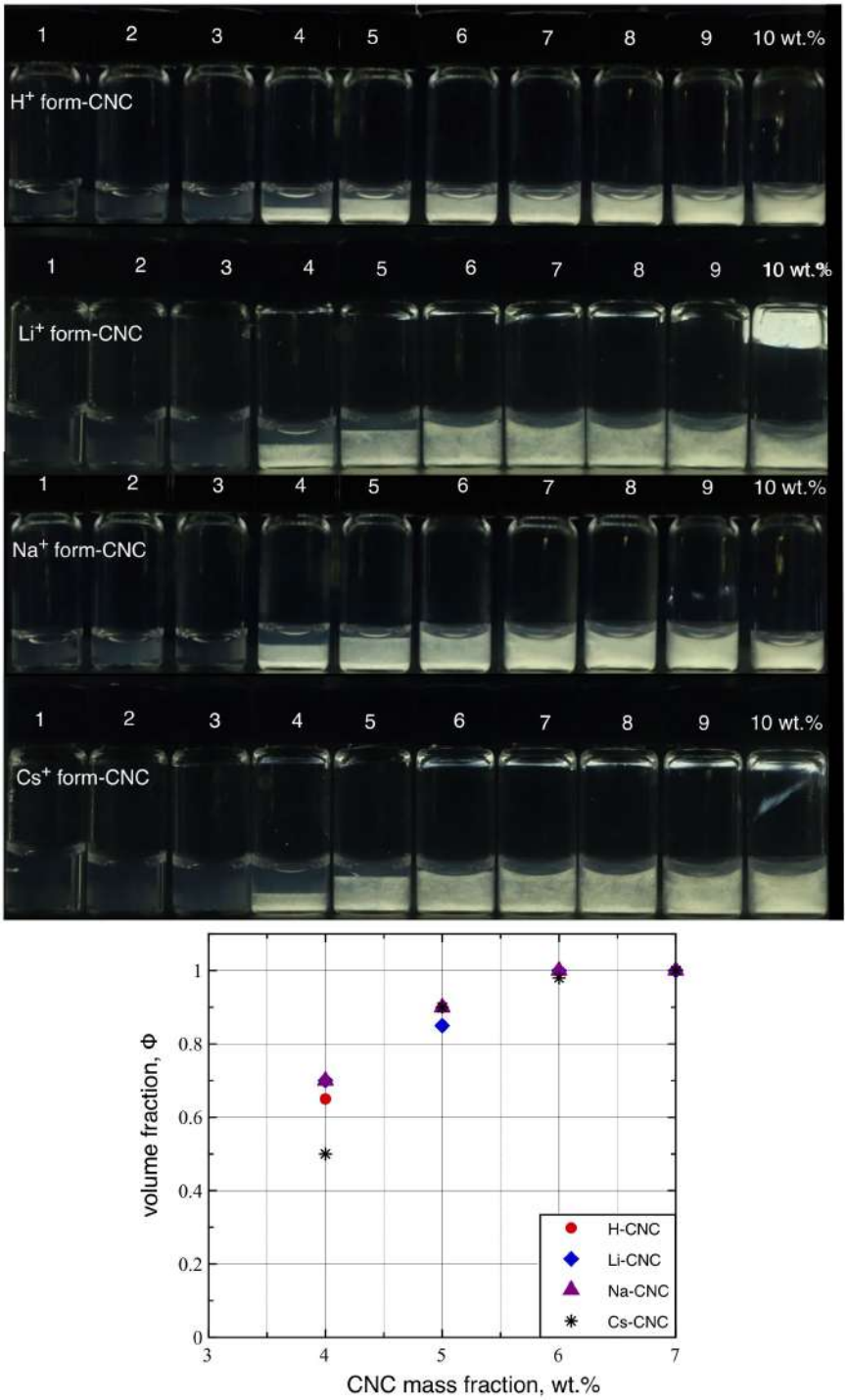

Figure 6.7: Top: Phase separation in suspensions of cellulose nanocrystals between crossed polarizers, protonated fraction (H-CNC), lithium-form fraction (Li-CNC), sodium-form fraction (Na-CNC) and cesium-form fraction (Cs-CNC). Bottom: Quantitative plots of the volume fraction Φ of LC phase for the four series. The CNC suspensions contain rods with high aspect ratio.

hydration number decreases with the size of the counterion, meaning that for the case of Cs^+, this number is the lowest compared to the different ions shown in the study study, see Table 6.1. The increase in the repulsive force will lead to an increase in the "apparent" excluded volume of the rods and thus a decrease in the critical mass fraction for the LC phase formation is expected [38]. If the repulsive force between particles decreases, the critical mass fraction will increase. The drawback of their study is the different starting batch that was used for the preparation of each series of CNCs. The difficulty in performing exactly the same hydrolysis conditions from one batch to a new one is characteristic of CNC suspensions.

The helix pitch for Li-CNC, Na-CNC and Cs-CNC are presented in Figure 6.8. Slight differences in p are observed, with longer p for the Cs-CNC and shorter values for Li-CNC for all the concentrations studied.

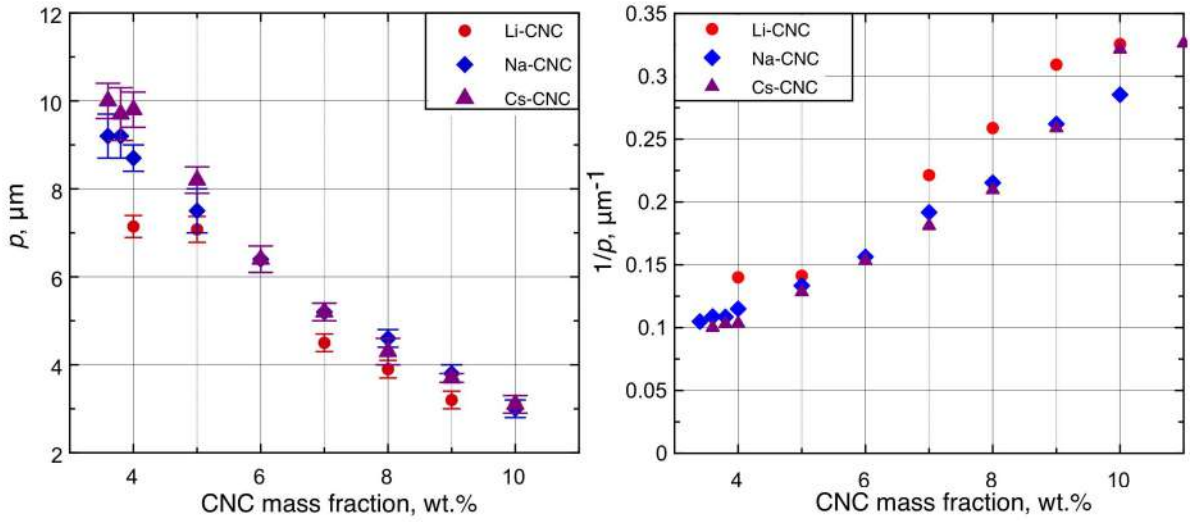

Figure 6.8: Left: Helix pitch in CNC aqueous suspensions for Li–, Na– and Cs-CNCs. Right: The inverse of p against CNC mass fraction. These values were measured in samples containing rods with high aspect ratio. The error bars correspond the standard deviation of 70 different measurements per sample capillary.

Previous studies on counterions have shown that the interaction with a charged surface can be dramatically different, regardless of having ions with the same valence [121–123]. Table 6.1 presents the bare radii of the different ions studied in this chapter apart from H^+, which is a special case due to its transformation into the hydronium ion in water, as well as their hydrated radii and hydration numbers. The bare radius corresponds to the radius of the ion treated as a hard sphere. If the ions are dissolved in water, water molecules will be bonded on the surface, resulting in hydrated ions with larger total radii.

The hydration number gives information of the average number of water molecules that form the primary hydration shell, which corresponds to the first shell of water molecules around a hydrated ion. This first layer is where the water molecules are greatly organized, meaning that

they are restricted in their motion and position [3]. This effect is much weaker after the first shell.

Table 6.1: Hydrated radii and hydration numbers of ions in water. Taken from [3]

Ion	Bare ion radius (nm)	Hydrated radius (nm)	Hydration number
Li^+	0.068	0.38	5
Na^+	0.095	0.36	4
K^+	0.133	0.33	3
Cs^+	0.169	0.33	1

Although all ions studied in this subchapter are monovalent ions and part of group 1 from the periodic table (charge +1), their differences in bare ion and hydrated radii play an important role in the interactions with other surfaces.

Considering that Li^+ has the smallest bare ion radius in Table 6.1 with charge +1, it also means that Li^+ has the highest *charge density* compared to all the ions in Table 6.1. The high charge density of Li^+ leads to strong interaction with water molecules, thus a larger hydrated radius compared to Na^+, K^+ and Cs^+. In addition, the strong interaction of the first layer of water molecules with the small ion means that the water molecules will largely be oriented as to compensate the charge, thus the strongly hydrated Li^+ ion is effectively larger than K^+ and Cs^+ ions, and it also has a lower effective charge, due to the more efficient screening by the well-oriented first layer of water molecules. Stating with certainty that variations in the hydration shell are the cause of the observed differences in p would require a more detailed study of the subject. However, I can give a tentative explanation for his behavior, taken into consideration the effect on the hydrophilic rod surface and the ion specificity.

I stress that the decrease in rod-rod distance does not directly imply a decrease in p. The important, and more general question is why p decreases as we move to the right in the phase diagram, towards greater rod volume fraction (and greater mass fraction). On the one hand, the increasing counterion concentration as more rods are added to the system reduces the Debye length and thus the range of electrostatic repulsion, allowing closer encounters between rods. Studies on rod-rod interactions have concluded that intermolecular attraction favors parallel orientation of the rods, while repulsion tends to twist them out of the energetically unfavorable parallel alignment [88]. In fact, Schütz and co-authors [72] calculated the twisting angle of two neighboring rods from the mass fraction-dependent pitch and the average separation distance between the CNCs. They found that the twisting angle increases with decreasing separation distance between adjacent rods, as the overall w was higher. In addition, the authors determined the interaction energy between rods throughout the complete two-phase regime. They reported that at longer separation distances (lower w), the interaction potential is weakly attractive, which can be interpreted as a marginal contribution from the electrostatic repulsion. For short

center-to-center distances (higher w), they found that the interaction energy between parallel cylinders was weakly repulsive. The authors attributed the increase in the twist angle to the tendency of the rods to form a perpendicular alignment (instead of a parallel organization) when the electrostatic repulsion is increased. Although I do not report values either of twisting angle or of separation distance between rods, I can give some general explanations of my results concerning the effect of the counterions on p.

On the other hand, the increasing hydration sheath of smaller counterions should lead to reduced screening of the surface charge and thus increasing Debye length. In the simple picture of two rods that are already aligned within parallel planes, the only variation being the rotation within those planes as they get more or less close to each other due to varying electrostatic repulsion range, weaker surface charge screening would suggest longer plane separation and thus more parallel alignment, hence longer pitch, in contrast to observation. However, the rods are not locked to rotate within a plane and the translation between rods is not a matter of their rotation planes moving more or less close to each other, but we have full three-dimensional freedom of translation and rotation. At increasing overall rod volume fraction, whether achieved by increasing the number of rods (at the cost of reducing the effective *individual* rod volume by introducing more counterions) or by keeping the rod number constant and boosting the effective individual rod volume by reducing the electrostatic screening potential of the counterions (as is the case when the counterions are highly hydrated), there is less freedom to move in 3D space without the influence of adjacent rods, simply due to the greater crowding. This more crowded situation could in fact enhance the effect of electrostatic repulsion on the local director orientation, twisting it stronger as the overall rod volume fraction increases, which could explain, in a general manner, the pitch reduction towards the right in the phase diagram.

6.5 Effect of added salt on phase diagram and helix pitch

In Figure 6.9, the effect of added NaCl at $1< c_s < 10$ mM, with c_s the concentration of the salt, on the macroscopic phase separation for Na-CNC is shown, with the data for the suspension without added salt (Na-CNC salt free) included for comparison. In addition, the corresponding plots of the phase diagrams are presented in Figure 6.10. From the macroscopic phase separation, it is clearly visible that the threshold w_0 for liquid crystal formation is shifted to higher w by the NaCl addition, increasing from $w_0 \approx 3$ wt.% in salt-free CNCs to $w_0 \approx 6.5$ wt.% after the addition of 10 mM NaCl.

The effect of salt on the CNC behavior has been extensively explored in previous CNC studies [38, 42, 92] as well as in theoretical reports related to rodlike polyelectrolytes [124], with similar

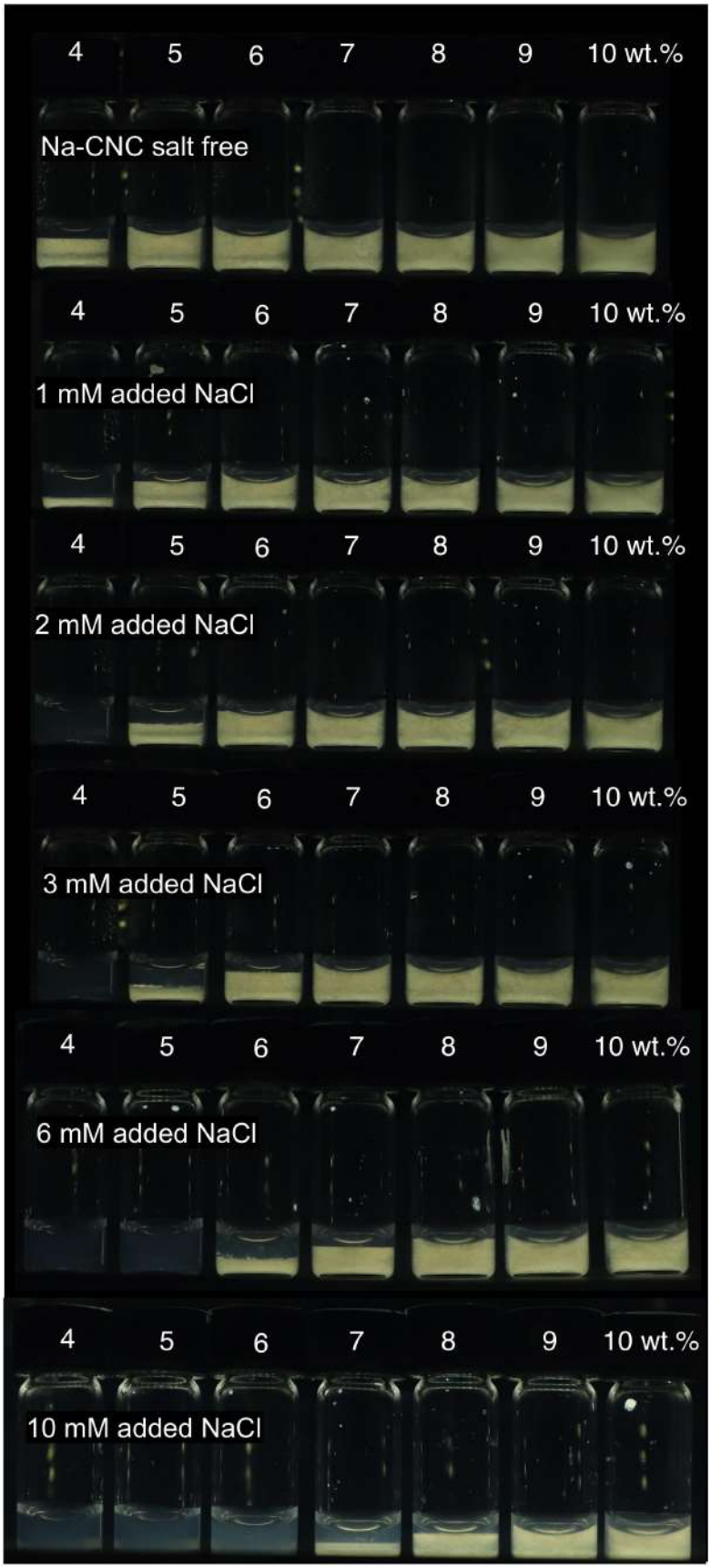

Figure 6.9: Effect of NaCl addition on the macroscopic volume fraction Φ of the LC phase at different CNC mass fractions. The CNC suspensions contain rods with high aspect ratio.

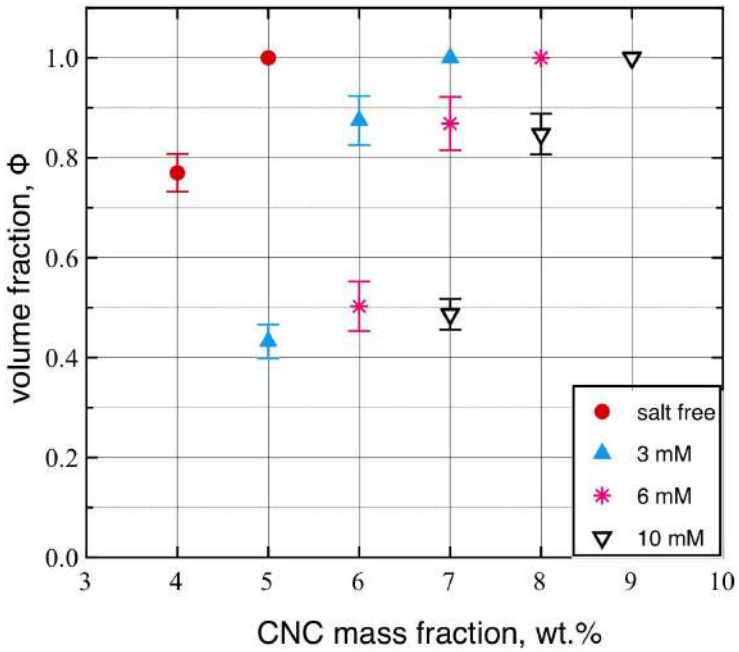

Figure 6.10: Effect of NaCl addition on the macroscopic volume fraction Φ of LC phase at different CNC mass fractions.

results. The electrostatic stabilization of CNCs makes their phase behavior highly sensitive to ions dissolved in water. The variation of w_0 in the phase diagram can be simply explained as a result of the change in the effective particle size [38]. The increased ion concentration after the addition of NaCl reduces the electrostatic repulsion between rods through a reduction of the Debye screening length κ^{-1}, resulting in rods with higher effective L/d than in pristine CNCs. From the Onsager theory, the increase in aspect ratio L/d should enhance liquid crystal formation (if only L/d were affected, it should lower w_0 and w_1 compared to salt-free CNC). However, the contrary effect is observed in Figure 6.9 upon the addition of salt. We explained in a previous study [38] that the increase in w_0 and w_1 can be understood as a result of the reduction in the total effective rod volume ϕ that is also affected by the salt concentration at constant w. This effect dominates over the variation in effective L/d, which changes linearly with κ^{-1} via L/$(d + 2\kappa^{-1})$, while the reduction in ϕ scales with the square of κ^{-1}, $\nu_{rod} = L\pi(d/2 + \kappa^{-1})^2$ [38].

Figure 6.11 shows the corresponding variation in p for the different samples as a function of CNC mass fraction w and NaCl addition c_s. As expected for salt-free CNC, p decreases as the CNC mass fraction increases, from $p \approx 9$ μm to $p \approx 3$ μm. The sensitivity of the pitch to salt is significantly weaker than for the phase diagram, but at 10 mM NaCl the pitch is distinctly smaller than for the other salt concentrations, perhaps suggesting that the salt addition would have a direct effect in reducing the pitch. However, at this high salt concentration, the phase diagram has changed so much that the 7 wt.% data point with the largest offset compared to lower salt additions is also situated deeply within the two-phase coexistence. This means

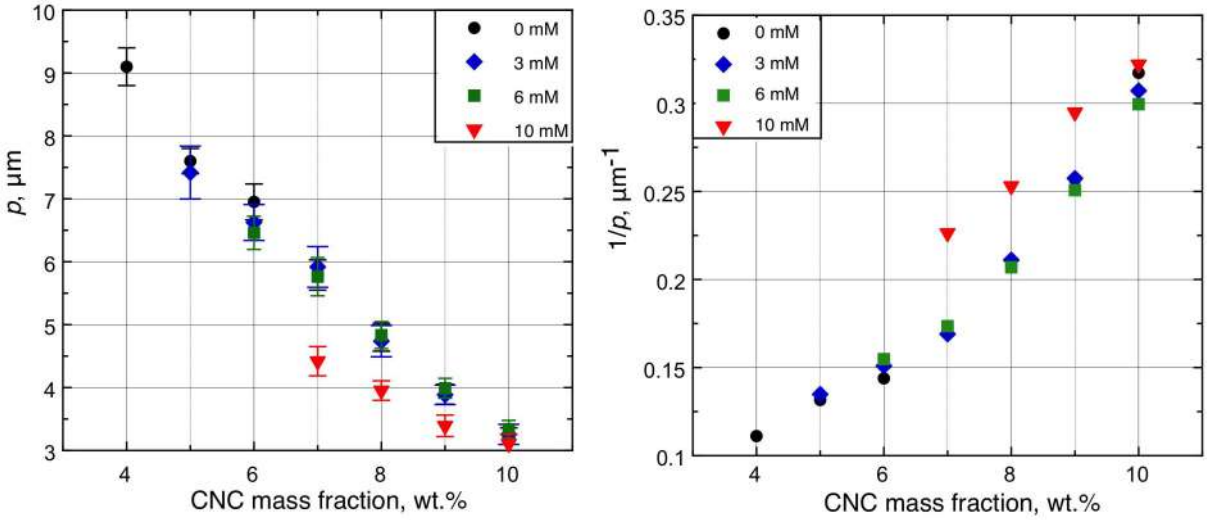

Figure 6.11: Left: Effect of NaCl addition on the helix pitch p against CNC mass fraction. Right: The inverse pitch against CNC mass fraction for CNC suspensions after salt addition. These values were measured in samples containing rods with high aspect ratio.

that the CNC mass fraction in the cholesteric tactoids where the pitch can be measured is much higher than 7 wt.%. Looking at Fig. 6.10, the w_1 value for reaching a completely liquid crystalline sample is between 8 wt.% and 9 wt.% at 10 mM NaCl, so the pitch value should correspond to this value on the x-axis. If we translate the 10 mM salt pitch value for 7 wt.% *overall* CNC mass fraction to $w \approx 8.5wt.\%$, also this pitch value falls very well on the general trend of pitch versus CNC mass fraction. This suggests that the salt addition in fact has no *direct* influence on the pitch, but it only influences it by shifting the CNC fraction w_1 at which the cholesteric phase develops. The fact that the pitch decreases throughout the two-phase regime of the 10 mM NaCl series, opposite of the behavior without salt when comparing long and short rods (Fig. 6.2), may indicate that we here have such high mass fraction of CNC that the effect of approaching w_1 introduces so many extra counterions that w_1 increases in the process, thus increasing the mass fraction of CNC in the cholesteric tactoids. From our previous studies in cotton-derived CNC [38] and as discussed in the previous subsection, we understood the decrease in pitch in terms of screening of the negative surface charges on the CNC rods by the sodium cations, Na^+, from the added salt. However, the pitch reduction does not come from this screening per se, but rather from the increase in CNC volume fraction in the liquid crystalline phase that the screening gives rise to.

While the addition of salt shifts w_1 to higher mass fractions, the CNC mass fraction for which the sample becomes a gel decreases, resulting in samples with narrowed equilibrium two-phase regime compared to the original salt-free CNC. This situation restricts the amount of salt that can be added and thus, restricts the range over which we can study p in this way.

Comparing with literature, I found that Hirai *et al.* [1] reported an interesting reversing behavior

upon NaCl addition. The authors reported decreasing values of Φ for c_s up to 1 mM (as expected). However, for higher c_s the LC fraction began increasing, supposedly reaching $\Phi = 1$ already for $c_s \approx 2$ mM at $w = 3$ wt.%. In addition, the authors observed that p increases with increasing salt addition after a threshold value of added salt. I present my results concerning this behavior at the end of this chapter.

6.5.1 Effect of constant counterion concentration on the phase diagram and helix pitch

Based on the observations on the impact of L/d on p, I hypothesize that the variation in p upon increase in w is caused by the counterion concentration since the CNCs are the only source of Na^+ ions in the system. To corroborate this hypothesis, I attempted to prepare CNC samples within $w = 4$ wt.% to 10 wt.%, aiming to maintain constant counterion concentration c_{ci} by the addition of salt. To accomplish this, c_{ci} was calculated for each mass of the CNC suspension without added NaCl, according to:

$$c_{ci} = c_{SO^{-3}} = w_S \frac{\rho w}{M_S} \tag{6.1}$$

where w_S is the sulfur mass fraction determined by conductometric titration in Chapter 5, ρ the density of the suspension that for simplicity is approximated to 1 kg per liter of suspension, M_s the molar mass of sulfate and w the CNC mass fraction for which c_{ci} is being calculated.

Using equation 6.1, c_{ci} was calculated for three different w and the values are presented in Table 6.2.

Table 6.2: Counterion concentration c_{ci} for different w.

w, wt.%	c_{ci}, mM
8	31
9	34
10	38

I added the corresponding salt to each CNC sample in order to reach c_{ci} presented in Table 6.2. After the salt addition, each sample vial was mixed using a vortex mixer for 2 min. Experiments using sodium-form CNC (Na-CNC) and lithium-form CNC (Li-CNC) were performed, both samples prepared by the ion-exchange process presented earlier in this chapter for the long-rod CNC fraction. LiCl was used for the experiments with Li-CNC and NaCl for the Na-CNC sample.

The macroscopic phase separations for Li-CNC (salt-free) and for the samples after the addition of LiCl are presented in Figure 6.12. From the quantitative plots of the relative volume fraction,

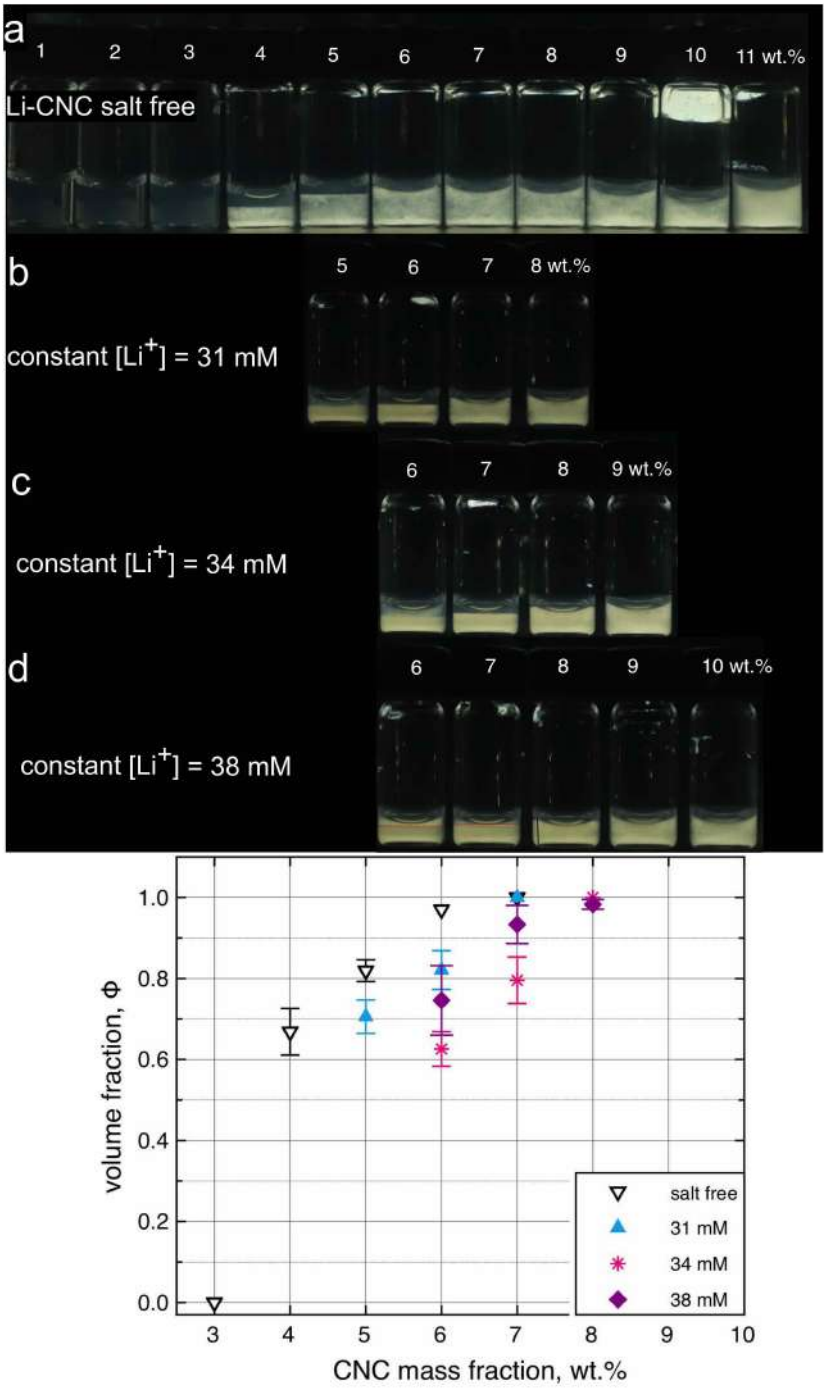

Figure 6.12: a) Lithium form CNC (Li-CNC) salt free after ion-exchange. b-d) Li-CNCs with constant counterion by the addition of LiCl, according to Table 6.2. The bottom image corresponds to the plot of the phase diagrams against w for the different series. The CNC suspensions contain rods with high aspect ratio.

Φ increases monotonically but not linearly from 0 to 1 with increasing w for the salt-free Li-CNC, which is a characteristic tendency for pristine CNC suspensions. The situation changes for the samples containing constant lithium concentration. For those cases we observe a *linear* increase of Φ with increasing w, as expected from the Onsager theory [17]. Also, w_0 is shifted to higher mass fraction as observed from previous experiments with salt addition. The linear behavior can be understood in terms of Debye screening length κ^{-1}. The electroscatic interactions are not included in Onsager theory, which expects a linear increase of Φ for increasing particle mass fraction. For charged rods, the thickness of the electrostatic double layer (κ^{-1}) depends on the ionic strength in the system. For the CNCs, counterions are brought into the suspension by the CNCs themselves. This results in a difference between the physical rod size and its effective value including κ^{-1}, which changes depending on the CNC mass fraction. This behavior can explain the levelling off of the curves of Φ and the linear tendency for samples at constant counterion concentration [4]. Dong *et al.* [42] carried out similar experiments with protonated CNCs (H-CNC). They maintained constant pH in a concentrated CNC suspension by extensive dialysis against water containing HCl, followed by the addition of HCl to the suspension in order to have constant concentration of H^+ (or constant pH) within a range of mass fractions, resulting in a similar linear tendency for Φ values against w.

Figure 6.13 and Figure 6.14 present the obtained results of p and its inverse value with the addition of salt in order to reach constant counterion concentration for Na-CNC and Li-CNC samples.

The pitch continuously changes with w for both salt-free samples, with p consistently slightly smaller at a certain w when the counterions are Li^+ than when they are Na^+. Note that the data points with salt added generally belong to the two-phase coexistence region, hence their pitch data correspond to higher CNC mass fraction than that of the overall sample. Comparing with Fig. 6.12 for Li^+ counterions (the behavior for Na^+ counterions is analogous) we see that the pitch value throughout the series corresponds roughly to that obtained for a CNC mass fraction where the full sample is liquid crystalline ($w = w_1$). This means that the constant pitch is to be expected, as in fact all samples correspond to an identical liquid crystal phase, at a CNC mass fraction of w_1. Interestingly, the trend in p at constant ion concentration is slightly different depending on the nature of counterion. For the Na-CNCs, p is nearly independent of w for the CNC samples when the counterion concentration is kept constant by salt addition. However, for the Li-CNCs in Figure 6.14, the data reveals a small decrease in p with increasing w even at constant counterion concentration, for all three values of c_{ci}. This is more visible when plotting $1/p$, on the right of Figure 6.14. Even so, the variation is much reduced, as expected when considering that the liquid crystal phase has higher mass fraction of CNC than the overall sample. The slight remaining variation with Li^+ counterions needs further work to

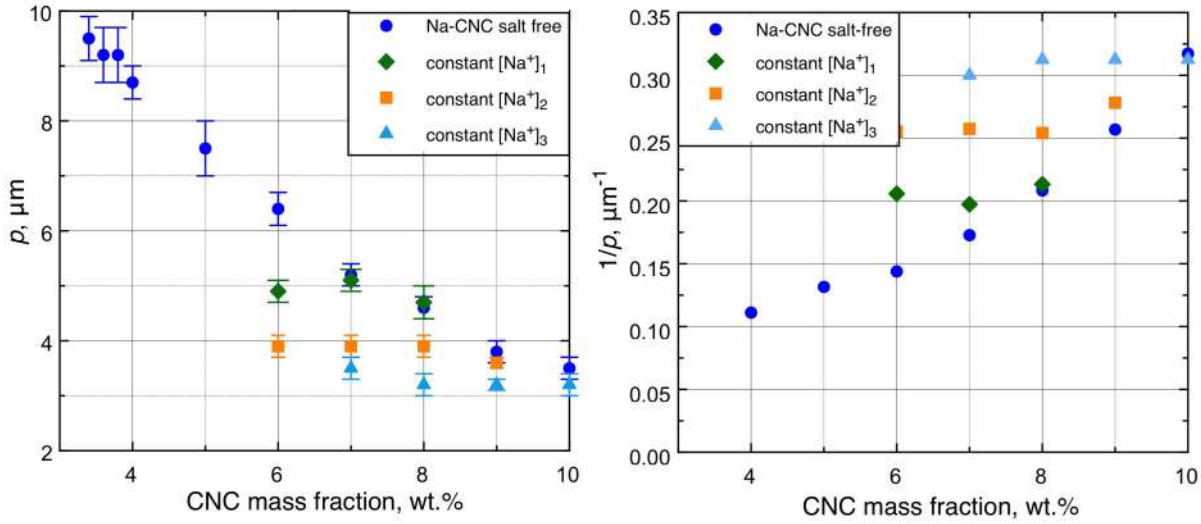

Figure 6.13: Effect of constant c_{Na^+} by NaCl addition on the helix pitch p against w. Left: Values of p of Na-CNC series with three different constant c_{Na^+} as well as for salt-free Na-CNC. Right: The inverse p for each curve against w. These values were measured in samples containing rods with high aspect ratio.

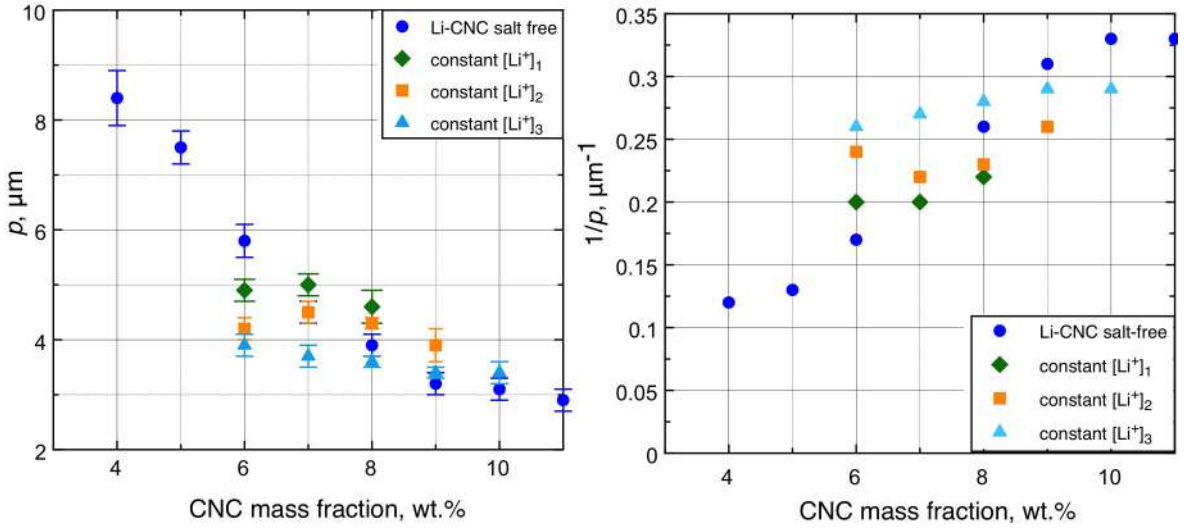

Figure 6.14: Effect of constant c_{Li^+} by LiCl addition on the helix pitch p against w. Left: Values of p of Li-CNC series with three different constant c_{Li^+} as well as for salt-free Li-CNC Right: The inverse p for each curve against w. These values were measured in samples containing rods with high aspect ratio.

be explained. Reflecting the much reduced dependence of p on w, the HTP is reduced from $\sim$ 0.04 to $\sim$ 0.003 μm^{-1} for the constant Na^+ concentration. For the case of the Li^+ ions, the HTP is reduced to 0.01 μm^{-1}.

I cannot explain the trends for p for monovalent ions just by applying electrostatic interactions since the ion specificity can be very confusing. As explained above, although the valence is the same among all the different ions studied in this thesis, they do not interact in the same way with the negatively charged surface. The DLVO theory assumes that the stability in colloidal system is mostly dictated by the attractive van der Waals interactions and the electrostatic repulsion, meaning that an unstable colloidal suspension can be the obtained after the addition of salt [122].

The nature of the twist in the chiral nematic phases is still a debated topic [72,125,126], and my thesis is far from proposing a mechanism that could explain this behavior. However, my results can contribute to a better understanding of this topic, especially when it comes to explaining the decrease in p as the CNC mass fraction increases in the suspension.

By purely entropic arguments, Straley [127] explained the cholesteric phase based on the hard-core fitting of screws. He suggested that the upper rod may approach the lower most closely, if the particle axis is twisted with respect to the axis of the lower particle, leading to a smaller excluded volume for the twist state, permitting the closest approach. If now we consider charged particles, there exist two main mechanisms that may explain the twist at least in CNC suspensions [4]. First, the typical description of the chirality transfer of the molecular cellulose to the macroscopic liquid crystal phase, characteristic of thermotropic cholesterics. In this case, the higher content of chiral species that are present in the sample, the stronger the twisting force will be in the system. For CNCs, this can be understood in terms of CNC content: the more CNC particles in the suspension, the shorter the p in the liquid crystal phase. However, the increasing of CNC charged particles will also increase the ionic strength of the system, due to the presence of more counterions in the suspension [4]. This will decrease the distance between particles due to the screening of the surface negative charges on the rods.

Another mechanism that has been reported for CNCs [128] as well as for DNA [126] is also related to the ions and to the effect of the electrostatic repulsion on the effective diameter of the rods. If we consider that the origin of chirality is the twisted geometry of the particles, this twisted shape is somehow less evident by a neighboring particle at low CNC mass fractions. The low ionic strength in a suspension with low mass fraction results in a large Debye length, and thus, greater effective diameter. Araki [129] suggested that the rods lose their chiral character in this situation, which results in CNC suspensions with large pitch. On the contrary, if now we consider CNC suspensions with high mass fractions, the twist shape is much more evident by

a neighboring particle, since the Debye length becomes very small at high ionic strength, and this results in an effective diameter that approaches the hard rod limit [86], thus the effective particle has the shape of a twisted rod, which then results in shorter pitch values. As mentioned above, higher rod volume fraction means a more crowded environment, strengthening the rod-rod interaction frequency which should also enhance the impact of chiral interactions, e.g. by twisted shapes.

I believe that all the possible explanations about the origin of chirality presented above contribute somehow to the understanding of the self-assembly of rod-like particles in lyotropic cholesteric LCs. Perhaps the model from Straley could explain the handedness of the system. If we think about the rods as right-handed screws, once two of the particles approach each other, they will start forming a left-handed helical structure. The opposite handedness would be observed if now the screws are left-handed.

If now I consider my results on pitch, especially by working with the long-rod fraction CNC after running systematic ion exchange studies, I could demonstrate that the helix pitch of CNC suspensions is primarily a function of CNC content. This should not be interpreted as a statement that the pitch is a function of the concentration of chiral material (as typical for thermotropic cholesterics), because the effective rod volume fraction by varying counterions or their concentration does not change the amount of chiral material, although it may influence the strength of chiral interactions. It would be a very interesting experiment to mix in non-chiral rods with a CNC suspension and see if the more presence of rods decreases the pitch. However, these rods would need to be similar in dimensions to CNC, with equal ease in dispersibility in water, in order to be a good reference material. Such rods are not easy to find. The pitch is also not affected by the aspect ratio of the rods (at least within the range investigated).

I have to carefully distinguish the counterion concentration and the ionic strength of my system. I calculate the ionic strength I of a CNC suspension at a certain mass fraction according to:

$$I = \frac{1}{2} \sum z_i^2 c_i \tag{6.2}$$

with z_i the charge of the ion i and c_i its concentration in the suspension. In my CNC system without any salt addition, the main ions are the sodium ions Na^+ and the suphate group SO_3^- that are bonded to the CNC rods. As I previously mentioned, Gray and co-authors [130] carried out experiments aiming at maintaining constant ionic strength by having constant pH for a CNC mass fraction range. This procedure is suitable to be performed since he was dealing with protonated CNC, meaning that the pH value was a measured of the protons in the suspension. The authors carried out their experiments at constant counterion concentration,

without including the contribution of the negative sulphate groups to the ionic strength. In our case:

$$I = \frac{1}{2}(c_{SO_3^-} + c_{Na^+}) = c_{SO_3^-} = w_S \frac{\rho w}{M_S}, \tag{6.3}$$

with $c_{SO_3^-}$ and c_{Na^+} the concentration of the sulphate group and sodium ions, w_S the sulphate content in wt.%, ρ the density of the suspension at a given mass fraction w and M_S the molar mass of sulphur. If now I calculate I using $w = 9$ wt.%, $I = 30.9$ mM.

If now, I carry out the same exercise with a CNC suspension at $w = 8$ wt.% with added NaCl in order to have the same counterion concentration as the previous CNC sample at $w = 9$ wt.%, I would change according to:

$$I = \frac{1}{2}(c_{SO_3^-} + c_{Na^+} + c_{Na^+} + c_{Cl^-}) == w_S \frac{\rho w}{M_S} + c_{NaCl}, \tag{6.4}$$

with c_{Na^+} and c_{Cl^-} the contribution to I from the concentration of the Na^+ and c_{Cl^-} ions, respectively, and c_{NaCl} the concentration of the added salt.

Considering w= 8 wt.% and $c_{NaCl} = 3.4$ mM, with c_{NaCl} the necessary salt concentration to add in order to have equal Na^+ concentration as in a CNC suspension at 9 wt.%, the resulted I after the addition of salt is increased to 30.9 μM, which is the same ionic strength that I calculated earlier, for a CNC sample at 9 wt.%.

6.5.2 Repetition of experiments reported by Hirai *et al.* [1]

One of the objectives of this thesis is to provide clear explanations of important experimental observations that are currently not understood, such as the anomalous phase and helix pitch behavior as a function of added electrolyte reported by Hirai *et al.* in 2009 [1]. They presented a very interesting study where aqueous suspensions of bacterial CNC with mass fraction in the isotropic-chiral nematic coexistance regime were studied, with and without addition of NaCl.

This bacterial CNC had exceptionally high aspect ratio rod and rather low surface charge, hence the isotropic phase lost its stability at the very low CNC content of $w_0 \approx 0.6$ wt.%. The authors did not report the value of w_1, presumably because $w_1 > w_g$, although no information is given in the paper regarding gelation. For $w = 3$ wt%, yielding a chiral nematic volume fraction $\Phi \approx 0.6$ without salt, the authors added increasing amount of NaCl. As I presented in Chapter 3, the salt addition initially reduced Φ, an observation that can explained with the dependence on

ionic strength I of the effective rod volume fraction ϕ, regardless of whether dissolved ions come from CNC or added NaCl. The increase in ionic strength reduces the electrostatic repulsion and thus the excluded volume, hence NaCl addition at constant w leads to a reduction in ϕ, thus counteracting LC formation. Surprisingly, however, the authors found the trend suddenly reversing at around 1 mM NaCl, the LC fraction appearing to diverge and becoming $\Phi^{app} = 1$ for salt concentration of 2 mM or higher. In addition to the unusual tendency of Φ, the authors also reported an increasing pitch beyond a salt concentration of 1 mM.

I attempted to perform similar experiments although using commercial wood-derived CNC in the as-received form. This type of rods presents shorter rods ($L/d \approx 60$) and higher charge density (around 15 times higher) compared to the bacterial-derived CNC. Full characterization of this CNC suspension has been presented in Chapter 3. For this purpose, I prepared an initial suspension at a mass fraction of 6 wt.% (which yields $\Phi \approx 0.6$). The initial batch was then split into smaller samples to which I added increasing amounts of NaCl, resulting in CNC samples with a NaCl concentration in the range from 0 mM (without salt) to 30 mM. Figure 6.15 shows the phase separation behavior of the commercial CNC samples with the different salt concentrations. All sample vials have been standing for 4 months before imaging.

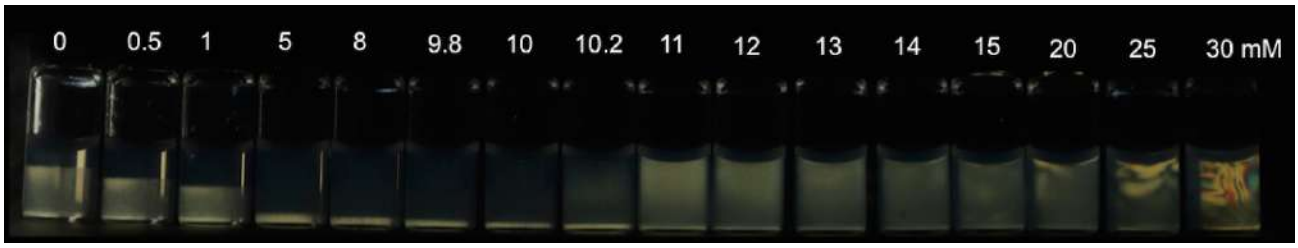

Figure 6.15: Phase separation for the as-received CNC at 6 wt.% with different added concentrations of NaCl, as indicated above each vial. The sample vialwhich all contain the same overall sample volume, are placed between crossed polarizers.

The volume fraction of the LC phase decreases with increasing NaCl, reaching a minimum at $c_{NaCl} \approx 10$ mM. With a further increase in salt concentration, it seems that the sample suddenly has turned completely liquid crystalline —as Hirai *et al.* presented in their work— until it reaches gelation at $c_{NaCl} \approx 25$ mM.

Figure 6.17 shows the effect of the added salt on the fingerprint textures of the CNC suspensions presented in Figure 6.15, filled into flat capillaries, as observed by polarized optical microscopy. The formation of liquid crystalline tactoids surrounded by dark isotropic phase is seen in all samples with $c_{NaCl} > 0.5$ mM. However, for $c_{NaCl} \approx 11$ mM, tactoids populate the entire sample capillary, giving the misleading impression that a fully chiral nematic phase has been formed.

The chiral nematic pitch was determined for all the CNC samples with different c_{NaCl}, the results presented in Figure 6.16. The measured pitch initially decreases with increasing c_{NaCl},

reaching a minimum at $c_{NaCl} \approx 8$ mM, and then increases with the added salt until 11 mM. The general tendency of decreasing pitch upon salt addition is nevertheless largely discussed in literature, where the general explanation is the reduced effective rod volume fraction, as discussed in the previous section.

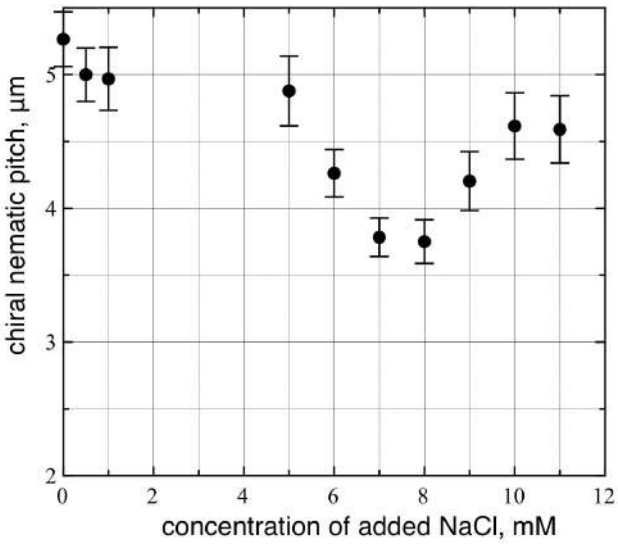

Figure 6.16: Effect of NaCl concentration on the the experimentally determined chiral nematic pitch of the LC phases for a fix cellulose mass fraction of 6 wt.%. As explained in the main text, the data for $c_{NaCl} > 8$ mM represent non-equilibrium, kinetically arrested helix structures, and should thus be interpreted differently than the data at lower salt concentration.

For the determination of pitch values, I measured the distance between two adjacent stripes from the fingerprint textures that were captured by polarized optical microscopy (details of the method in Chapter 2). Clearly, these textures must correspond to the bottom phase (or the cholesteric part of the sample, after phase separation) of the CNC sample. For the case of CNCs with added salt, tactoids remain in the isotropic phase without merging, which could lead to complications when measuring the final pitch. As long as a macroscopic phase separation is observed (regardless of the presence of tactoids in the upper part of the sample), I only measured pitch values in the lower phase. From Figure 6.17, at $c_{NaCl} = 9$ mM tactoids are visible in the entire capillary. From the sample vials presented in Fig. 6.15, there is a thin lower cholesteric phase at 8 mM $< c_{NaCl} <$ 10.2 mM, which is not fully appreciated from the POM images. The epoxy glue that I used for sealing the extremes of the capillaries covered part of the bottom phase, without any visible lower cholesteric part for $c_{NaCl} \geq 9$ mM.

From Figure 6.16, we observe that the increase in pitch at $c_{NaCl} \geq 9$ mM coincides with the observation of a great number of very small tactoids (and the consequent absence of a significant volume of continuous LC phase, see Fig. 6.17) that completely decorate the CNC sample without merging. For this reason, the data reported correspond to pitch values determined from tactoids until fingerprint textures were not any longer visible, starting from $c_{NaCl} \approx 12$

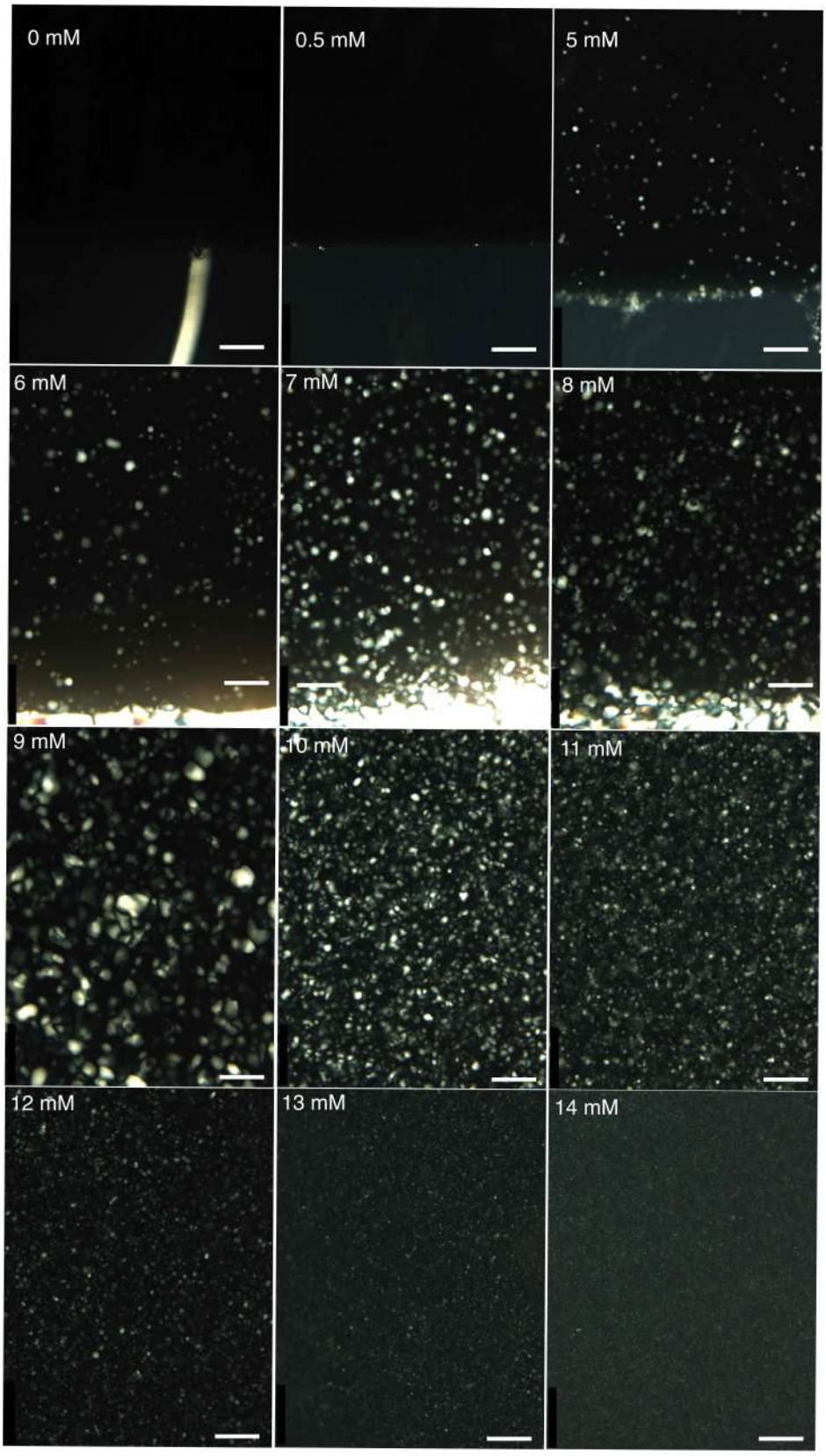

Figure 6.17: Effect of added NaCl on the texture of the LC phase of the commercial CNC suspensions for a fix cellulose mass fraction of 6 wt.%. White scale bars correspond to 200 μm.

mM.

The addition of NaCl provokes shifts in ϕ_0 and ϕ_1 (as discussed in section 6.5 in this chapter), towards higher values (or higher w_0^{NaCl} and w_1^{NaCl}) compared to the salt-free CNC samples. After some threshold of added NaCl, $\phi_g^{NaCl} < \phi_1^{NaCl}$, resulting in gelled tactoids that will never merge but they will sink (Figure 6.16). At this point, the mass fraction in the tactoids is greater than the gelation threshold (which is smaller than w_1). But if the tactoids never sink, then the isotropic background has also gelled, and then the situation is $\phi_g^{NaCl} < \phi_0^{NaCl}$. I am now in a position to explain the surprising pitch versus salt concentration data by Hirai *et al.*, reproduced for my CNC suspensions in Figure 6.16. The key issue to recognize is that the tactoids enter a gelled state, or they get very close to it, beyond salt concentrations where the pitch appears to increase. This means that the helix is never allowed to reach its equilibrium state, and we measure an experimental pitch value that is larger than the equilibrium one. The surprising minimum in pitch in Figure 6.16 is thus due to the fact that the data represent equilibrium behavior for salt concentrations up to that giving minimum pitch, but for higher salt concentrations the data show non-equilibrium values.

6.6 Summary

The extended phase diagram obtained by the high L/d fractions permits a deep study of the helix pitch behavior, varying particle mass fraction, aspect ratio, counterion-type and counterion concentration for a broad range of CNC mass fractions. While it is well known that the helix pitch of CNC suspensions decreases with increasing CNC mass fraction, the reason has not been properly elucidated. Since the only chiral species present is the cellulose, it would be natural to connect the decreasing pitch to the increase in chiral constituents. However, raising the CNC mass fraction also raises the Na^+ concentration and thus gives rise to stronger screening of the charge on the CNC surface. The pitch decrease might thus also be attributed to the increasing ion content. The situation is thus complex, but a synthesis of all the observations described in this chapter may suggest that the key issue is the overall rod volume fraction, not the mass fraction. Another parameter that was assumed important for the pitch is the CNC aspect ratio, and with our fractionated samples, we were for the first time in the position to probe the impact. Within the window of aspect ratios provided by our samples, we could not confirm any dependence of pitch on aspect ratio.

Chapter 7

Control of optical response of dry CNC films

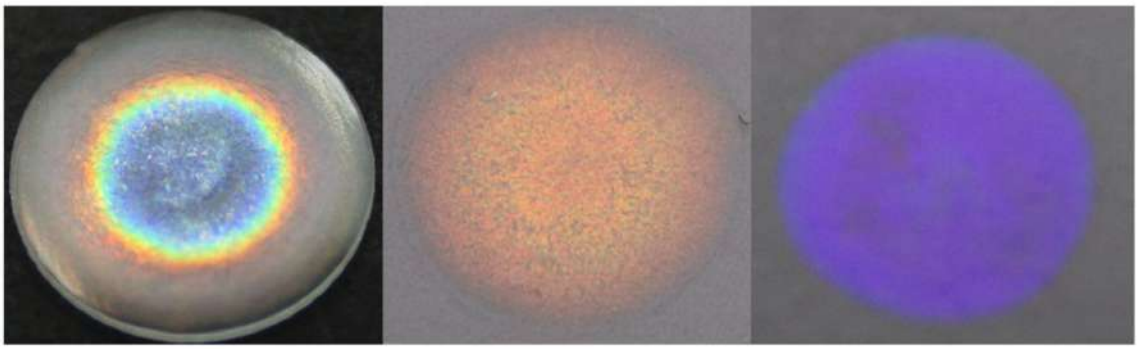

Overview of this chapter

I finalize this thesis by drying CNC suspensions to obtain solid films with controlled optical response. Different parameters are examined such as mass fraction, aspect ratio, surface morphology of the film and evaporation rate. The final films were characterized by polarizing microscopy, profilometry and electron microscopy. The present study emphasizes the crucial role of controlled drying conditions for a proper control of the helix orientation. In addition, by using the longest rods of the CNC distribution, we are able to prepared films which are highly ordered in their rod organization, resulting in incredible uniform colors and reflecting only left-handed circular polarized light, as expected for this type of material.

7.1 Introduction

By drying cholesteric CNC suspensions, films are obtained for which the helix pitch p can reach values as short as the visible-light wavelengths, wavelengths, $\sim$ 400–$\sim$ 700 nm, resulting in the reflection of vivid colors due to the self-assembly of the CNC rods [108, 131, 132]. In this case of structural coloration, gelation is truly an advantage considering that the helical structure of CNCs is "trapped" in this non-equilibrium stage, which permits the production of iridescent films upon evaporation of water.

For most of the possible applications of the CNC films, it is crucial to ensure that the helix is uniformly oriented along with a defined p [53, 133, 134]. However, most of the studies in the field have encountered difficulties in controlling the final properties of the dry CNC films [118, 131, 135–137].

As explained in Chapter 2, the wavelength λ_r selectively reflected from a cholesteric helix, depends on the average refractive index $\bar{n}$, on p and on the angle θ between the incident light and the plane that is perpendicular to the helix axis, according to Bragg's law:

$$\lambda_r = \bar{n} p \cos\theta \tag{7.1}$$

This means that uniform optical response can only be experienced if the helix is uniformly oriented with a defined pitch. The reflected light is circularly polarized and displays the same left handedness as the CNC helix.

The dependence of p on a variety of parameters has been largely studied, such as temperature [135], sonication time [118], application of magnetic fields [131, 132, 138], CNC mass fraction [137], ionic strength, additives [139, 140], among others. Although the mentioned studies have shown possibilities to improve the color uniformity, apparently the slow drying is the key for the formation of highly-ordered structures, which results in films with homogeneous colors [104].

In this chapter, I discuss the impact of the rod aspect ratio and of the drying conditions on the iridescent colors of CNC films by studing the drying of CNC drops containing particles with different aspect ratio (the CNC fractions presented in previous chapters) and with CNC mass fractions in the range of 2 wt.% to 9 wt.% (from isotropic to CNC suspensions near the onset of gelation).

7.2 Preparation and characterization of CNC films

For the preparation of films, 5 μL drops of CNC suspensions were deposited on untreated glass coverslips (coverslips from Roth, with water contact angle of $\theta \approx 55°$) using a micropipette, with the CNC mass fractions in the range of 2 wt.%–9 wt.%.

For the investigation of the impact of the rod aspect ratio L/d on the colors of the films, drops were dried using two fractionated CNC suspensions and the unfractionated initial sample (init-CNC) for comparison. The low aspect ratio particles with $L/d \approx 43$ (referred to as $4i_f$-CNC, corresponding to fourfold fractionated isotropic phase) and $L/d \approx 58$ (referred to as $5a_f$-CNC or fivefold fractionated anisotropic phase). In the case of the init-CNC, $L/d \approx 50$. Size distributions and phase diagrams of each CNC fraction are presented in Chapter 4, Figure 4.8 and Figure 4.12, respectively.

In the following sections, the preparation procedures for films using three different drying conditions are explained. First, I start by drop-casting CNC samples under ambient lab conditions, allowing the suspensions to dry at 22°C and at relative humidity (RH) of 40%. A second set of experiments were carried out by slow drying CNC drops in a glove box. Each drop was deposited on the substrate inside a glove box which was maintained at constant relative humidity of 90% and temperature of 22°C during 7 days. The films were characterized 24 h after their formation.

In order to extend the drying time, I performed experiments with a hexadecane coating, using the experimental procedure recently reported by Zhao *et al.* [104]. With extreme care the experiments were carried out inside a closed glove box to avoid any water evaporation during the preparation of the drops. After deposition of CNC on the glass substrates, the CNC drops were carefully covered with hexadecane. Once all the samples were covered with the inmiscible oil, the samples were removed from the box and the drying process was continued under ambient lab conditions (22 °C and 40% RH) for 5 weeks until the films showed colors. Figure 7.1 presents a schematic illustration of the preparation method discussed in this section.

The height profiles of the films were determined using a stylus profilometer with 2 μm tip radius at 3 mg force, which is able to scan over the sample from edge to edge. In addition, polarized optical images were obtained with a polarizing optical microscope in reflection mode. Details of the experimental methods are presented in Chapter 2.

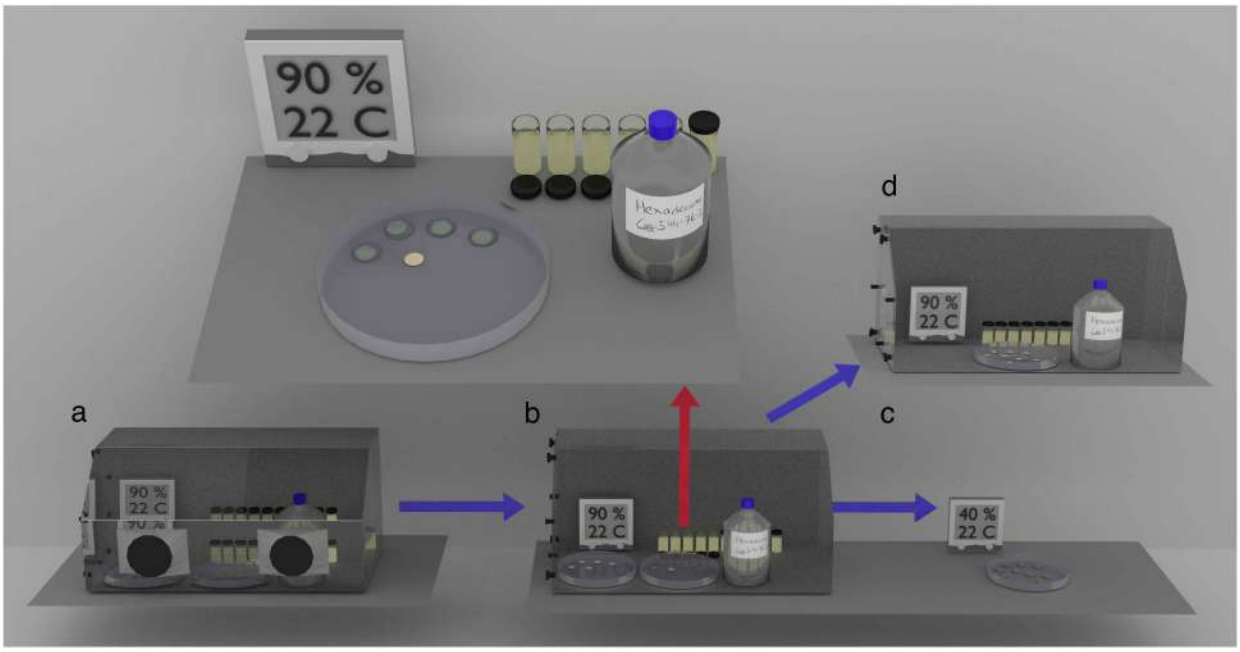

Figure 7.1: Schematic illustration of the preparation method of CNC films using different evaporation rates. (a) The sample vials are placed inside a glove box for the experiments with controlled drying at 22°C and 90% RH. (b) Two sets of CNC drops at different mass fractions and L/d are deposited on glass coverslips using a micropipette. One set of samples is covered with hexadecane. Simultaneously, a second series of samples are allowed to dry inside the box. The gloves are ommited in the illustration for simplicity. (c) After covering the CNC drops with hexadecane, the samples are taken out of the glove box to continue the drying process under room conditions. (d) The set of samples is left inside the box for evaporation at high RH. The red arrow indicates a magnified illustration of the inside of the glove box.

7.3 Influence of CNC mass fraction on the reflective colors of films dried at ambient conditions

I start this investigation by drop-casting unfractionated CNC suspensions (init-CNC) on coverslips with CNC mass fractions in the range from 2 wt% to 9 wt.%. The selected mass fraction range includes the isotropic phase (from 2 wt.% to 3 wt.%) and the two-phase regime (from 4 wt.% to 9 wt.%). Drops of 5 μL from each mass fraction were deposited on the glass substrate using a micropipette, and left untouched under ambient lab conditions (22°C and 40% RH). Photographs of the vials containing the equilibrated samples for this study are shown in Chapter 4, Figure 4.12 and the size distributions are presented in Figure 4.8.

I summarize the main results in Figure 7.2, presenting images of the dried films at different starting mass fractions in reflection mode (first column) and after the insertion of a quarter-wave plate, with the reflection and/or transmission of left-handed (second column) and right-handed circularly polarized light, CPL (third column). The height profile measurements of the dried films are presented on the right in Figure 7.2 for each starting mass fraction. All drying experiments were carried out in parallel and under the exact same ambient conditions. All water had evaporated after $t \approx 60$ min and the final films were characterized 24 h after drying.

From Figure 7.2, we observe a ring-like particle deposition as a function of particle mass fraction, showing an almost zero deposit height in the middle of the sample for films with lower mass fractions, as exhibited from the height profile measurements. In addition, reflected color changes radially from blue- to red-reflecting rings, from the center to the periphery of the films, and probably infrared light (IR) in the dark regions. From the profilometry data, the increased number of particles in the edge leads to an increase in height from ~ 20 μm for drops prepared with a starting mass fraction of 2 wt.% to ~ 70 μm for initial drops at 9 wt.%. The radial particle deposition can be explained by the evaporation–driven radial flow that carries the CNC rods outwards to the edge of the drop, collecting the particles at the periphery, near the contact line [27], resulting in a ring-deposition at the edge. This phenomenon introduced in Chapter 2 is known as the coffee-ring effect [23].

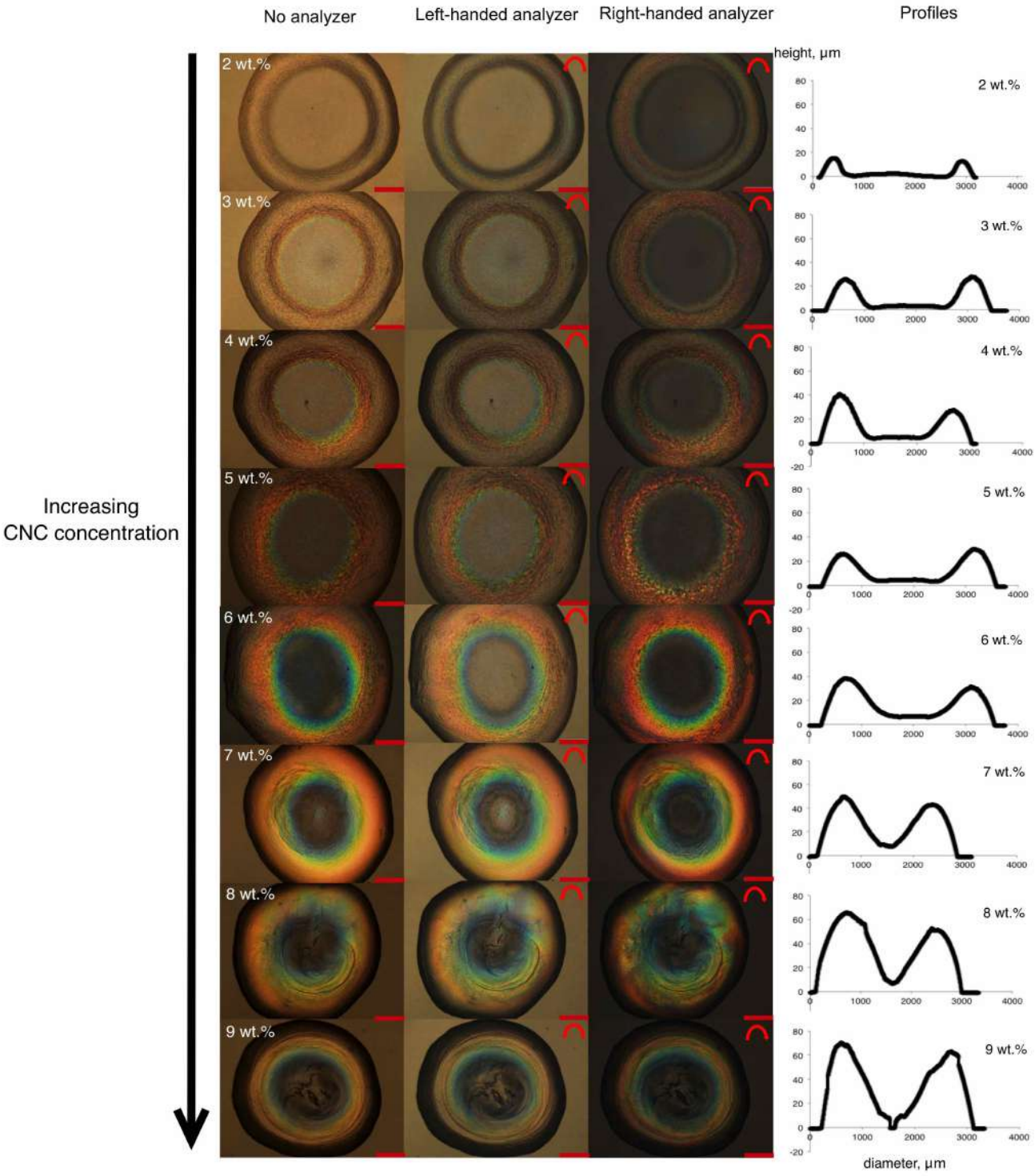

Figure 7.2: Reflection microscopy images of films dried at 22°C and 40% RH. Films were prepared from unfractionated rods (init-CNC) in a mass fraction range from 2 wt.% to 9 wt.%. For each image, the illumination is horizontally linearly polarized. In the first column, there is no analyzer. In the second and third columns, a $\lambda/4$ plate is used for checking the circular polarization. The height profile measurements are presented in the last column of images. Scale bars correspond to 500 μm.

The color fluctuations throughout the sample could demonstrate a large variation in pitch p [137], although the angle θ and the average refractive index $\bar{n}$ should be taken into account, according to Eq. 7.1 in the introduction of this chapter. Although a helical arrangement is found by scanning electron microscopy (SEM) investigations (Figure 7.3), the CNC rods probably have entered to a non-equilibrium gelled state before the helix has the time to fully equilibrate, resulting in films with the characteristic coffee-ring pattern and red-green coloration at the edge of the film [78,141,142]. On the contrary, the middle part of the film reflects blue as a consequence of the longer evaporation time and lower amount of particles in that particular location of the dried drop.

Figure 7.3 shows SEM images of the cross-sectional areas of a film prepared from an unfractionated CNC sample at a mass fraction of 5 wt.% under ambient conditions. Details of the sample preparation for the SEM characterization are presented in Chapter 2. Three different areas of the sample are exhibited: the center blue-colored region in Figure 7.3a, the red- colored area with high particle deposition in Figure 7.3b and the film periphery near the contact line in Figure 7.3c.

The three cross-sectional images exhibit areas with the characteristic periodic organization of materials with structural coloration, although the orientation of the helical arrangements are not completely normal to the substrate. The periodicity is clearly distorted in the thickest red-reflecting area of the film (Figure 7.3b), where the texture exhibits several dislocations across the structure with the helical axis varying with position. The pseudo-layers in the central blue-colored area of the film present a more ordered arrangement, although the periodic structure is tilted at the lower part of the sample (Figure 7.3a) compared to the areas near the edge (Figure 7.3c).

The irregular patterns observed in the SEM images can be related to variation in space of the helical pitch as well as to nonuniform orientation of the helical axis with respect to the glass substrate, probably as a consequence of the radial flow during the water evaporation. As mentioned in the introduction of this chapter, the angle θ in Eq. 7.1 is affected by the orientation of the helix axis, which could result in films with nonuniform colors upon evaporation of water. Previous studies have shown similar defects and the authors have agreed that the changes in volume, ionic strength and convective forces during evaporation have an impact on the organization of the rods [40, 143].

The analysis with a quarter-wave plate (from the second and third column in Figure 7.2) reveals that the reflective light is left-handed *and* right-handed circularly polarized. Saha and Davis [144] reported similar observations in CNC films characterized by selective reflectance using CPL. The authors suggested that the periodic modulation of the refractive indices can be

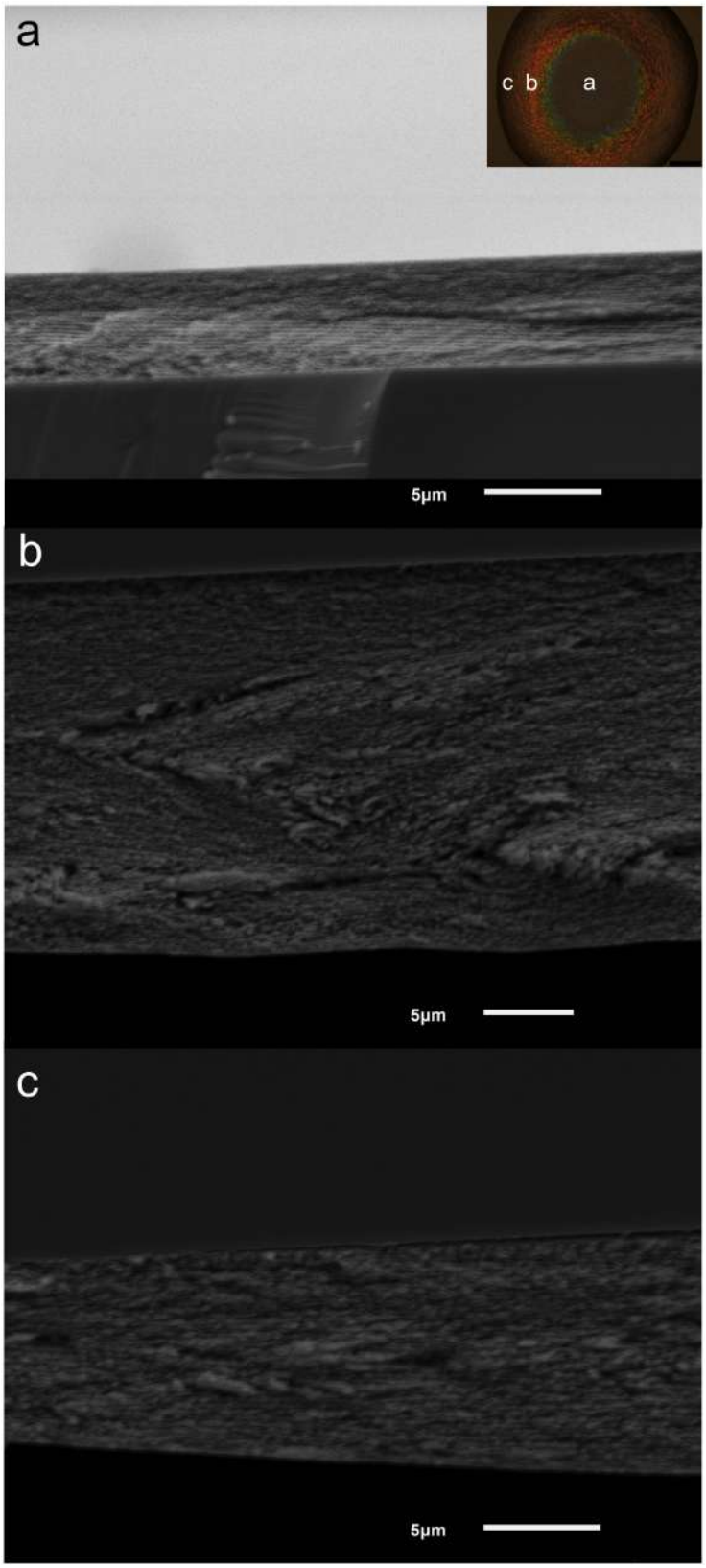

Figure 7.3: SEM images of the cross-sectional areas of a film of a 5 wt% unfractionated CNC suspension, dried at 22°C and 40%RH. The sequence of images presents the periodic structure of the film (a) at the blue-reflecting center, (b) red-reflecting area and (c) at the periphery. The inset corresponds to the reflection microscope image of the film with the letters indicating the position from which sample was cracked and the cross-section imaged.

changed by cholesteric microstructures with variable p in the film. From my results, I attribute this behavior to the non-uniformities that allow for lambda-half phase behavior at intermediate height, which can turn right-handed incoming light into left-handed. This means that the originally right-handed light is reflected by the left-handed structure, because the lambda-half plate changes the handedness. And since the reflected light also goes through the lambda-half plate, it is again right-handed when it is detected, hence it *appears* that the CNC reflects right-handed polarization. I will continue with the discussion of this topic at the end of this chapter.

I attempted to manually measure the pitch p from the SEM images in Figure 7.3, which corresponds to twice the distance between two consecutive pseudo-layers across the film. From the center to the periphery of the film, p shows variation in the range of 0.25 μm to 0.40 μm. By taking $\theta = 0$ and $\bar{n} = 1.6$ [145–148] in Eq. 7.1, we can obtain a rough estimation for λ_r, resulting in $\lambda_r \approx 400$ nm for the central blue-colored area and $\lambda_r \approx 650$ nm for the red-reflecting part of the film. Both values belong to the correct range of the wavelength of visible light, nevertheless, more analysis is needed for a complete conclusion of how the irregular pitch and the orientation of the helix axis can impact the optical reflective properties.

7.4 Influence of the rod size distribution on the optical response of dried films

The first time that the effect of the rod size on the final films was at least mentioned in a scientific publication, dates back to 1998. That year Revol and Grey [108], pioneers in the CNC field, reported that in films dried from CNC suspensions containing particles with longer average length, the color will be shifted towards the red, while for films containing shorter average length particles, the color will be shifted towards the blue. Unfortunately, these statements were only part of the discussion of the article, without the report of any data.

The films that I describe in the following were prepared by drop-casting CNC suspensions with two different aspect ratios L/d, both sets of samples obtained after the multiple separation of phases using the separatory funnel, protocol discussed in Chapter 4. CNC drops were dried under ambient lab conditions (22°C and 40% RH).

The sample vials between crossed-polarizers and the plots of the volume fraction Φ are presented in Figure 4.12. The size characterizations are shown in Figure 4.8 with an aspect ratio for $4i_f$-CNC of $L/d \approx 43$ and for $5a_f$-CNC of $L/d \approx 58$. I deposited 5 μL suspension drops with mass fraction in the range of 2 wt.% to 9 wt.%, on untreated glass coverslips.

Reflection microscopy images and height data of the dried drops for all the different mass fractions are presented in Figure 7.4 and in Figure 7.5, corresponding to the $5a_f$-CNC and $4i_f$-CNC films respectively. All drying experiments were carried out in parallel and under the same ambient conditions. All water had evaporated after $t \approx 60$ min and the resulting films were characterized 24 h after the drying process was completed.

The films exhibit radial color variation, although the selective reflection is stronger for the dried sample with high L/d, varying from blue to green and finally to red from the center to the edge of the films.

The height profile measurements of the dried drops evidence the existence of a clear ring-like deposit for both samples, with the periphery of the films containing most of the particles. From Fig. 7.4 and Fig. 7.5, films obtained from the two different L/d are quite different, both in terms of colors and morphology (i.e. profiles). In films made from rods with $L/d \approx 43$ at 8 wt.% and and 9 wt.%, the profiles present volcano-like shape, while for $L/d \approx 58$ the center of the film is very close to the surface. The latter means that radial flows are stronger for rods with higher L/d.

After fractionation, the increase in L/d enhanced liquid crystalline formation without affecting the mass fraction at which gelation occurs. Because of this, I am able to prepare films with high enough CNC mass fractions that form a fully liquid crystalline phase. Previous studies have suggested that the phase coexistance regime promotes random alignment of the helix due to the presence of tactoids in the sample, while films dried from fully cholesteric droplets would acquire a more uniform vertically aligned helix [137]. This approach suggests that drying a CNC suspension of very low concentration, located either in the completely isotropic regime [118, 132, 143] or near the end of the biphasic regime [135, 149–151] would result in films non-uniform in color, as largely reported in literature.

However, when drying drops containing rods with high L/d in the fully liquid crystalline regime, we observe that the films are not homogeneous in terms of color and handedness, since a clear variation in colors are visible throughout the film. Moreover, both right- and left-handed circularly polarized light are reflected. In fact, films prepared using higher mass fractions are even more irregular in shape (for example, the films prepared with 8 wt.% and 9 wt.% as starting mass fraction). The lack of colors compared to the films prepared with lower mass fractions suggest that the rods entered a gelled state before reaching values of p low enough to produce visible selective reflection after drying-induced compression.

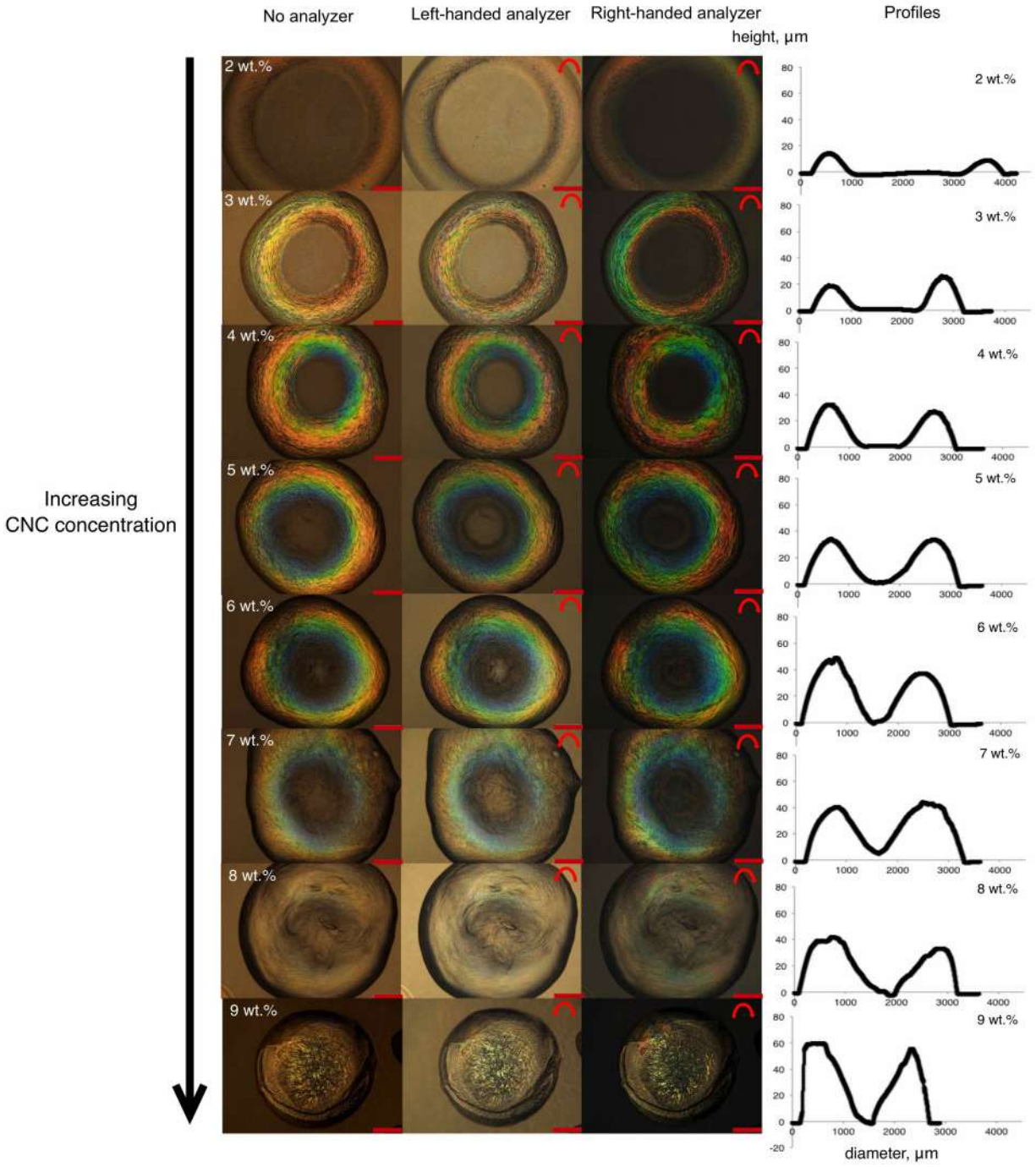

Figure 7.4: Reflection microscopy images of films dried at 22°C and 40% RH. Films were prepared using rods with $L/d \approx 58$ ($5a_f$-CNC) in a mass fraction range from 2 wt.% to 9 wt.% in a mass fraction range from 2 wt.% to 9 wt.%. For each image, the illumination is horizontally linearly polarized. In the first column, there is no analyzer. In the second and third columns, a $\lambda/4$ plate is used for checking the circular polarization. The height profile measurements are presented in the last column of images. Scale bars correspond to 500 μm.

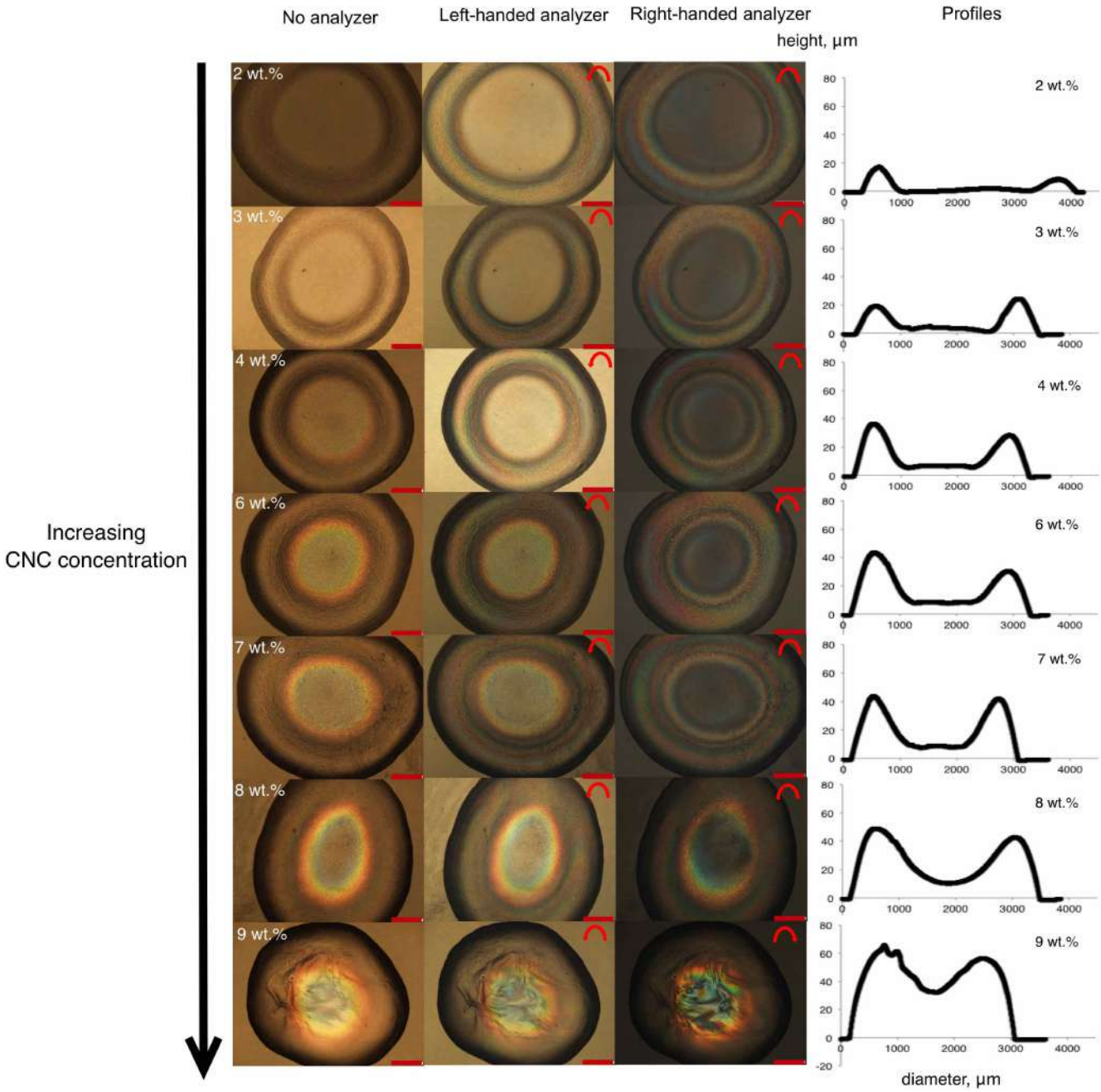

Figure 7.5: Reflection microscopy images of films dried at 22°C and 40% RH. Films were prepared using rods with $L/d \approx 43$ ($4i_f$-CNC) in a mass fraction range from 2 wt.% to 9 wt.% in a mass fraction range from 2 wt.% to 9 wt.%. For each image, the illumination is horizontally linearly polarized. In the first column, there is no analyzer. In the second and third columns, a $\lambda/4$ plate is used for checking the circular polarization. The height profile measurements are presented in the last column of images. Scale bars correspond to 500 μm.

It is important to highlight that the comparison between studies is not trivial. The preparation of the CNCs has a huge impact on the properties of the particles in both aqueous suspension and final films. As an example, Beck and co-authors [118] have reported that sonication (prior to film casting) increases p, moving the reflection band of the final film to longer wavelength. I will present in the next section my results of the effect of evaporation rate on the reflected colors, the importance to characterize the CNC suspensions and report the drying conditions is crucial in order to compare results obtained by different authors.

Figure 7.6 shows images captured with polarizing microscopy for three films prepared with the unfractionated CNC (Figure 7.6a), $4i_f$-CNC film (Figure 7.6b) and $5a_f$-CNC (Figure 7.6c) with the same starting mass fraction and dried in ambient lab conditions. Domains are observed in the three different films. However, for the dried drop from the low L/d suspension, the multidomains are smaller compared to the other two samples, and they are visible throughout the entire film. If we go back to Chapter 6, specifically to Figure 4.15, the presence of tactoids after 2 years in capillaries filled with short-rod fractions reveal that the tactoids have reached a kinetic arrested state. I can thus conclude that those domains that are observed in the final films resulted from tactoids that never merged, regardless of the drying conditions.

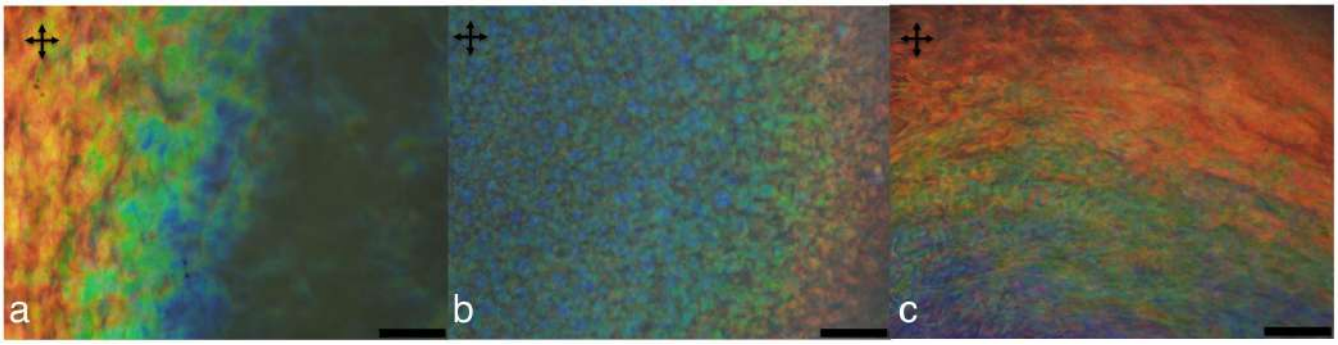

Figure 7.6: Films dried from 6 wt.% CNC suspensions showing a radial color variation. a) Photo showing a film from an unfractionated CNC suspension. b) Photo of a film prepared from rods with $L/d \approx 43$ ($4i_f$-CNC) with a polydomain pattern from the center to the edge of the sample. c) Photo of a film containing rods with $L/d \approx 58$ ($5a_f$-CNC). Each image was taken between crossed polarizers in reflection mode. Scale bars correspond to 500 μm.

7.5 Effect of evaporation rate on final dried films

7.5.1 Drop-drying inside a glove box

I continue the study by extending the drying time of the CNC drops using a glove box and compare the obtained results to the characteristic ring deposits discussed in the previous sections. More details of the drying process have been illustrated in Figure 7.1.

Microscope images and height profile measurements of the dried films for the three different CNC samples are presented in Figure 7.7, Figure 7.8 and Figure 7.9, corresponding to films formed from unfractionated CNCs, $5a_f$-CNC ($L/d \approx 58$) and $4i_f$-CNC ($L/d \approx 43$), respectively. The drying of each set of samples was carried out simultaneously inside the glove box, with an initial relative humidity RH of 90% and a temperature $T = 22°C$. The films remained inside the glove box for a time $t \approx 7$ days. After this period, the films were removed from the box and characterized after 24 h.

For the three different sets of samples, the drops of more dilute suspensions yielded thin films with diameters of ~ 3.5 mm and a maximum height of ~ 20 μm for CNC mass fractions in the range of 2 wt.% to 4 wt.%. The thin film at low rod mass fraction is a result of the small amount of particles, distributed more evenly across the film compared to the corresponding films that were dried fast at low humidity. A clear evolution of increasing film thickness with increasing rod mass fraction is observed, with all height profiles showing dome-like shapes. A dome-like profile can be understood as the projection of particle distribution across the drop; in other words, a dome shape is a direct consequence of the initial shape of the drop, which is a spherical cap [152, 153].

The greatest height of these films varies from ~ 30 μm to ~ 80 μm for CNC mass fractions ranging from 5 wt.% to 8 wt.%. These profile patterns indicate that there was no significant radial transport of CNC rods during drying at this slow rate of evaporation. Probably the evaporation-driven flows have very small impact on the deposition process of suspended CNC rods.

Interestingly, the dome-like depositions of the CNC rods is not the only reason for films reflecting more homogeneous colors. In fact, some radial color variation can be observed for films prepared from unfractionated CNC suspensions (Figure 7.7) showing the characteristic polydomain mosaic patterns reported in previous studies [137, 144]. For this set of films, the reflecting colors vary depending on the CNC mass fraction, changing from green-blue multidomains domains to films exhibiting red-green areas for higher initial mass fractions.

Films consisting of rods from fractionated CNC samples reveal the impact of L/d on the color

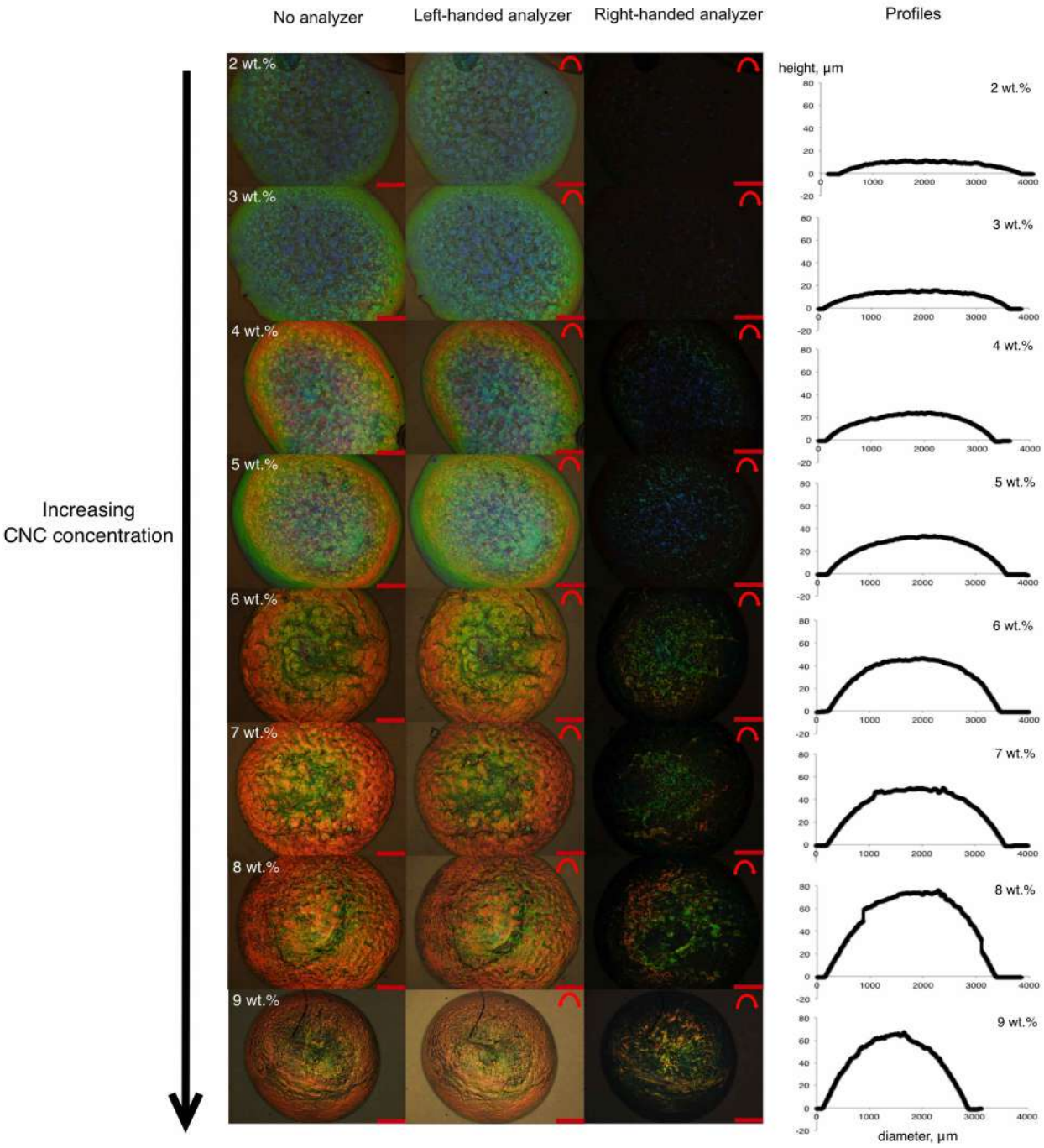

Figure 7.7: Reflection microscopy images of films dried in a controlled atmosphere glove box at 22°C and 90% RH. Films were prepared using unfractionated samples (init-CNC) in a mass fraction range from 2 wt.% to 9 wt.%. For each image, the illumination is horizontally linearly polarized. In the first column, there is no analyzer. In the second and third columns, a $\lambda/4$ plate is used for checking the circular polarization. The height profile measurements are presented in the last column of images. Scale bars correspond to 500 μm.

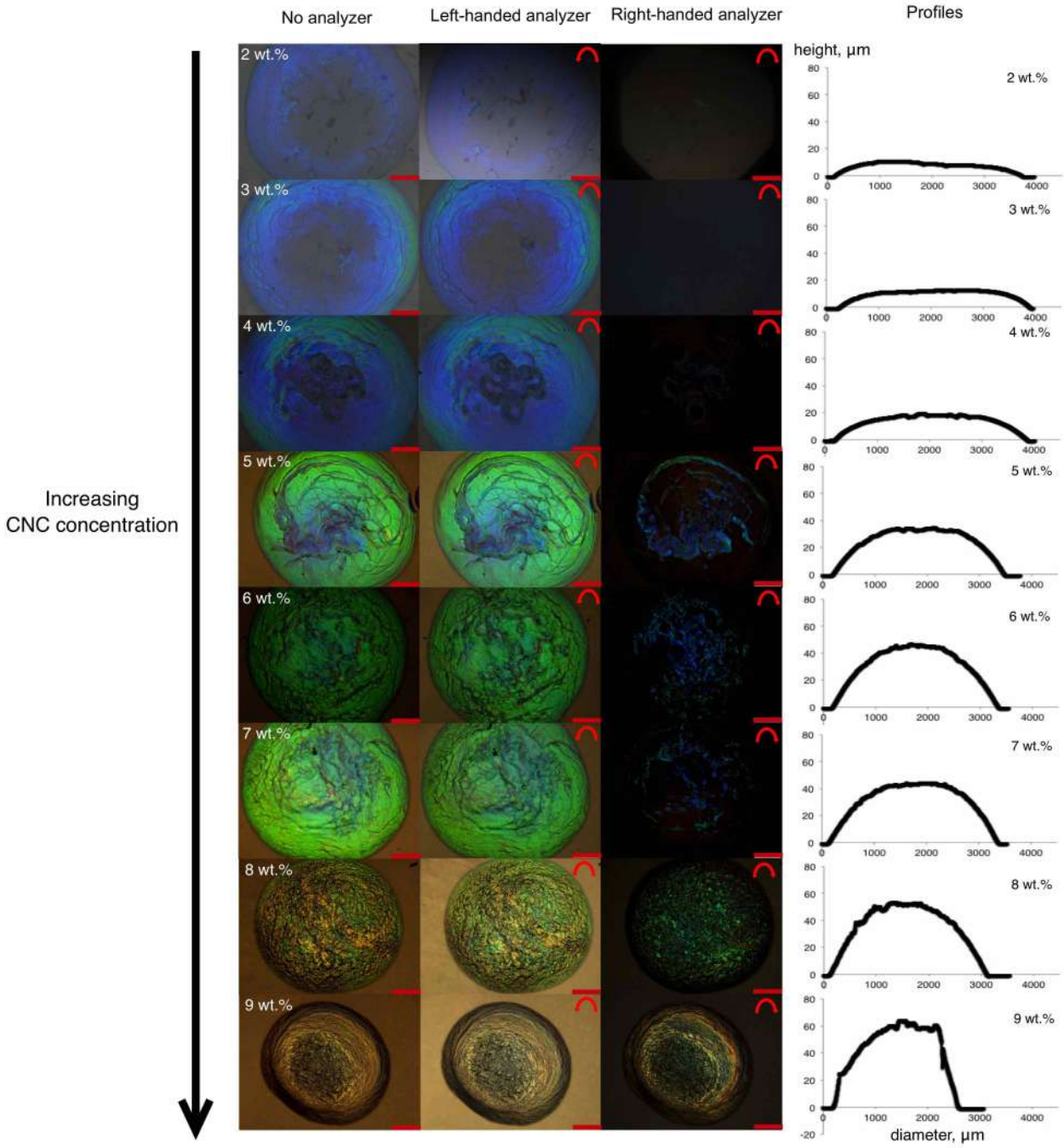

Figure 7.8: Reflection microscopy images of films dried in a controlled atmosphere glove box at 22°C and 90% RH. Films contain rods with $L/d \approx 58$ ($5a_f$-CNC) in a mass fraction range from 2 wt.% to 9 wt.%. For each image, the illumination is horizontally linearly polarized. In the first column, there is no analyzer. In the second and third columns, a $\lambda/4$ plate is used for checking the circular polarization. The height profile measurements are presented in the last column of images. Scale bars correspond to 500 μm.

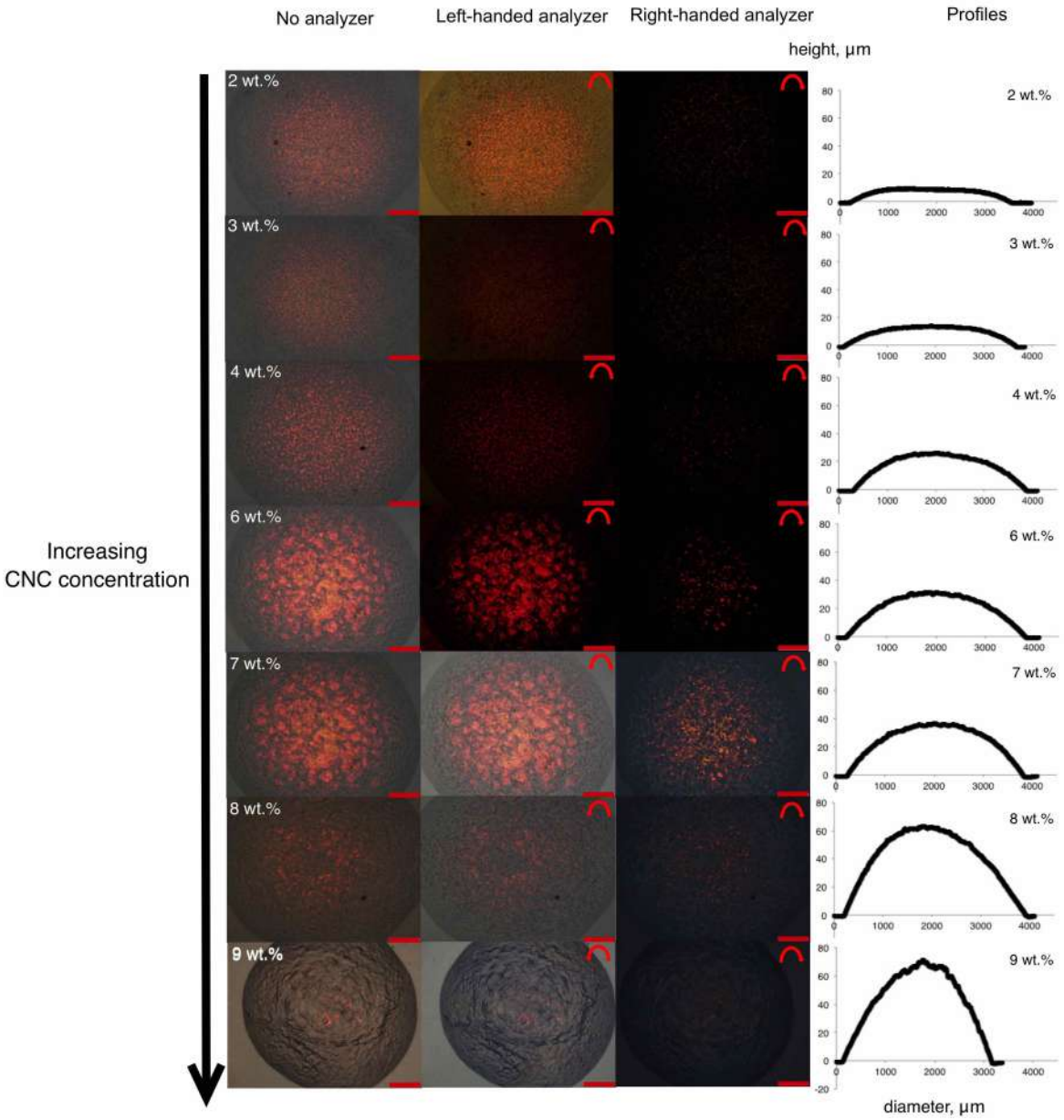

Figure 7.9: Reflection microscopy images of films dried in a controlled atmosphere glove box at 22°C and 90% RH. Films contain rods with $L/d \approx 43$ ($4i_f$-CNC) in a mass fraction range from 2 wt.% to 9 wt.%. For each image, the illumination is horizontally linearly polarized. In the first column, there is no analyzer. In the second and third columns, a $\lambda/4$ plate is used for checking the circular polarization. The height profile measurements are presented in the last column of images. Scale bars correspond to 500 μm.

formation. Figure 7.8 shows microscopic images and height profiles of films formed from $5a_f$-CNC sample with rods of $L/d \approx 58$ and with different CNC mass fractions. The films exhibit more homogenous colors compared to the films from unfractionated rods. They reflect intense blue if prepared from low CNC mass fractions (from 2 wt.% to 4 wt.%) whereas green areas dominate across the film for particle mass fractions between 5 wt.% and 7 wt.%.

Reflection microscope images of the films using rods with $L/d \approx 43$ ($4i_f$-CNC) are presented in Figure 7.9. Polarizing microscope images after the insertion of a quarter-wave plate, probing the reflection of left-handed circular polarized light (CPL), are shown in the second column and the corresponding images with the analyzer set to probe right-handed CPL in the third column. The height profile measurements of the dried films are presented in last column in Figure 7.9. They all exhibit strong red-reflecting color with the presence of domains across the samples.

From the results presented above, we can conclude that slow drying suppresses the coffee-ring effect regardless of the rod L/d in the original suspension, resulting in more uniform films compared to the samples dried under lab ambient conditions. Two explanations for this behavior can be considered. First, this type of dome-like deposits could occur when gelation is reached comparatively quickly after the creation of the drop, with water evaporating faster than the rate of particle diffusive motion [154]. This situation was certainly not present in the earlier experiments, where ring-shape deposits were formed by drop-casting CNC suspensions under ambient conditions, showing that there is significant CNC rod translation within the drops before gelation sets in, even for high particle mass fraction. The second reason could be the negligible radial capillary flow due to the slow water loss across the sample surface, which results in diffusion dominating over capillary flow [155]. This restriction in radial flows permits that neighboring domains are able to merge and later form a single and uniform domain [104].

The color variation between films containing rods with different L/d can be understood in terms of w_0 and w_1, mass fractions thresholds reported in Chapter 5. During evaporation of water from a starting CNC suspension w, must pass through a mass fraction region where spontaneous formation of a chiral nematic phase is entropically favor, according to the Onsager model [142]. The chiral structure formed will remain later on in the dry state, once gelation sets in at w_g. I concluded in Chapter 5 that L/d either promotes LC formation for rods with high L/d, shifting w_0 and w_1 towards lower w compared to the unfractionated sample. Whereas w_0 and w_1 are shifted towards much higher w for rods with high L/d. However, w_g is unaffected by L/d. Because of this, the short rods have much less time available to equilibrate before being trapped in a gel state (at w_g), since it only forms a LC phase once w is so high that gelation sets in first ($w_1 > w_g$). On the contrary, the low values of w_0 and w_1 for the long rods permit that the CNC suspensions equilibrate much earlier compared to the unfractionated sample. This

results in uniform films if the drying conditions are slow enough, as I presented in the previous experiments.

Using the explanation from above, the effect of w on the color variation is also a result of how much time the sample has available in order to equilibrate. If a CNC drop at high w is deposited on the substrate, the suspension will have less time to equilibrate before gelation sets in, compared to CNC suspensions with low starting w. If it is assumed that gelation prevents the further decrease in p expected for higher w, then the final wavelength of the film should move to higher values, with red-shift of the samples with increasing w, as we observed in Figure 7.7 and in Figure 7.8.

7.5.2 Drop drying using immiscible oil

The suppression of water evaporation from small volumes of samples by using immiscible oils has been reported for a variety type of materials [156, 157]. Following the procedure recently reported by Zhao *et al.* [104], I attempted to extend the drying time of the CNC drops by covering the initial samples with hexadecane at the beginning of the process until the final films are formed.

I deposited 10 μL drops using a micropipette on untreated glass coverslips. The experiments were carried out inside a glove box which was maintained at 22°C and 90% HR to avoid water loss during the process. I dried CNC drops from the three different samples (unfractionated CNC, $5a_f$-CNC and $4i_f$-CNC) at initial CNC mass fractions of 3 wt.% and 6 wt.%.

Reflection microscopic images of the dried films from initial CNC suspensions of 3 wt.% are presented in Figure 7.10 and films with initial CNC mass fraction of 6 wt.% are shown in Figure 7.11. Left- and right-handed CPL images are presented for both sets of films.

The unfractionated rods and CNCs with high aspect ratio from initial suspensions of 3 wt.% form films with homogeneous and intense blue-reflecting color throughout the complete sample. For both films, only left-handed CPL is reflected, a clear indication of well-aligned and highly-ordered film [107,158]. On the contrary, the film from the short-rod fraction present red domains across the sample, and some right-handed CPL is reflected.

When increasing the mass fraction to 6 wt.%, (Figure 7.11), the blue coloration continues but only for the high aspect ratio film, which reflects left-handed CPL. For the case of the film from the init-CNC and from rods with low aspect ratio, the multidomain pattern are observed, both reflecting red-green colors and both circular polarizations.

Figure 7.12 shows SEM images of the cross-section of films prepared with 3 wt.% with low L/d

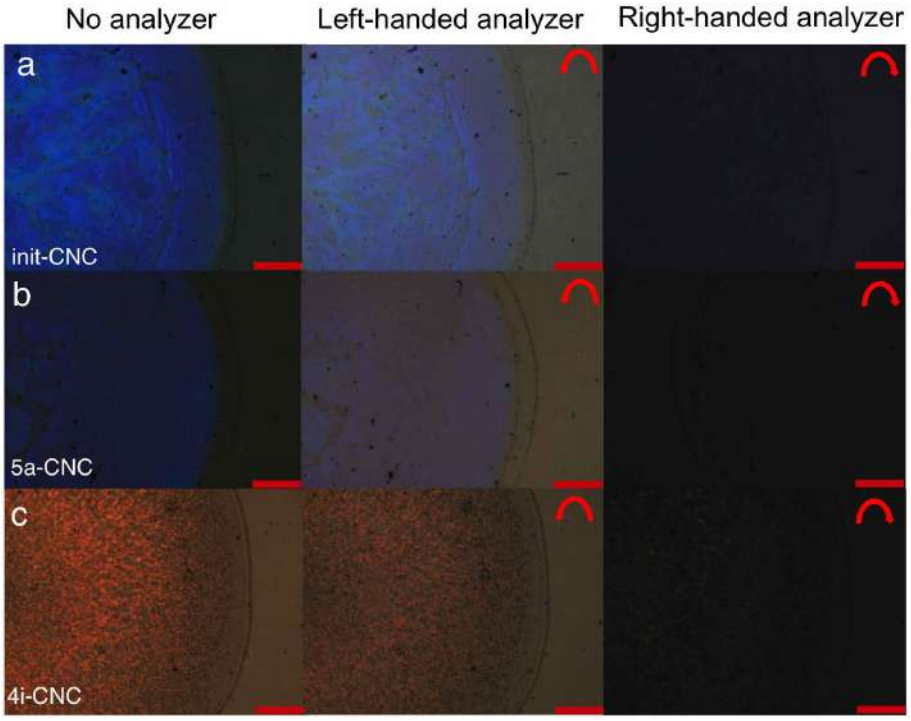

Figure 7.10: Reflection microscopy images of CNC films slowly dried under hexadecane oil and prepared with an starting CNC suspension of 3 wt.%. (a) Film formed with unfractionated sample (init-CNC), (b) high L/d rods and (c) low L/d rods. For each image, the illumination is horizontally linearly polarized. In the first column, there is no analyzer. In the second and third columns, a $\lambda/4$ plate is used for checking the circular polarization. Scale bars correspond to 500 μm.

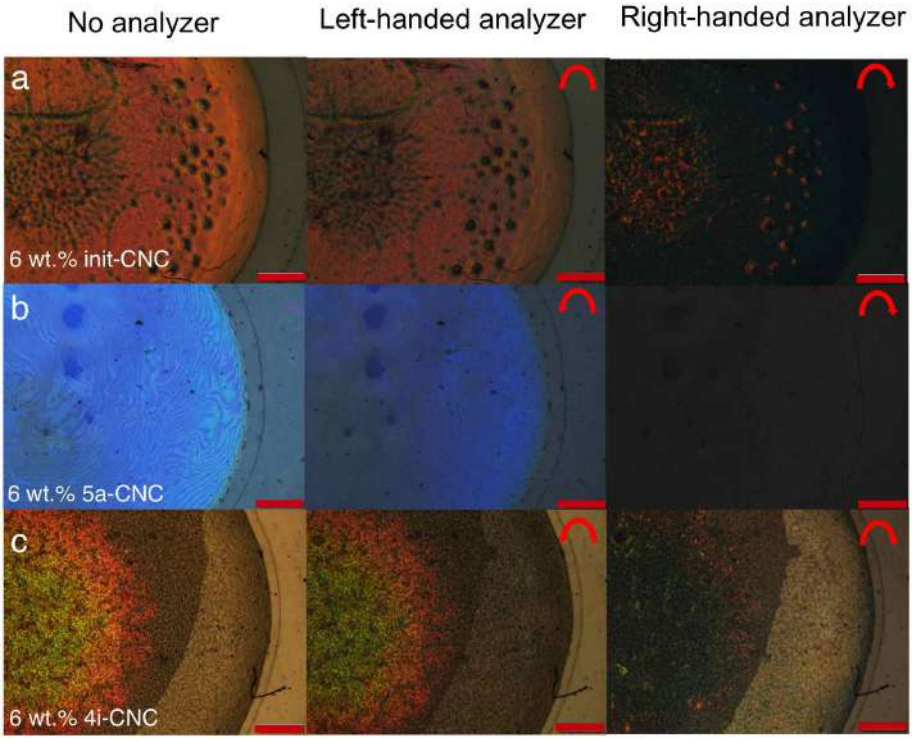

Figure 7.11: Reflection microscopy images of CNC films slowly dried under hexadecane oil and prepared with an starting CNC suspension of 6 wt.%. (a) Film formed with unfractionated sample (init-CNC), (b) with high L/d rods ($5a_f$-CNC) and (c) with low L/d rods. For each image, the illumination is horizontally linearly polarized. In the first column, there is no analyzer. In the second and third columns, a $\lambda/4$ plate is used for checking the circular polarization. Scale bars correspond to 500 μm.

rods (a) and high L/d (b), with slow drying. The two images were captured using the same magnification.

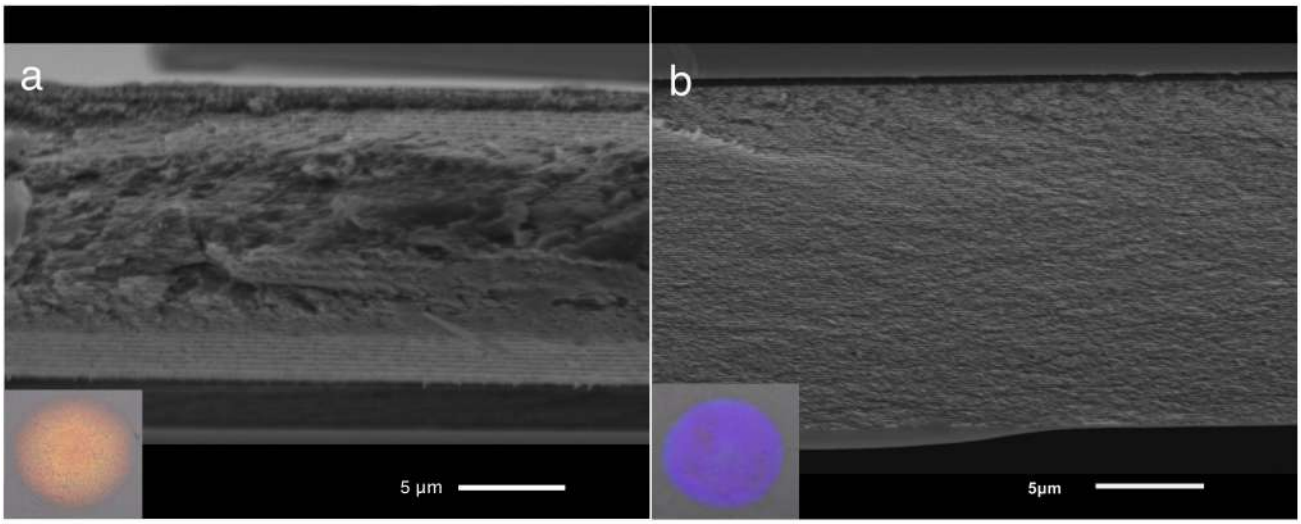

Figure 7.12: SEM images of the cross-sectional areas of two films formed with starting CNC sample at 3 wt.% and dried using hexadecane. a) Film containing rods with low aspect ratio shows larger pitch and a non-uniform periodic structure. b) Film containing rods with high aspect ratio exhibits significantly shorter and uniform pitch and more uniform direction of periodicity compared to the periodicity of films formed with low aspect ratio rods. Both insets present microscopic images of the corresponding films captured at an angle of $\sim 30°$.

In both images, we observe the typical periodicity of the rods that is responsible of the structured coloration of the samples, with half the pitch p as the distance between two consecutive stripes. The images were obtained roughly at the center of the film.

We can visualize the consequences of the early gelation in the films made from low aspect ratio rods. The cross-section of this red film (Figure 7.12a) presents a sandwich-like organization, with periodic structures at the top interface (close to the oil during drying) and at the bottom interface (close to the glass substrate). A non-uniform cross-sectional area is observed between the two interfaces. As discussed above, this region without a uniform standing helix will show birefringence, thus being able to act as a phase plate. This explains why the red reflecting films show reflection of both left- and right-handed CPL, because the intermediate disordered region can act close to a lambda/2 plate, changing right-handed CPL into left-handed CPL on the way down, and back on the way up for the light reflected from the bottom region with uniform standing helix. On the contrary, the film formed with rods of $L/d \approx 58$ (7.12b) presents an organized and periodic structure continuously from the top to the bottom of the sample with constant pitch p. Values of p (measured as twice the distance between two consecutive stripes)

for the red film is in the range of 0.4 μm and 0.3 μm for the blue-reflecting sample.

By considering $\theta = 0$ and $\bar{n} = 1.6$ [145] in Eq. 7.1, I can obtain a rough estimation for λ_r, resulting in $\lambda_r \approx 400$ nm for the central blue-colored area and $\lambda_r \approx 650$ nm for the red-reflecting part of the film. Both values belong to the range of the wavelength of visible light and coincide with the colors observed by naked eye. Figure 7.13 exhibits the UV-visible transmittance spectra of both films prepared from the fractionated CNCs, measured with a spectrophotometer.

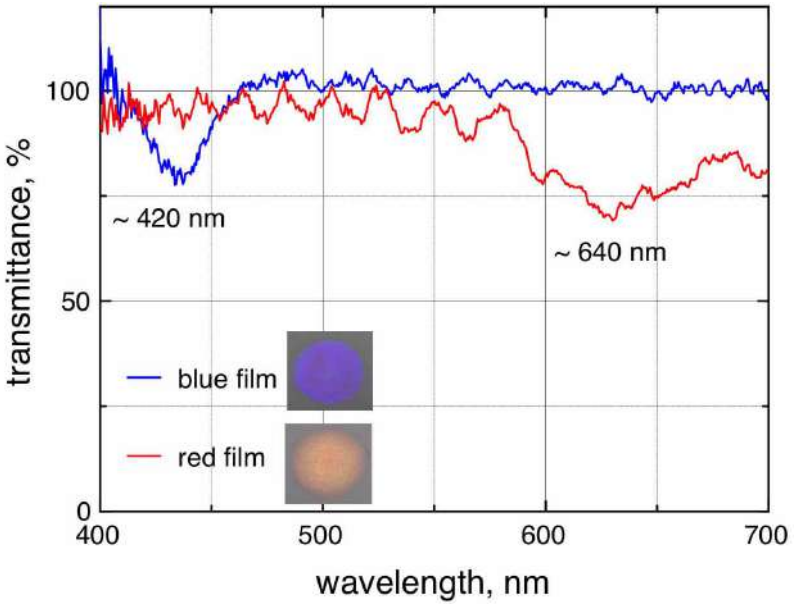

Figure 7.13: Transmittance spectra in the region of visible light for solid films prepared from low L/d (blue curve) and from high L/d (red curve). The insets present the images of the corresponding the films.

Here I use the minimum transmittance as an indicator of the maximum reflection wavelength in the CNC films; the reflected light appears as an absorbance peak in transmission mode [108,135]. In other words, the transmission dip corresponds to the light that has been selectively reflected by the film, and therefore does not reach the detector of the spectrophotometer. In the region within the band gap, circularly polarized light with the same handedness than the helical structure of the sample theoretically should exhibit 100 % reflectivity [40, 159]. Therefore, the reflectivity for unpolarized light, which was used in these experiments, is expected to be 50 %, since half of the light is reflected away. This is not the case for both films, for which the transmitance is less than 50 %, probably an indication of some defects in the samples. From Figure 7.13 the spectrum of the blue film exhibits a central peak $\lambda_r \approx 420$ nm, more or less in agreement with the value of pitch determined from the SEM images. The spectrum of the red film is much less smooth, which can be interpreted as an indication of the spread in helix orientations and/or pitch, as we observe from the cross section image in Figure 7.12a. If we consider a central peak of $\lambda_r \approx 640$ nm, this value is close to the pitch measurements from the SEM image.

Nevertheless, more analysis is needed for a complete conclusion of how the irregular pitch in the film prepared with short rods as well as the orientation of the helix axis, might impact the optical reflective properties.

7.6 Summary

The CNC helical structure of the liquid crystal phase can be preserved in dried films upon water evaporation. If the helix pitch of the final dried sample is in the range of the visible wavelengths, the films will exhibit structural colors. The results in this chapter reveal that the relative humidity is one of the most critical parameters in the preparation of solid films. The reason for this is that the fast drying promotes radial transportation of the particles towards the edge of the drop, according to the famous "coffee-ring effect", whereas slow drying suppresses this effect. The slow drying can also be accomplished by covering the initial drop with hexadecane, which considerably slows down drying. If, in addition, films are prepared from fractionated samples, we can get absolutely homogeneous color of the film, reflecting only one circular polarizarion, as should be the case for CNCs. Films prepared from a suspension of long aspect radio rods result in a well-ordered helical structure and acquires a deep blue reflection across the film, whereas films from short rods tend to be red. We believe that the latter is due to the larger counterion concentration in the suspension with low aspect ratio rods. Since more CNC particles are needed to promote a liquid crystal phase, the system gets so close to gelation already at the onset of liquid crystal formation. Because of this, the helix never has the time to reach its equilibrium pitch before gelation sets in, which leads to poorly developed order.

Chapter 8

Conclusions and outlook

The study elaborated in this thesis reports a wide spectrum of experiments, from the initial stages of the self-organization of CNC rods in aqueous suspensions to the controlled preparation of solid iridescent films by evaporating the water.

One of the main goals and achievements described in this work is the successful segregation of CNC suspensions into different fractions. In these fractions, CNC rods with distinct geometrical morphology are accumulated, allowing to influence the onset of the liquid crystal formation. For CNC rods having a high aspect ratio, the onset of the liquid crystal formation starts at much lower mass fraction compared to rods with low aspect ratio. For the fractionation of CNC rods in suspension, being a mixture of CNC rods with different aspect ratios, the equilibrium phase coexistence of the isotropic and chiral nematic phase close to the onset of the liquid crystal formation is crucial. The evaluation of the numerous experiments allowed the establishment of a deep understanding of the physical chemistry that is fundamental to the separation process and liquid crystal formation of rod-like systems. The protocol that derived from this work reveals an effective way to collect pristine CNC rod fractions.

Although the size segregation of a highly disperse CNC suspension occurs regardless of the overall concentration of the CNC sample within the two-phase regime, the longest rods will populate the fraction just above $\Phi = 0$, while the shortest CNCs will be located in the fraction just below the end of the coexistence phases. This allows to fractionate pristine CNCs in a fast way, without the need of repeated separations of liquid crystalline and isotropic fractions.

The fractionated samples were used in a very smart way, and by the addition of calculated amounts of salt, it was proved that the key parameter that induces gelation is neither the mass of rods nor the volume fraction, as initially hypothesized, but the counterion concentration: a macroscopic gel is formed once a critical ion concentration is reached, regardless of rod aspect ratio and of concentration. Interestingly, it has been found indications that the individual rods

form end-to-end aggregation when the overall mass fraction is approaching the onset of gelation, as evidenced from the AFM images and further analysis as well as the anisotropy observed in the gelled samples, even for the fully isotropic suspensions that are far from the onset of liquid crystal formation.

Because the mass fraction for liquid crystal formation is much lower when working with the long rods, the range of the equilibrium liquid crystal phase is extended. Using the long-rod fraction and by performing systematic ion exchange experiments, we can conclude that the helix pitch of CNC suspensions is neither *directly* a function of CNC content and nor affected by the aspect ratio of the particles within the range that was investigated in this thesis.

We conclude that it may be the counterion effect on the pitch due to the effect on the phase diagram and on the rod volume fraction in the system that promotes the decrease in pitch at increasing CNC mass fraction. This new perspective can be understood in terms of the *overall* particle volume fraction that increases, enhancing the effect of the electrostatic repulsion on the local director, promoting a stronger twist and thus, a shorter pitch.

Using again the fractionated samples, films were obtained after water evaporation under controlled drying conditions, starting from samples with completely isotropic phase to the fully liquid crystalline suspensions. We conclude that the slow drying of CNC suspensions with high aspect ratio rods strongly impact the final color formation, due to their ability to develop fully chiral nematic phases at a mass fraction far from the onset of gelation. This results in uniform color of the film and with only one circular polarization, as should be the case for this type of nanorods.

In terms of future experiments, the effect of sonication on the final behavior of CNC is still a mystery. Although there exist studies where sonication is used for tuning the pitch in CNC aqueous suspensions and final dried films, there are not a conclusive explanations about what is actually happening when a CNC sample is sonicated, or even simpler, is it necessary to sonicate the sample? instead, maybe centrifugation or other mechanism could be used.

A full elucidation of the origin of the end-to-end aggregation phenomenon is outside the scope of this experimental thesis, but it leaves a stimulating challenge for theoreticians to address.

Bibliography

[1] A. Hirai, O. Inui, F. Horii, and M. Tsuji, "Phase separation behavior in aqueous suspensions of bacterial cellulose nanocrystals prepared by sulfuric acid treatment.," *Langmuir : the ACS journal of surfaces and colloids*, vol. 25, no. 1, pp. 497–502, 2009.

[2] C. Honorato-Rios, C. Lehr, C. Schütz, R. Sanctuary, M. A. Osipov, J. Baller, and J. P. Lagerwall, "Fractionation of cellulose nanocrystals: enhancing liquid crystal ordering without promoting gelation," *NPG Asia Materials*, pp. 1–11, 2018.

[3] J. N. Israelachvili, *Intermolecular and surface forces*, vol. 151. 2015.

[4] J. P. F. Lagerwall, C. Schütz, M. Salajkova, J. Noh, J. Hyun Park, G. Scalia, and L. Bergström, "Cellulose nanocrystal-based materials: from liquid crystal self-assembly and glass formation to multifunctional thin films," *NPG Asia Materials*, vol. 6, no. 1, p. e80, 2014.

[5] P. Christian, F. Von Der Kammer, M. Baalousha, and T. Hofmann, "Nanoparticles: Structure, properties, preparation and behaviour in environmental media," *Ecotoxicology*, vol. 17, no. 5, pp. 326–343, 2008.

[6] C. Honorato-rios, J. Bruckner, C. Schutz, S. Wagner, Z. Tosheva, L. Bergstrom, and J. P. F. Lagerwall, *Cholesteric liquid crystal formation in suspensions of cellulose nanocrystals*. World Scientific, 2016.

[7] I. Dierking, "Chiral liquid crystals: Structures, phases, effects," *Symmetry*, vol. 6, no. 2, pp. 444–472, 2014.

[8] H. C. R. Pasteur, L., "Mémoire sur la relation qui peut exister entre la forme cristalline et la composition chimique, et sur la cause de la polarisation rotatoire," *Comptes rendus hebdomadaires des séances de lAcadémie des Sciences*, no. 26, p. 535, 1848.

[9] R. Jones, "Soft Condensed Matter," in *Soft Consended Matter*, ch. 7, p. 112, 2002.

[10] J. Noh, *Tuning Self-Assembly in Liquid Crystal shells: from Interfacial- to Polymer-stabilizatio*. PhD thesis, University of Luxembourg, 2018.

[11] I. Dierking, *Textures of Liquid Crystals*, vol. 124. Weinheim, FRG: Wiley-VCH Verlag GmbH & Co. KGaA, 5 2003.

[12] J. P. F. Lagerwall, "A phenomenological introduction to liquid crystals and colloids," pp. 11–93, 2016.

[13] M. Mitov, "Cholesteric liquid crystals with a broad light reflection band," *Advanced Materials*, vol. 24, no. 47, pp. 6260–6276, 2012.

[14] M. Mitov, "Cholesteric liquid crystals in living matter," *Soft Matter*, vol. 13, no. 23, pp. 4176–4209, 2017.

[15] V. Sharma, M. Crne, J. O. Park, and M. Srinivasarao, "Structural origin of circularly polarized iridescence in jeweled beetles," *Science*, vol. 325, no. 5939, pp. 449–451, 2009.

[16] S. Vignolini, P. J. Rudall, A. V. Rowland, A. Reed, E. Moyroud, R. B. Faden, J. J. Baumberg, B. J. Glover, and U. Steiner, "Pointillist structural color in Pollia fruit," *Proceedings of the National Academy of Sciences*, vol. 109, no. 39, pp. 15712–15715, 2012.

[17] L. Onsager, "the Effects of Shape on the Interaction of Colloidal Particles," *Annals of the New York Academy of Sciences*, vol. 51, no. 4, pp. 627–659, 1949.

[18] Georgios M. Kontogeorgis Søren Kiil, *Introduction to Applied Colloid and Surface Chemistry*. 1 ed., 2016.

[19] J. C. Berg, "Electrical Properties of Interfaces," in *An Introduction to Interfaces and Colloids*, ch. 6, pp. 455–482, London: World Scientific, 2010.

[20] R. J. Hunt and W. P. Johnson, "Pathogen transport in groundwater systems: contrasts with traditional solute transportTransport de pathogènes dans les systèmes aquifères: contrastes avec le transports traditionnel de solutésTransporte de patógenos en sistemas de agua subterránea: contra," *Hydrogeology Journal*, vol. 25, no. 4, pp. 921–930, 2017.

[21] K. S. Kontogeorgis, Georgios M., *Introduction to applied colloid and surface chemistry*. first edit ed., 2016.

[22] D. Z. Ruoyang Chen, Liyuan Zhang and W. Shen, "Wetting and Drying of Colloidal Droplets: Physics and Pattern Formation," *Intech open*, vol. 2, p. 64, 2018.

[23] R. D. Deegan, O. Bakajin, T. F. Dupont, G. Huber, S. R. Nagel, and T. A. Witten, "Capillary flow as the cause of ring stains from dried liquid drops," *Nature*, vol. 389, no. 6653, pp. 827–829, 1997.

[24] D. Mampallil and H. B. Eral, "A review on suppression and utilization of the coffee-ring effect," *Advances in Colloid and Interface Science*, vol. 252, pp. 38–54, 2018.

[25] P. J. Yunker, T. Still, M. A. Lohr, and A. G. Yodh, "Suppression of the coffee-ring effect by shape-dependent capillary interactions," *Nature*, vol. 476, no. 7360, pp. 308–311, 2011.

[26] R. Chen, L. Zhang, D. Zang, and W. Shen, "Blood drop patterns: Formation and applications," *Advances in Colloid and Interface Science*, vol. 231, pp. 1–14, 2016.

[27] M. Anyfantakis, D. Baigl, and B. P. Binks, "Evaporation of Drops Containing Silica Nanoparticles of Varying Hydrophobicities: Exploiting Particle-Particle Interactions for Additive-Free Tunable Deposit Morphology," *Langmuir*, vol. 33, no. 20, pp. 5025–5036, 2017.

[28] L. Brinchi, F. Cotana, E. Fortunati, and J. M. Kenny, "Production of nanocrystalline cellulose from lignocellulosic biomass: Technology and applications," *Carbohydrate Polymers*, vol. 94, no. 1, pp. 154–169, 2013.

[29] Y. L. Hsieh, "Cellulose nanocrystals and self-assembled nanostructures from cotton, rice straw and grape skin: A source perspective," *Journal of Materials Science*, vol. 48, no. 22, pp. 7837–7846, 2013.

[30] R. H. Marchessault, F. F. Morehead, and N. M. Walter, "Liquid Crystals Systems from Fibrillar Polysaccharides," *Nature*, vol. 184, pp. 632–633, 1959.

[31] J. F. Revol, H. Bradford, J. Giasson, R. H. Marchessault, and D. G. Gray, "Helicoidal self-ordering of cellulose microfibrils in aqueous suspension," *International Journal of Biological Macromolecules*, vol. 14, no. 3, pp. 170–172, 1992.

[32] M. N. Anglès and A. Dufresne, "Plasticized Starch/Tunicin Whiskers Nanocomposites. 1. Structural Analysis," *Macromolecules*, vol. 33, no. 22, pp. 8344–8353, 2000.

[33] N. N. Wel, C. a. J. Putman, S. J. T. Noort, B. G. Grooth, and a. M. C. Emons, "Atomic force microscopy of pollen grains, cellulose microfibrils, and protoplasts," *Protoplasma*, vol. 194, no. 1-2, pp. 29–39, 1996.

[34] S. Beck-Candanedo, M. Roman, and D. Gray, "Effect of conditions on the properties behavior of wood cellulose nanocrystals suspensions," *Biomacromolecules*, vol. 6, pp. 1048–1054, 2005.

[35] D. Bondeson, A. Mathew, and K. Oksman, "Optimization of the isolation of nanocrystals from microcrystalline cellulose by acid hydrolysis," *Cellulose*, vol. 13, no. 2, pp. 171–180, 2006.

[36] P. Pooyan, L. P. Brewster, R. Tannenbaum, and H. Garmestani, "Biomimetic synthesis of two different types of renewable cellulosic nanomaterials for scaffolding in tissue engineering," *Green Processing and Synthesis*, vol. 7, no. 3, pp. 181–190, 2018.

[37] S. Beck, M. Méthot, and J. Bouchard, "General procedure for determining cellulose nanocrystal sulfate half-ester content by conductometric titration," *Cellulose*, vol. 22, no. 1, pp. 101–116, 2015.

[38] C. Honorato-Rios, A. Kuhnhold, J. R. Bruckner, R. Dannert, T. Schilling, and J. P. F. Lagerwall, "Equilibrium Liquid Crystal Phase Diagrams and Detection of Kinetic Arrest in Cellulose Nanocrystal Suspensions," *Frontiers in Materials*, vol. 3, no. May, pp. 1–13, 2016.

[39] S. Beck, M. Méthot, and J. Bouchard, "General procedure for determining cellulose nanocrystal sulfate half-ester content by conductometric titration," *Cellulose*, vol. 22, no. 1, pp. 101–116, 2015.

[40] M. Licen, B. Majaron, J. Noh, C. Schütz, L. Bergström, J. Lagerwall, and I. Drevenšek-Olenik, "Correlation between structural properties and iridescent colors of cellulose nanocrystalline films," *Cellulose*, vol. 23, no. 6, pp. 3601–3609, 2016.

[41] Q. Q. Wang, J. Y. Zhu, R. S. Reiner, S. P. Verrill, U. Baxa, and S. E. McNeil, "Approaching zero cellulose loss in cellulose nanocrystal (CNC) production: Recovery and characterization of cellulosic solid residues (CSR) and CNC," *Cellulose*, vol. 19, no. 6, pp. 2033–2047, 2012.

[42] X. M. Dong, "Chiral nematic ordered suspensions of cellulose microcrystallites," p. 128, 1996.

[43] M. S. Reid, M. Villalobos, and E. D. Cranston, "Benchmarking Cellulose Nanocrystals: From the Laboratory to Industrial Production," *Langmuir*, vol. 33, no. 7, pp. 1583–1598, 2017.

[44] K. Šolc, "Cloud-Point Curves of Polymers with Logarithmic-Normal Distribution of Molecular Weight," *Macromolecules*, vol. 8, no. 6, pp. 819–827, 1975.

[45] L. B. Kiss, J. Söderlund, G. A. Niklasson, and C. G. Granqvist, "New approach to the origin of lognormal size distributions of nanoparticles," *Nanotechnology*, vol. 10, no. 1, pp. 25–28, 1999.

[46] T. O. Pangburn and M. A. Bevan, "Role of polydispersity in anomalous interactions in electrostatically levitated colloidal systems," *Journal of Chemical Physics*, vol. 123, no. 17, 2005.

[47] C. Turley, J. C. Blackford, S. Widdicombe, D. Lowe, P. D. Nightinggale, and A. p. Rees, "Reviewing the Impact of Increased Atmospheric CO2 on Oceanic pH and the Marine Ecosystem," *Avoiding dangerous climate change*, vol. 14, no. 1, pp. 134–135, 2006.

[48] S. Beck and J. Bouchard, "Auto-Catalyzed acidic desulfation of cellulose nanocrystals," *Nordic Pulp & Paper Research Journal*, vol. 29, no. 1, pp. 6–14, 2014.

[49] Y. Hu and N. Abidi, "Distinct chiral nematic self-assembling behavior caused by different size-unified cellulose nanocrystals via a multistage separation," *Langmuir*, vol. 32, no. 38, pp. 9863–9872, 2016.

[50] M. Nordenström, A. Fall, G. Nyström, and L. Wågberg, "Formation of Colloidal Nanocellulose Glasses and Gels," *Langmuir*, vol. 33, no. 38, pp. 9772–9780, 2017.

[51] J. R. Bruckner, A. Kuhnhold, C. Honorato-Rios, T. Schilling, and J. P. Lagerwall, "Enhancing self-assembly in cellulose nanocrystal suspensions using high-permittivity solvents," *Langmuir*, vol. 32, no. 38, pp. 9854–9862, 2016.

[52] D. Gray, "Recent Advances in Chiral Nematic Structure and Iridescent Color of Cellulose Nanocrystal Films," *Nanomaterials*, vol. 6, no. 11, p. 213, 2016.

[53] J. H. Park, J. Noh, C. Sch??tz, G. Salazar-Alvarez, G. Scalia, L. Bergstr??m, and J. P. F. Lagerwall, "Macroscopic control of helix orientation in films dried from cholesteric liquid-crystalline cellulose nanocrystal suspensions," *ChemPhysChem*, vol. 15, no. 7, pp. 1477–1484, 2014.

[54] T. Odijk and H. N. W. Lekkerkerker, "Theory of the isotropic-liquid crystal phase separation for a solution of bidisperse rodlike macromolecules," *The Journal of Physical Chemistry*, vol. 89, no. 22, pp. 2090–2096, 1985.

[55] F. C. Bawden, N. W. Pirie, J. D. Bernal, and I. Fankuchen, "1936 Nature Publishing Group," *Group*, vol. 138, no. 3503, pp. 1051–1052, 1936.

[56] P.-X. Wang, W. Y. Hamad, and M. J. MacLachlan, "Structure and transformation of tactoids in cellulose nanocrystal suspensions," *Nature Communications*, vol. 7, no. May, p. 11515, 2016.

[57] G. Mosser, A. Anglo, C. Helary, Y. Bouligand, and M. M. Giraud-Guille, "Dense tissue-like collagen matrices formed in cell-free conditions," *Matrix Biology*, vol. 25, no. 1, pp. 3–13, 2006.

[58] P. Prinsen and P. van der Schoot, "Shape and director-field transformation of tactoids," *Physical Review E - Statistical Physics, Plasmas, Fluids, and Related Interdisciplinary Topics*, vol. 68, no. 2, p. 11, 2003.

[59] X. M. Dong, J.-F. Revol, and D. G. Gray, "Effect of microcrystallite preparation conditions on the formation of colloid crystals of cellulose," *Cellulose*, vol. 5, no. 1, pp. 19–32, 1998.

[60] S. Zhang, I. A. Kinloch, A. H. Windle, S. Zhang, I. A. Kinloch, and A. H. Windle, "Mesogenicity Drives Fractionation in Lyotropic Aqueous Suspensions of Multiwall Carbon Nanotubes," 2006.

[61] W. Bai, J. Holbery, and K. Li, "A technique for production of nanocrystalline cellulose with a narrow size distribution," *Cellulose*, vol. 16, no. 3, pp. 455–465, 2009.

[62] R. S. Frost, "Statistical Thermodynamics of Mixtures of Rodlike Particles. Surface Tension and the Most Probable Distribution," *Macromolecules*, vol. 21, no. 6, pp. 1854–1858, 1988.

[63] J. K. Moscicki and G. Williams, "The effect of a Gaussian distribution of chain-lengths on the phase-behaviour of a model system of rod-like macromolecules in solution," *Polymer*, vol. 23, no. 4, pp. 558–568, 1982.

[64] H. N. Lekkerkerker, P. Coulon, R. Van Der Haegen, and R. Deblieck, "On the isotropic-liquid crystal phase separation in a solution of rodlike particles of different lengths," *The Journal of Chemical Physics*, vol. 80, no. 7, pp. 3427–3433, 1984.

[65] N. Donkai, "Lyotropic mesophase of imogolite: molecular weight fractionation and polydispersity effect," vol. 7, pp. 1–7, 1993.

[66] A. Speranza and P. Sollich, "Isotropic-nematic phase equilibria in the Onsager theory of hard rods with length polydispersity," *Physical Review E - Statistical Physics, Plasmas, Fluids, and Related Interdisciplinary Topics*, vol. 67, no. 6, p. 19, 2003.

[67] A. Speranza and P. Sollich, "Isotropic-nematic phase equilibria of polydisperse hard rods: The effect of fat tails in the length distribution," *Journal of Chemical Physics*, vol. 118, no. 11, pp. 5213–5223, 2003.

[68] H. H. Wensink and G. J. Vroege, "Isotropic-nematic phase behavior of length-polydisperse hard rods," *Journal of Chemical Physics*, vol. 119, no. 13, pp. 6868–6882, 2003.

[69] V. A. Davis, A. N. G. Parra-Vasquez, M. J. Green, P. K. Rai, N. Behabtu, V. Prieto, R. D. Booker, J. Schmidt, E. Kesselman, W. Zhou, H. Fan, W. W. Adams, R. H. Hauge,

J. E. Fischer, Y. Cohen, Y. Talmon, R. E. Smalley, and M. Pasquali, "True solutions of single-walled carbon nanotubes for assembly into macroscopic materials," *Nature Nanotechnology*, vol. 4, no. 12, pp. 830–834, 2009.

[70] P. Woolston and J. S. Van Duijneveldt, "Isotropic-nematic phase transition of polydisperse clay rods," *Journal of Chemical Physics*, vol. 142, no. 18, 2015.

[71] P. A. Buining and N. W. Lekkerkerker, "Isotropic-Nematic Phase Separation of a Dispersion," *The Journal of Chemical Physics*, vol. 97, no. Figure 1, pp. 11510–11516, 1993.

[72] C. Schütz, *Fabrication of nanocellulose-based materials*. 2015.

[73] D. G. Gray and X. Mu, "TwistBend Stage in the Relaxation of Sheared Chiral Nematic Suspensions of Cellulose Nanocrystals," *ACS Omega*, vol. 1, no. 2, pp. 212–219, 2016.

[74] R. M. Parker, B. Frka-petesic, G. Guidetti, G. Kamita, G. Consani, C. Abell, and S. Vignolini, "Hierarchical Self-Assembly of Cellulose Nanocrystals in a Conned Geometry," *ACS nano*, vol. 10, pp. 8443–8449, 2016.

[75] S. Shafeiei-Sabet, W. Y. Hamad, and S. G. Hatzikiriakos, "Influence of degree of sulfation on the rheology of cellulose nanocrystal suspensions," *Rheologica Acta*, vol. 52, no. 8-9, pp. 741–751, 2013.

[76] E. E. Ureña-Benavides, G. Ao, V. A. Davis, and C. L. Kitchens, "Rheology and phase behavior of lyotropic cellulose nanocrystal suspensions," *Macromolecules*, vol. 44, no. 22, pp. 8990–8998, 2011.

[77] L. Lewis, M. Derakhshandeh, S. G. Hatzikiriakos, W. Y. Hamad, and M. J. MacLachlan, "Hydrothermal Gelation of Aqueous Cellulose Nanocrystal Suspensions," *Biomacromolecules*, vol. 17, no. 8, pp. 2747–2754, 2016.

[78] X. Mu and D. G. Gray, "Formation of chiral nematic films from cellulose nanocrystal suspensions is a two-stage process," *Langmuir*, vol. 30, no. 31, pp. 9256–9260, 2014.

[79] J. Araki, M. Wada, S. Kuga, and T. Okano, "Influence of surface charge on viscosity behavior of cellulose microcrystal suspension," *Journal of Wood Science*, vol. 45, no. 3, pp. 258–261, 1999.

[80] D. G. Gray, "Order and gelation of cellulose nanocrystal suspensions: An overview of some issues," *Philosophical Transactions of the Royal Society A: Mathematical, Physical and Engineering Sciences*, vol. 376, no. 2112, pp. 1–7, 2018.

[81] J. Lapointe and D. A. Marvin, "Filamentous Bacterial Viruses VIII. Liquid Crystals of fd," *Molecular Crystals and Liquid Crystals*, vol. 19, no. 3-4, pp. 269–278, 2007.

[82] Z. Dogic and S. Fraden, "PRLsmectic97," vol. 78, no. 12, pp. 1–4, 1997.

[83] K. R. Purdy, Z. Dogic, S. Fraden, A. Rühm, L. Lurio, and S. G. Mochrie, "Measuring the nematic order of suspensions of colloidal fd virus by x-ray diffraction and optical birefringence," *Physical Review E - Statistical Physics, Plasmas, Fluids, and Related Interdisciplinary Topics*, vol. 67, no. 3, p. 12, 2003.

[84] P. Taylor, J. Tang, and S. Fraden, "Isotropic-cholesteric phase transition in colloidal suspensions of filamentous bacteriophage fd Isotropic-cholesteric phase transition in colloidal suspensions of filamentous bacteriophage fd," *Mosaic A Journal For The Interdisciplinary Study Of Literature*, no. March 2014, pp. 37–41, 2006.

[85] S. W. Lee, B. M. Wood, and A. M. Belcher, "Chiral smectic C structures of virus-based films," *Langmuir*, vol. 19, no. 5, pp. 1592–1598, 2003.

[86] Z. Dogic and S. Fraden, "Cholesteric phase in virus suspensions," *Langmuir*, vol. 16, no. 20, pp. 7820–7824, 2000.

[87] Z. Dogic and S. Fraden, "Ordered phases of filamentous viruses," *Current Opinion in Colloid and Interface Science*, vol. 11, no. 1, pp. 47–55, 2006.

[88] A. A. Kornyshev, D. J. Lee, S. Leikin, and A. Wynveen, "Structure and interactions of biological helices," *Reviews of Modern Physics*, vol. 79, no. 3, pp. 943–996, 2007.

[89] A. B. Fall, S. B. Lindstrom, O. Sundman, L. Odberg, and L. Wagberg, "Colloidal stability of aqueous nanofibrillated cellulose dispersions," *Langmuir*, vol. 27, no. 18, pp. 11332–11338, 2011.

[90] K. R. Peddireddy, I. Capron, T. Nicolai, and L. Benyahia, "Gelation Kinetics and Network Structure of Cellulose Nanocrystals in Aqueous Solution," *Biomacromolecules*, vol. 17, no. 10, pp. 3298–3304, 2016.

[91] Y. Xu, A. D. Atrens, and J. R. Stokes, ""Liquid, Gel and Soft Glass" Phase Transitions and Rheology of Nanocrystalline Cellulose Suspensions As a Function of Concentration and Salinity," *Soft Matter*, vol. 14, no. 10, pp. 1953–1963, 2018.

[92] T. Abitbol, D. Kam, Y. Levi-Kalisman, D. G. Gray, and O. Shoseyov, "Surface Charge Influence on the Phase Separation and Viscosity of Cellulose Nanocrystals," *Langmuir*, vol. 34, no. 13, pp. 3925–3933, 2018.

[93] F. Cherhal, B. Cathala, and I. Capron, "Surface charge density variation to promote structural orientation of cellulose nanocrystals," *Nord. Pulp. Pap. Res. J.*, vol. 30, no. 1, pp. 126–131, 2015.

[94] F. Cherhal, F. Cousin, and I. Capron, "Influence of charge density and ionic strength on the aggregation process of cellulose nanocrystals in aqueous suspension, as revealed by small-angle neutron scattering," *Langmuir*, vol. 31, no. 20, pp. 5596–5602, 2015.

[95] A. Varghese, R. Rajesh, and S. Vemparala, "Aggregation of rod-like polyelectrolyte chains in the presence of monovalent counterions," *Journal of Chemical Physics*, vol. 137, no. 23, 2012.

[96] S. Zhou, "Density functional analysis of like-charged attraction between two similarly charged cylinder polyelectrolytes," *Langmuir*, vol. 29, no. 40, pp. 12490–12501, 2013.

[97] M. Chau, S. E. Sriskandha, D. Pichugin, H. Thérien-Aubin, D. Nykypanchuk, G. Chauve, M. Méthot, J. Bouchard, O. Gang, and E. Kumacheva, "Ion-Mediated Gelation of Aqueous Suspensions of Cellulose Nanocrystals," *Biomacromolecules*, vol. 16, no. 8, pp. 2455–2462, 2015.

[98] F. Cherhal, B. Cathala, and I. Capron, "Surface charge density variation to promote structural orientation of cellulose nanocrystals," *Nord. Pulp. Pap. Res. J.*, vol. 30, no. 1, pp. 126–131, 2015.

[99] K. Kang and J. K. G. Dhont, "Glass transition in suspensions of charged rods: Structural arrest and texture dynamics," *Physical Review Letters*, vol. 110, no. 1, 2013.

[100] K. Kang and J. K. Dhont, "Structural arrest and texture dynamics in suspensions of charged colloidal rods," *Soft Matter*, vol. 9, no. 17, pp. 4401–4411, 2013.

[101] J. P. Straley, "Theory of piezoelectricity in nematic liquid crystals, and of the cholesteric ordering," *Physical Review A*, vol. 14, no. 5, pp. 1835–1841, 1976.

[102] S. Dussi, S. Belli, R. Van Roij, and M. Dijkstra, "Cholesterics of colloidal helices: Predicting the macroscopic pitch from the particle shape and thermodynamic state," *Journal of Chemical Physics*, vol. 142, no. 7, 2015.

[103] H. Wensink, Wensink, and H. H., "Effect of Size Polydispersity on the Pitch of Nanorod Cholesterics," *Crystals*, vol. 9, no. 3, p. 143, 2019.

[104] T. H. Zhao, R. M. Parker, C. A. Williams, K. T. Lim, B. Frka-Petesic, and S. Vignolini, "Printing of Responsive Photonic Cellulose Nanocrystal Microfilm Arrays," *Advanced Functional Materials*, vol. 1804531, pp. 1–8, 2018.

[105] A. G. Dumanli, H. M. Van Der Kooij, G. Kamita, E. Reisner, J. J. Baumberg, U. Steiner, and S. Vignolini, "Digital color in cellulose nanocrystal films," *ACS Applied Materials and Interfaces*, vol. 6, no. 15, pp. 12302–12306, 2014.

[106] T. Hiratani, W. Y. Hamad, and M. J. MacLachlan, "Transparent Depolarizing Organic and Inorganic Films for Optics and Sensors," *Advanced Materials*, vol. 29, no. 13, pp. 1–6, 2017.

[107] R. M. Parker, G. Guidetti, C. A. Williams, T. Zhao, A. Narkevicius, S. Vignolini, and B. Frka-Petesic, "The Self-Assembly of Cellulose Nanocrystals: Hierarchical Design of Visual Appearance," *Advanced Materials*, vol. 30, no. 19, pp. 1–13, 2018.

[108] J.-F. Revol, L. Godbout, and D. G. Gray, "Solid self-assembled films of cellulose with chiral nematic order and optically variable properties," *Journal of Pulp and Paper Science*, vol. 24, no. 5, pp. 146–149, 1998.

[109] M. Giese, L. K. Blusch, M. K. Khan, and M. J. MacLachlan, "Functional materials from cellulose-derived liquid-crystal templates," *Angewandte Chemie - International Edition*, vol. 54, no. 10, pp. 2888–2910, 2015.

[110] X. M. Dong, T. Kimura, J.-F. Revol, and D. G. Gray, "Effects of Ionic Strength on the IsotropicChiral Nematic Phase Transition of Suspensions of Cellulose Crystallites," *Langmuir*, vol. 12, pp. 2076–2082, 1 1996.

[111] Y. K. Yarovoy and M. M. Labes, "Effect of chiral polymers on lyotropic liquid crystals," *Journal of the American Chemical Society*, vol. 119, no. 50, pp. 12109–12113, 1997.

[112] A. Hirai, O. Inui, F. Horii, and M. Tsuji, "Phase separation behavior in aqueous suspensions of bacterial cellulose nanocrystals prepared by sulfuric acid treatment.," *Langmuir : the ACS journal of surfaces and colloids*, vol. 25, no. 1, pp. 497–502, 2009.

[113] C. Schütz, M. Agthe, A. B. Fall, K. Gordeyeva, V. Guccini, M. Salajkova, T. S. Plivelic, J. P. F. Lagerwall, G. Salazar-Alvarez, and L. Bergström, "Rod Packing in Chiral Nematic Cellulose Nanocrystal Dispersions Studied by Small-Angle X-ray Scattering and Laser Diffraction," *Langmuir*, vol. 31, no. 23, pp. 6507–6513, 2015.

[114] D. G. Gray, "Chiral nematic ordering of polysaccharides," *Carbohydrate Polymers*, vol. 25, no. 4, pp. 277–284, 1994.

[115] S. Y. Jo, B. C. Kim, S. W. Jeon, J. H. Bae, M. Walker, M. Wilson, S. W. Choi, and H. Takezoe, "Enhancement of the helical twisting power with increasing the terminal chain length of nonchiral bent-core molecules doped in a chiral nematic liquid crystal," *RSC Advances*, vol. 7, no. 4, pp. 1932–1935, 2017.

[116] M. P. Allen, "Calculating the helical twisting power of dopants in a liquid crystal by computer simulation," *Physical Review E*, vol. 47, no. 6, pp. 4611–4614, 1993.

[117] X.-M. Dong and D. G. Gray, "Effect of Counterions on Ordered Phase Formation in Suspensions of Charged Rodlike Cellulose Crystallites," vol. 7463, pp. 2404–2409, 1997.

[118] S. Beck, J. Bouchard, and R. Berry, "Controlling the reection wavelength of iridescent solid films of nanocrystalline cellulose," *Biomacromolecules*, vol. 12, pp. 167–172, 2011.

[119] A. Ghafoor and G. Murtaza, "Estimation of ionic strength from electrical conductivity of punjab ground waters," *Pakistan Journal of Agricultural Sciences*, vol. 37, no. I, pp. 113–115, 2000.

[120] N. Verdel and P. Bukovec, "Correlation between the increasing conductivity of aqueous solutions of cation chlorides with time and the "salting-out" properties of the cations," *Entropy*, vol. 18, no. 3, 2016.

[121] Y. Liu, D. Stoeckel, K. Gordeyeva, M. Agthe, C. Schütz, A. B. Fall, and L. Bergström, "Nanoscale Assembly of Cellulose Nanocrystals during Drying and Redispersion," *ACS Macro Letters*, vol. 7, pp. 172–177, 2 2018.

[122] T. Phan-Xuan, A. Thuresson, M. Skepö, A. Labrador, R. Bordes, and A. Matic, "Aggregation behavior of aqueous cellulose nanocrystals: the effect of inorganic salts," *Cellulose*, vol. 23, no. 6, pp. 3653–3663, 2016.

[123] N. Schwierz, D. Horinek, and R. R. Netz, "Anionic and cationic hofmeister effects on hydrophobic and hydrophilic surfaces," *Langmuir*, vol. 29, no. 8, pp. 2602–2614, 2013.

[124] A. Stroobants, H. N. W. Lekkerkerker, and T. Odijk, "Effect of electrostatic interaction on the liquid crystal phase transition in solutions of rodlike polyelectrolytes," *Macromolecules*, vol. 19, no. 8, pp. 2232–2238, 1986.

[125] E. Figgemeier and K. Hiltrop, "Quantified chirality, molecular similarity, and helical twisting power in lyotropic chiral nematic guest/host systems," *Liquid Crystals*, vol. 26, no. 9, pp. 1301–1305, 1999.

[126] C. B. Stanley, H. Hong, and H. H. Strey, "DNA Cholesteric Pitch as a Function of Density and Ionic Strength," *Biophysical Journal*, vol. 89, no. 4, pp. 2552–2557, 2005.

[127] J. P. Straley, "Theory of piezoelectricity in nematic liquid crystals, and of the cholesteric ordering," *Physical Review A*, vol. 14, no. 5, pp. 1835–1841, 1976.

[128] J. Araki and S. Kuga, "Effect of trace electrolyte on liquid crystal type of cellulose microcrystals," *Langmuir*, vol. 17, no. 15, pp. 4493–4496, 2001.

[129] J. Araki, M. Wada, S. Kuga, and T. Okano, "Birefringent Glassy Phase of a Cellulose Microcrystal Suspension," *Langmuir*, vol. 16, no. 6, pp. 2413–2415, 2000.

[130] X. M. Dong, T. Kimura, J.-F. Revol, and D. G. Gray, "Effects of Ionic Strength on the IsotropicChiral Nematic Phase Transition of Suspensions of Cellulose Crystallites," *Langmuir*, vol. 12, pp. 2076–2082, 1 1996.

[131] B. Frka-Petesic, G. Guidetti, G. Kamita, and S. Vignolini, "Controlling the Photonic Properties of Cholesteric Cellulose Nanocrystal Films with Magnets," *Advanced Materials*, vol. 29, no. 32, pp. 1–7, 2017.

[132] J. Pan, W. Hamad, and S. K. Straus, "Parameters affecting the chiral nematic phase of nanocrystalline cellulose films," *Macromolecules*, vol. 43, no. 8, pp. 3851–3858, 2010.

[133] B. D. Wilts, A. G. Dumanli, R. Middleton, P. Vukusic, and S. Vignolini, "Invited Article: Chiral optics of helicoidal cellulose nanocrystal films," *APL Photonics*, vol. 2, no. 4, 2017.

[134] R. M. Parker, B. Frka-Petesic, G. Guidetti, G. Kamita, G. Consani, C. Abell, and S. Vignolini, "Hierarchical Self-Assembly of Cellulose Nanocrystals in a Confined Geometry," *ACS Nano*, vol. 10, no. 9, pp. 8443–8449, 2016.

[135] S. Beck, J. Bouchard, G. Chauve, and R. Berry, "Controlled production of patterns in iridescent solid films of cellulose nanocrystals," *Cellulose*, vol. 20, no. 3, pp. 1401–1411, 2013.

[136] T. D. Nguyen, W. Y. Hamad, and M. J. MacLachlan, "Tuning the iridescence of chiral nematic cellulose nanocrystals and mesoporous silica films by substrate variation," *Chemical Communications*, vol. 49, no. 96, pp. 11296–11298, 2013.

[137] S. Park, J. O. Baker, M. E. Himmel, P. A. Parilla, and D. K. Johnson, "Cellulose crystallinity index: measurement techniques and their impact on interpreting cellulase performance," *Biotechnology for Biofuels*, vol. 3, no. 1, p. 10, 2010.

[138] F. Kimura, T. Kimura, M. Tamura, A. Hirai, M. Ikuno, and F. Horii, "Magnetic alignment of the chiral nematic phase of a cellulose microfibril suspension," *Langmuir*, vol. 21, no. 5, pp. 2034–2037, 2005.

[139] C. C. Y. Cheung, M. Giese, J. A. Kelly, W. Y. Hamad, and M. J. Maclachlan, "Iridescent chiral nematic cellulose nanocrystal/polymer composites assembled in organic solvents," *ACS Macro Letters*, vol. 2, no. 11, pp. 1016–1020, 2013.

[140] K. E. Shopsowitz, H. Qi, W. Y. Hamad, and M. J. MacLachlan, "Free-standing mesoporous silica films with tunable chiral nematic structures," *Nature*, vol. 468, no. 7322, pp. 422–426, 2010.

[141] D. G. Gray and X. Mu, "Chiral nematic structure of cellulose nanocrystal suspensions and films; Polarized light and atomic force microscopy," *Materials*, vol. 8, no. 11, pp. 7873–7888, 2015.

[142] X. Mu and D. G. Gray, "Droplets of cellulose nanocrystal suspensions on drying give iridescent 3-D "coffee-stain"rings," *Cellulose*, vol. 22, no. 2, pp. 1103–1107, 2015.

[143] J. Majoinen, E. Kontturi, O. Ikkala, and D. G. Gray, "SEM imaging of chiral nematic films cast from cellulose nanocrystal suspensions," *Cellulose*, vol. 19, no. 5, pp. 1599–1605, 2012.

[144] P. Saha and V. A. Davis, "Photonic Properties and Applications of Cellulose Nanocrystal Films with Planar Anchoring," *ACS Applied Nano Materials*, vol. 1, no. 5, pp. 2175–2183, 2018.

[145] A. G. Dumanli, G. Kamita, J. Landman, H. van der Kooij, B. J. Glover, J. J. Baumberg, U. Steiner, and S. Vignolini, "Controlled, bio-inspired self-assembly of cellulose-based chiral reflectors," *Advanced Optical Materials*, vol. 2, no. 7, pp. 646–650, 2014.

[146] B. Wang and A. Walther, "Self-Assembled, Iridescent, Crustacean-Mimetic Nanocomposites with Tailored Periodicity and Layered Cuticular Structure," no. 11, pp. 10637–10646, 2015.

[147] E. D. Cranston and D. G. Gray, "Birefringence in spin-coated films containing cellulose nanocrystals," *Colloids and Surfaces A: Physicochemical and Engineering Aspects*, vol. 325, no. 1-2, pp. 44–51, 2008.

[148] B. Frka-Petesic, J. Sugiyama, S. Kimura, H. Chanzy, and G. Maret, "Negative Diamagnetic Anisotropy and Birefringence of Cellulose Nanocrystals," *Macromolecules*, vol. 48, no. 24, pp. 8844–8857, 2015.

[149] Y. P. Zhanga, V. P. Chodavarapua, A. G. Kirka, and M. P. Andrews, "Structured color humidity indicator from reversible pitch tuning in self-assembled nanocrystalline cellulose films," *Sensors and Actuators, B: Chemical*, vol. 176, pp. 692–697, 2013.

[150] Y. P. Zhang, "Nanocrystalline cellulose for covert optical encryption," *Journal of Nanophotonics*, vol. 6, no. 1, p. 063516, 2012.

[151] S. Beck, J. Bouchard, and R. Berry, "Dispersibility in water of dried nanocrystalline cellulose," *Biomacromolecules*, vol. 13, no. 5, pp. 1486–1494, 2012.

[152] M. Anyfantakis, D. Baigl, and B. P. Binks, "Evaporation of Drops Containing Silica Nanoparticles of Varying Hydrophobicities: Exploiting ParticleParticle Interactions for Additive-Free Tunable Deposit Morphology," 2017.

[153] E. L. Talbot, L. Yang, A. Berson, and C. D. Bain, "Control of the particle distribution in inkjet printing through an evaporation-driven sol-gel transition," *ACS Applied Materials and Interfaces*, vol. 6, no. 12, pp. 9572–9583, 2014.

[154] H. M. Gorr, J. M. Zueger, and J. A. Barnard, "Characteristic size for onset of coffee-ring effect in evaporating lysozyme-water solution droplets," *Journal of Physical Chemistry B*, vol. 116, no. 40, pp. 12213–12220, 2012.

[155] M. Pack, H. Hu, D. O. Kim, X. Yang, and Y. Sun, "Colloidal Drop Deposition on Porous Substrates: Competition among Particle Motion, Evaporation, and Infiltration," *Langmuir*, vol. 31, no. 29, pp. 7953–7961, 2015.

[156] C. F. Cerretani, N. H. Ho, and C. J. Radke, "Water-evaporation reduction by duplex fi lms : Application to the human tear fi lm," *Advances in Colloid and Interface Science*, vol. 197-198, pp. 33–57, 2013.

[157] K. Shimura, N. Uchiyama, and K. I. Kasai, "Prevention of evaporation of small-volume sample solutions for capillary electrophoresis using a mineral-oil overlay," *Electrophoresis*, vol. 22, no. 16, pp. 3471–3477, 2001.

[158] T. Wu, J. Li, J. Li, S. Ye, J. Wei, and J. Guo, "A bio-inspired cellulose nanocrystal-based nanocomposite photonic film with hyper-reflection and humidity-responsive actuator properties," *J. Mater. Chem. C*, vol. 4, no. 41, pp. 9687–9696, 2016.

[159] L. Saadaoui, G. Petriashvili, M. P. De Santo, R. Hamdi, T. Othman, and R. Barberi, "Electrically controllable multicolor cholesteric laser," *Optics Express*, vol. 23, no. 17, p. 22922, 2015.